

Chemical Science

Accepted Manuscript

This article can be cited before page numbers have been issued, to do this please use: S. Rasaily, G. K. Dam and S. K. Ghosh, *Chem. Sci.*, 2026, DOI: 10.1039/D6SC01670G.



This is an Accepted Manuscript, which has been through the Royal Society of Chemistry peer review process and has been accepted for publication.

Accepted Manuscripts are published online shortly after acceptance, before technical editing, formatting and proof reading. Using this free service, authors can make their results available to the community, in citable form, before we publish the edited article. We will replace this Accepted Manuscript with the edited and formatted Advance Article as soon as it is available.

You can find more information about Accepted Manuscripts in the [Information for Authors](#).

Please note that technical editing may introduce minor changes to the text and/or graphics, which may alter content. The journal's standard [Terms & Conditions](#) and the [Ethical guidelines](#) still apply. In no event shall the Royal Society of Chemistry be held responsible for any errors or omissions in this Accepted Manuscript or any consequences arising from the use of any information it contains.

Advanced Functional Porous Materials for Photocatalytic H₂O₂ Production

Sagarmani Rasaily,^a Gourab K Dam,^a and Sujit K. Ghosh^{*a,b}

Received 00th January 20xx,
Accepted 00th January 20xx

DOI: 10.1039/x0xx00000x

Hydrogen peroxide (H₂O₂) is one of the most essential chemicals that has a high oxidising ability (1.763 V at pH 0) and the highest active oxygen content (47.1 wt%). Current synthesis techniques are energy-intensive, generate harmful waste, and pose the potential danger of explosions. Photocatalytic H₂O₂ production via O₂ reduction is a promising, sustainable, and eco-friendly method that harnesses solar energy to drive the reaction while also requiring low energy input and ensuring safety. Interestingly, advanced functional porous materials (AFPMs), like covalent organic frameworks (COFs), metal-organic frameworks (MOFs), porous organic polymers (POPs), covalent triazine framework (CTF), metal-organic polyhedra (MOP) and hydrogen bonded organic framework (HOF) have surfaced as promising photocatalysts for effective photocatalysis. These materials exhibit tunable pore size, high surface area, and robust framework, all of which facilitate mass transfer, adequate active sites, and efficient recycling. In this review, we have discussed the different strategies applied in recent literature to improve the photocatalytic efficiency in these materials towards photocatalytic H₂O₂ synthesis. This review provides an extensive summary and discussion of the latest applications of AFPM-based photocatalysts in H₂O₂ photosynthesis. The historical background and fundamental principles underlying photocatalysts for photocatalytic H₂O₂ production are briefly outlined. This is followed by a detailed classification and discussion of the strategies reported to enhance photocatalytic performance. The review addresses AFPM-based photocatalyst challenges and future prospects for light-driven H₂O₂ production.

Introduction

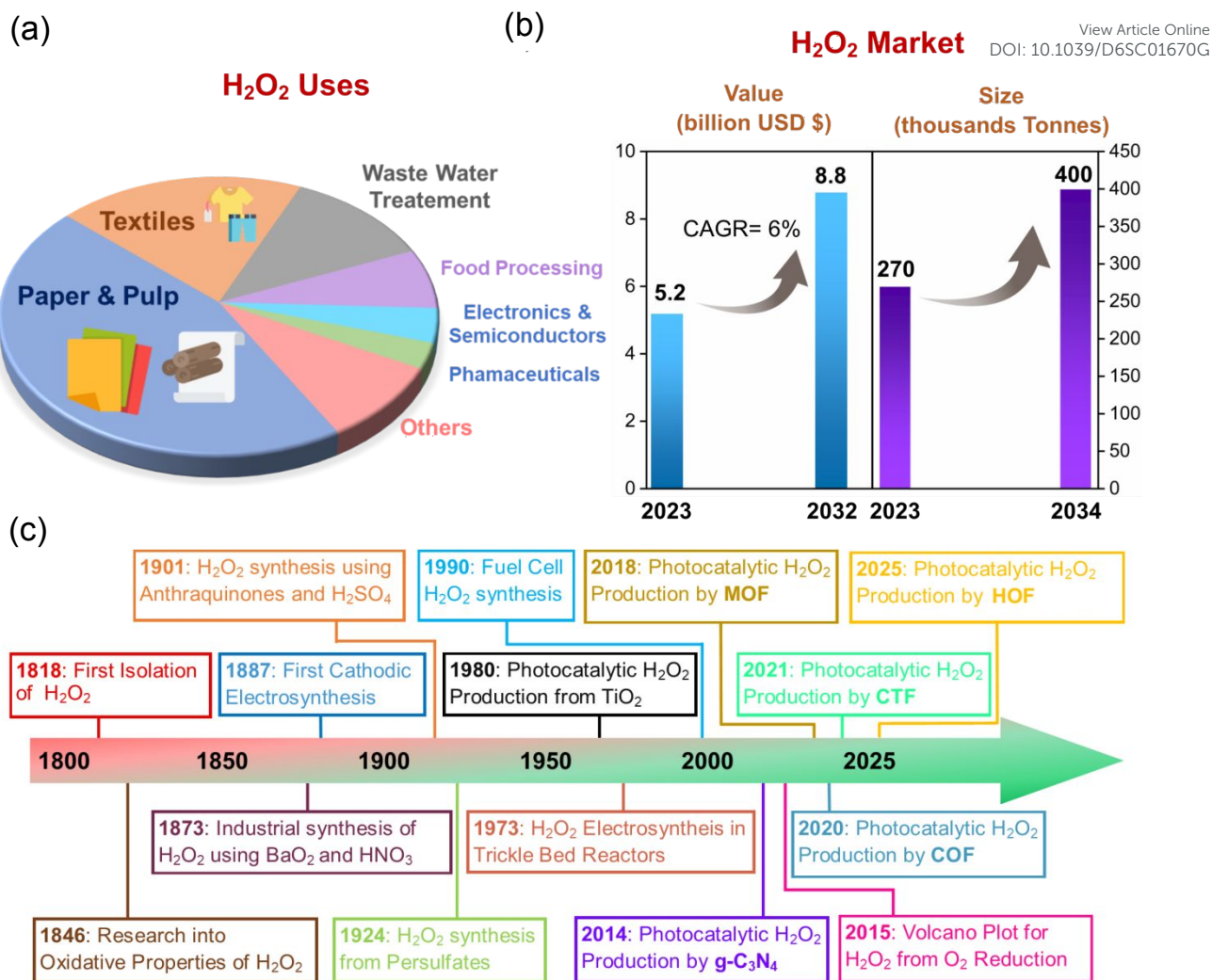
Hydrogen peroxide (H₂O₂), first prepared by Thenard in 1818, was a product of a reaction between barium peroxide and nitric acid.¹ Also known as oxygenated water, H₂O₂ is a non-planar molecule with C₂ symmetry and enantiomerism, attributed to its 95° dihedral angle between its two O-H bonds. Besides being the smallest and simplest chiral molecule, H₂O₂ can act as both a strong oxidant across a wide pH range and a reducing agent, capable of reducing stronger oxidising compounds such as Ce(SO₄)₂, KMnO₄, Cl₂, NaClO, etc.¹ Additionally, the derivatives of H₂O₂, such as hydroxyl radicals (·OH), can break down nearly all types of organic pollutants or damage essential components within microbial cells, leading to the removal of organic contaminants or the elimination of harmful microorganisms.^{2,3} Initially, H₂O₂ was known for bleaching natural dyes and was synthesised from barium peroxide. Gradually, researchers found the application of H₂O₂ in various fields. The significant timeline towards the application of H₂O₂ towards various applications includes: (a) 1888: first medical use as treating numerous diseases, (b) 1891: first report as disinfectant.⁴ (c) 1920: reports of intravenous injection using H₂O₂ in treating influenza pneumonia during World War,⁵ (d) 1967: protective action of H₂O₂ against ischemia-reperfusion (IR) injury,⁶ (e) 1980: intravenous infusion of H₂O₂ for oxidative therapy,⁷ (f) H₂O₂ as an alternative to

chlorine as a bleaching agent in paper production,⁸ (g) terminal oxidant towards industrial synthesis of propene epoxide (PO).⁸ Today, H₂O₂ has been established as one of the most essential chemicals globally.⁹ It is recognised as a versatile and sustainable reagent. With the improvement of technologies, it is more dedicatedly applied in chemical synthesis, paper and pulp bleaching, food processing, biomedical therapy, disinfection, wastewater treatment, metal mining and processing, etc (Scheme 1a).^{10–12} Furthermore, H₂O₂ is an eco-friendly and safe energy storage medium, offering an energy density of 2.1 MJ kg⁻¹ at 60 wt%, making it ideal for applications in H₂O₂ fuel cells and cutting-edge power technologies. The H₂O₂ fuel cell, with a voltage of +1.09 V vs NHE (standard hydrogen electrode), is similar in performance to the methanol fuel cell (+1.21 V) and the H₂ fuel cell (+1.23 V), making it an environmentally benign alternative as an energy carrier.¹³ The increasing use of H₂O₂ has led to a rise in global demand, reaching a market volume of 270,000 tons in 2023, with projections to grow to 400,000 tons by 2032 (Scheme 1b).¹⁴ Due to the various intriguing properties and versatile applications, the market value of H₂O₂ was estimated at \$5.2 billion in 2023. According to the report, this is expected to grow to \$8.8 billion by 2032 (Scheme 1b).¹⁵ The first commercial production of H₂O₂ was achieved by 1909 *via* an electrochemical method using H₂SO₄. By the 1930s, the oxidation process for synthesising H₂O₂ had been implemented in the industry by the 1940s. The oxidation process was proven to be economically more preferred over the electrolytic process, and two processes, namely isopropyl oxidation and the anthraquinone oxidation (AO)

^a Department of Chemistry, Indian Institute of Science Education and Research (IISER) Pune, 411008, India.

^b Centre for Water Research (CWR), Indian Institute of Science Education and Research (IISER) Pune, 411008, India.
Email: sghosh@iiserpune.ac.in.





Scheme 1: a) Pi diagram for the various uses of H₂O₂.¹⁴ (b) Summary of expected market value.^{14,15} (c) Schematic timeline for the synthesis of H₂O₂ using different techniques.¹⁶

process, were developed for the large-scale production of H₂O₂. Today, the rising global demand for H₂O₂ is mainly satisfied using the AO process developed by IG Farben (now BASF).^{1,8} The AO process primarily involves the hydrogenation of 2-ethyl-anthraquinone to form 2-ethyl-anthrahydroquinone and its oxidation further using a Pd or Ni catalyst. The AO process demands hydrogen in high purity and oxygen or air for non-catalytic oxidation. Consequently, the AO process could produce H₂O₂ up to 60-70% w/w strength. However, the AO process is less atom-economic and energy-intensive, with an energy requirement of ~13,000 Btu/lb (8.1 kWh/kg).¹⁷ On the other hand, the isopropyl oxidation process has a significant drawback for industrial H₂O₂ production, as it requires large quantities of raw materials and faces challenges in isolating H₂O₂ with high purity.¹⁸ Apart from the oxidation process, the direct synthesis of H₂O₂ is also well-known. It can produce ~61 moles per kilogram of catalyst (kg cat) per hour by reacting H₂ and O₂ at high pressure and using a Pd-Sn catalyst.¹⁹⁻²¹ However, the explosive nature of H₂ and O₂ under high pressure, and the requirement for novel metal catalysts, have limited the industrial-scale synthesis.^{19,22} Therefore, with the significant limitations of conventional methods, there is significant

focus and research to explore and develop eco-friendly alternatives for producing H₂O₂, addressing both the rising demand and the need for environmentally benign H₂O₂ production methods. The schematic timeline for the production of H₂O₂ using different techniques has been provided in Scheme 1c.¹⁶ Towards developing sustainable alternative processes for H₂O₂ production, electrochemical and photocatalytic techniques have gained significant interest. In electrochemical techniques, H₂O₂ can be produced from the reduction of O₂ in H₂O at ambient conditions, also well known as a two-electron oxygen reduction reaction (2e⁻ ORR). It offers numerous benefits, including safe operation, a clean production process, simple reactions at ambient conditions, and low energy consumption. However, the electrochemical 2e⁻ ORR is often hindered by high overpotential due to slow kinetics and is also influenced by the competing four-electron pathway that leads to the production of H₂O. Significant research is going on for its development towards H₂O₂ production. Various efficient electrocatalysts have been reported that include metal oxides,^{23,24} single-atom catalysts (SACs),²⁵⁻²⁷ carbon materials,^{28,29} porous materials.³⁰ On the other hand, the photocatalytic production of



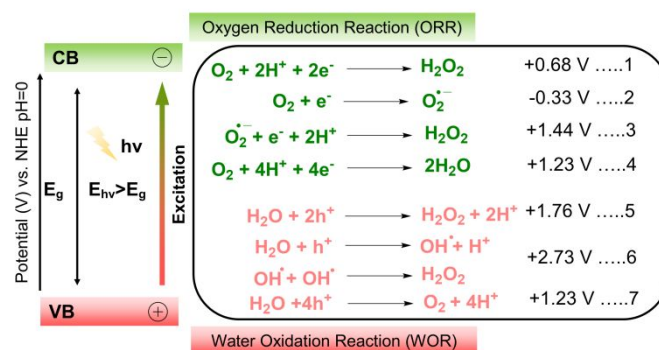
H₂O₂ using solar energy is one of the most sustainable methods of producing H₂O₂. Sunlight, a clean and abundant source, provides more than 1.19×10^{17} J of energy to the Earth per second. In nature, green plants and certain organisms are well known to harness solar energy to convert carbon dioxide into carbohydrates through photosynthesis. Motivated by the conversion of solar energy to chemical energy is well-known chemistry today and is applied towards the production of valuable chemicals such as ammonia,³¹ water splitting,^{32–34} organic chemicals,^{35–37} CO₂ reduction^{38,39} etc. The photocatalytic production of H₂O₂ has also gained significant interest recently and is developing as a promising alternative to conventional methods, especially targeting the decentralised production and in situ utilisation. The photocatalytic H₂O₂ production from abundant H₂O and O₂ as raw materials offers high product selectivity, high atom economy, and less waste production. The photosynthesis of H₂O₂ proceeds through an oxygen reduction reaction (ORR) and water oxidation process (WOR). However, the photocatalytic production of H₂O₂ using water and oxygen is thermodynamically not feasible as it has a high ΔG value of ~ 117 kJ mol⁻¹. Therefore, developing an efficient photocatalyst is essential for the photocatalytic production of H₂O₂, and research in this area is gaining significant interest.

Mechanistic pathway towards photocatalytic H₂O₂:

The photocatalytic production of H₂O₂ over functional porous materials typically involves three key steps: (i) light absorption, which excites electrons and generates photoinduced charge carriers; (ii) migration of these electrons from the valence band (VB) to the conduction band (CB), leaving behind holes. The energy gap between VB and CB is also known as bandgap energy (BE), and (iii) redox reactions between the remaining photogenerated carriers and surface-adsorbed O₂ and H₂O molecules, leading to H₂O₂ formation. For a photocatalyst to be efficient towards the desired photocatalytic reaction, the energy of the incident light must be equal to or exceed that of the photocatalyst so that the electron and hole pairs to be photoexcited and separate into the CB and VB, respectively.

The production of H₂O₂ could be obtained through ORR and WOR concomitantly. The ORR, leading to the formation of H₂O₂, typically proceeds through either a direct one-step 2e⁻ pathway or an indirect two-step, single-electron reduction (equations (1), Scheme 2) or *via* a direct one-step, two-electron reduction (equation (2), Scheme 2).⁴⁰ In direct one-step ORR, the adsorbed oxygen is reduced by two electrons, and its combination with two protons produces H₂O₂ directly (Equation 1, Scheme 2). The thermodynamic potential for procuring the direct 2e⁻ ORR pathway is 0.68 V. In the indirect two-step ORR pathway, the absorbed oxygen is first reduced with one electron to form superoxide radical (O_2^-) (Equation 2, Scheme 2). This is also the rate-determining step that requires a potential of -0.33 V. The superoxide formed then combines with one electron and two protons to produce H₂O₂ (Equation 3, Scheme 2). Additionally, the 2e⁻ ORR for H₂O₂ production competes with the 4e⁻ ORR pathway to H₂O (Equation 4, Scheme 2), which is thermodynamically more favourable due to its more positive potential (+1.23 V) compared to

the 2e⁻ ORR (+0.68 V). Since the ORR pathway depends on photogenerated electrons, their rapid recombination with holes can significantly reduce the efficiency of H₂O₂ formation. The use of sacrificial agents such as methanol, ethanol, or benzyl alcohol can selectively scavenge photogenerated holes, suppress electron–hole recombination, and thereby enhance the overall photocatalytic performance. Similar to the ORR pathway, H₂O₂ can also be generated via the WOR route, in which photogenerated holes at VB participate in the oxidation process leading to H₂O₂ formation. The WOR pathway for H₂O₂ production can be categorized into two mechanisms: (i) a direct one-step 2h⁺ oxidation process, in which H₂O is oxidized by two holes to generate H₂O₂ at a potential of 1.76 V (Equation 5, Scheme 2), and (ii) an indirect two-step pathway, where oxidation of H₂O at the valence band (Equation 6, Scheme 2) produces $\bullet\text{OH}$ radicals that subsequently dimerize to form H₂O₂ (Equation 6, Scheme 2). However, the indirect route requires a much more positive potential (2.73 V), making it thermodynamically less favourable. In addition, WOR can also proceed via 4h⁺ oxidation of H₂O to form O₂ at the VB (Equation 7, Scheme 2), and the generated O₂ may subsequently participate in a cascade 2e⁻ ORR process to yield H₂O₂.

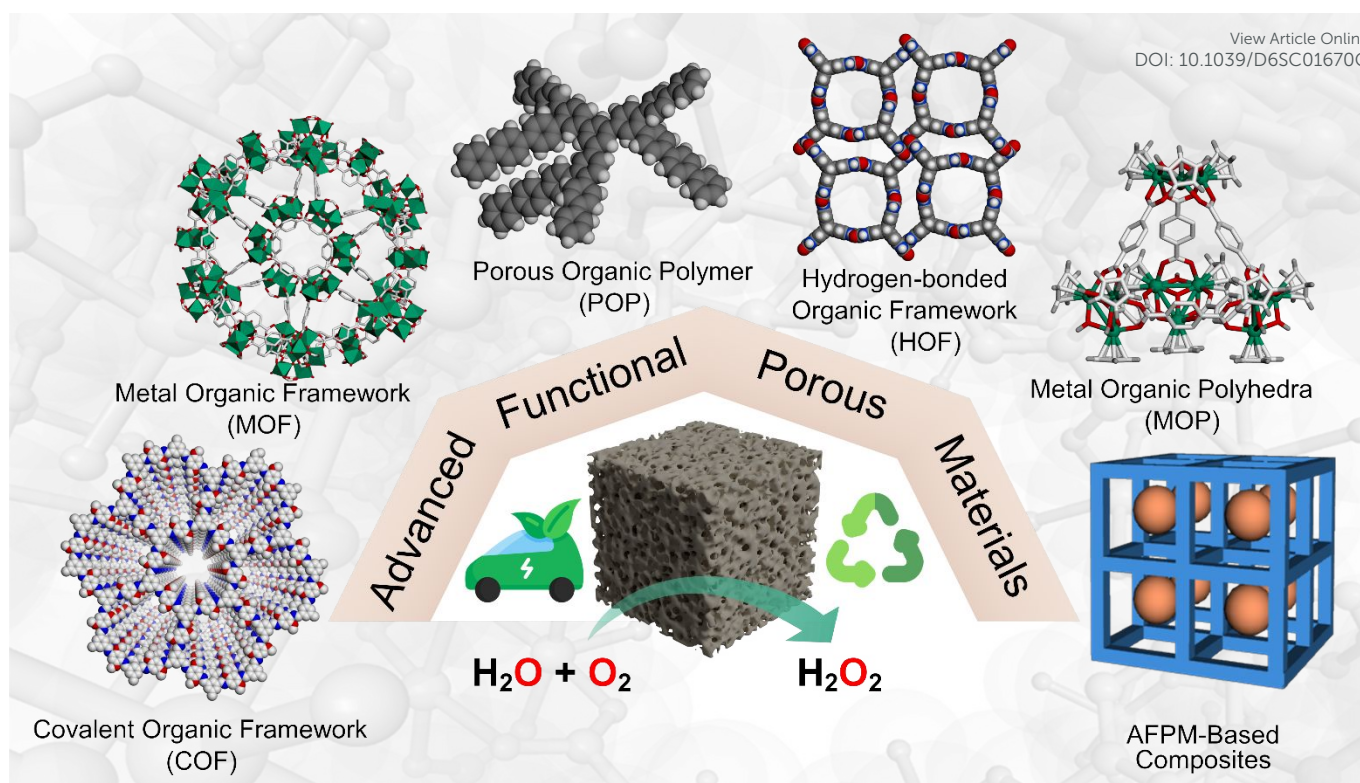


Scheme 2: Schematic illustration and energy diagram of the photocatalytic production of H₂O₂ over a photoactive COF-based material *via* the ORR pathway or WOR pathway, where potentials are given against the normal hydrogen electrode (NHE) at pH = 0.

Advanced functional porous materials (AFPM) as a photocatalyst:

An ideal photocatalyst exhibits a broad light absorption range, a suitable band gap, efficient charge separation, long-term stability, abundant active sites, and low cost. The pioneering work on photocatalysis was reported by Fujishima and Honda in 1972, where titanium dioxide was demonstrated as an n-type semiconductor for water splitting under UV radiation.⁴¹ Since then, great efforts have been devoted to this research area, and various photocatalytic reactions have been carried out. A primary focus has been devoted to developing inorganic semiconductors such as metal oxides,²³ metal sulfides,^{42,43} metal selenides quantum dots,⁴⁴ organic dyes,⁴⁵ etc. However, the practical applications of these photocatalysts are limited by the toxicity, high cost of rare metal components, and the inherent limitation of being non-recyclable. Additionally, many of them have a large band gap of approximately 3.2 eV and exhibit efficiency only under UV-light irradiation, which limits their use





Scheme 3: Representation of various advanced functional porous materials discussed in this review for photocatalytic H_2O_2 production.

under visible light, resulting in low photocatalytic efficiency and photocurrent quantum yield. Metal-free organic semiconductors such as graphitic carbon nitride ($\text{g-C}_3\text{N}_4$) have shown promising efficiency under visible light irradiation. Apart from being metal-free, these materials also possess intriguing properties, such as being earth-abundant, having an appropriate band gap of approximately 2.7 eV, and exhibiting high thermal and chemical stability.^{46,47} The suitable band structure also makes them ideal for constructing a type II heterojunction combined with other photoactive materials with large band gaps.⁴⁸ However, $\text{g-C}_3\text{N}_4$ has limited structural diversity and is typically synthesised through thermal polycondensation, which involves calcinating nitrogen-containing molecules at a temperature exceeding 600 °C.⁴⁹ In the quest for better photocatalysts, researchers are growing interested in exploring the photocatalytic performance of advanced functional porous materials (AFPMs). AFPMs refer to materials constructed from organic and/or inorganic building block units through various forces, such as coordination bonds, covalent and hydrogen bonds, etc. They exhibit standard features, including a high specific surface area, a periodic nanoporous structure, and tunable supramolecular structures. Following the reticular chemistry, there have been reports of new types of porous material that include metal-organic frameworks (MOFs), covalent-organic frameworks (COFs), porous organic polymers (POPs), covalent triazine frameworks (CTFs), metal-organic polyhedra (MOPs), and hydrogen-bonded organic frameworks (HOFs). Owing to its large surface area, these materials have been widely explored for separation and gas storage. However, research has also been propelled towards demonstrating its potential as an efficient photocatalyst.

Advantages of AFPMs-based photocatalysts:

In contrast to traditional semiconductors, functional porous materials exhibit common characteristics and several distinct advantages that make them particularly beneficial for photocatalysis. The main advantages of AFPMs are: (1) high surface area, which enables efficient mass transport, and their large pore channels, which allow molecules to pass through, resulting in more accessible active sites where substrates can bind and react. (2) Enhanced Light-Harvesting Capability where π -conjugated frameworks and chromophoric or semiconductive units enhance light harvesting by enabling broad visible-light absorption. (3) Tunable pore structure and morphology where hierarchical porosity could be introduced to enhance selective diffusion of solvents, mass transport, and better accommodation of reactants/products. (4) Tunable electronic structure, which can be tuned through functional groups or donor-acceptor units to adjust the bandgap, charge separation, and redox properties. (5) High functionalisation flexibility that enables diverse post-synthetic modifications for easy incorporation of catalytic sites, creation of polar environments, and tuning of surface charge. (6) Structural stability and reusability of many AFPMs arise from their chemical robustness and thermal stability, enabling long-term cycling without loss of activity. With all these intriguing properties, AFPMs have been extensively applied to photocatalysis, especially MOFs and COFs. The pioneer work of Zecchina's group in 2004 showed Zn_4O_{13} clusters in MOF-5 to behave similarly to ZnO quantum dots (QDs).⁵⁰ In 2007, Garcia and coworkers reported the first report of MOF towards photocatalysis using MOF-5 as a photocatalyst for phenol degradation.⁵¹ Extensive research has been carried out after that, and the progress of MOF as a photocatalyst



has been summarised in many reviews.^{52–54} Similarly, the first report of COF towards photocatalysis was recorded in 2010 by Müllen and coworkers, where COF has been identified as a novel poly-(azomethine) network (ANW) and explored towards photocatalytic H₂ evolution.⁵⁵ Recent advances in using COF as a photocatalyst have been summarised in various reviews.^{56,57} Towards photocatalysis, MOFs that are constructed via metal nodes coordinated to organic ligands have large band gaps, which are not feasible for photocatalysis reactions or require high energy to generate an electron-hole pair. Conversely, COFs present a significant opportunity to address the aforementioned challenges at the photocatalyst level. Furthermore, the metal-free nature makes it a more favourable catalyst in terms of environmental considerations. However, the synthesis complexity and photostability are major challenges in using COF as a photocatalyst. POPs are also popular photocatalysts for wide photocatalytic applications.^{58,59} However, its amorphous nature is a major challenge as non-crystalline materials typically exhibit poorer photocatalytic performance, due to the defects in the structure which disrupt conjugation and hinder efficient charge separation and migration. Various types of AFMSs exhibit distinct characteristics in terms of monomer structure, preparation methods, and optical properties, and each presents its own set of challenges. Different approaches enhancing the performance of AFPMs have been proposed, which include methods such as ligand functionalization, mixed-metal/linker strategies, metal ion/ligand immobilisation, metal nanoparticle loading, semiconductor coupling, composite synthesis, etc. In this review, we discuss the photocatalytic applications of various AFPMs, with a focus on H₂O₂ production, and relate their photocatalytic performance to the structural and electronic properties of their compositional components.

AFPMs-based photocatalysts for H₂O₂ production:

As the demand for H₂O₂ continues to rise and the search for environmentally friendly production methods intensifies. Several well-known semiconductors, such as metal oxide and g-C₃N₄, have garnered significant attention towards photocatalytic H₂O₂ production.^{23,60} Metal oxides such as TiO₂ serve as a benchmark photocatalyst for H₂O₂ production through two-electron oxygen reduction under UV/visible light irradiation. Due to the wide band gap of TiO₂, it has often been combined with other materials to form a composite appropriate for H₂O₂ photosynthesis. Modifications such as Au-Ag or Pd cocatalysts enhance charge separation and selectivity for H₂O₂ production on TiO₂ and achieve yields up to 3.6 mM.⁶¹ Similarly, BiVO₄ has also shown efficiency for H₂O₂ production through 2e⁻ ORR pathways due to the favourable alignment of its conduction band edge.⁶² Similar to metal oxides, modified metal sulfides have also shown promising efficiency for H₂O₂ production. 2D layered materials such as g-C₃N₄ also serve as the standard metal-free benchmark for photocatalytic H₂O₂ production, achieving ~20–30 μmol h⁻¹ (pure water/O₂) via 2e⁻ ORR due to its suitable conduction band (-0.4 to -1.0 V vs. NHE) for ·O₂⁻ formation, though limited by poor WOR (VB ~+1.7 V) and recombination, yielding a

apparent quantum yield (AQY) of ~0.5–2% at 420 nm.⁶³ Beyond conventional photocatalysts, lignin, one of the most abundant renewable aromatic biopolymer resources, has also recently been reported as an effective photocatalyst for H₂O₂ production.⁶⁴ In the past few years, there has been a notable increase in research focused on using porous materials for photocatalytic H₂O₂ production. The statistical data obtained by searching phrases "Photocatalytic Production of Hydrogen Peroxide" OR "H₂O₂" AND "Porous" OR "Frameworks" as title in the Web of Science database is shown in Figure 1. Tremendous development has been made in enhancing the photochemical efficiency of AFPMs towards light-driven H₂O₂ production, and it is well documented in various reviews.^{30,65–69} While previous reviews have extensively documented and discussed the progress of porous materials in photocatalytic H₂O₂ production, they typically focused on a single type of AFPM. In contrast, detailed reviews that collectively examine the progress and advances across all functional porous materials remain limited. Capitalising on this opportunity, the present work provides a unified and critical discussion of photocatalytic H₂O₂ production using a broad range of porous frameworks, including COFs, MOFs, POPs, CTFs, HCPs, HOFs, MOPs, and their composite systems. Considering the large volume of publications in this field and the fact that many earlier advances have already been comprehensively covered in previous reviews, this manuscript focuses on literature published between 2024 and 2025. Furthermore, the review highlights the key opportunities and challenges associated with AFPM-based photocatalysts, with particular emphasis on the synthetic technique of AFPM photocatalysts, scalability toward practical applications, long-term photostability, long-term H₂O₂ production, and efficiency limitations. All AFPMs have been discussed as individual topics/subtopics for the readers. The review also provides the perspective and recommendations for the future progress of this field.

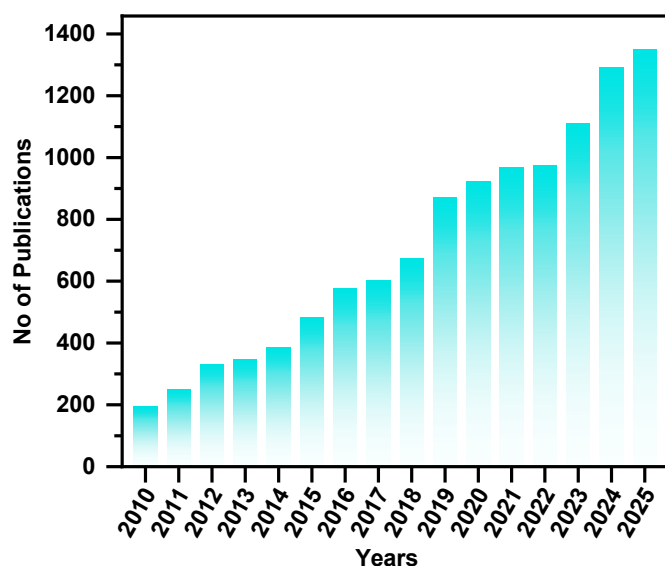


Figure 1: Bar chart of the number of articles per year concerning photocatalytic hydrogen peroxide production by advanced functional porous materials (accessed 21 January 2026). The statistical data were obtained by searching the phrases "Photocatalytic Production of Hydrogen Peroxide" OR "H₂O₂" AND "Porous" OR "Frameworks" in the Web of Science database, and the numbers correspond to the final publication year



Covalent organic frameworks (COFs) based photocatalysts towards H₂O₂ production:

COFs are porous materials composed of organic building blocks connected by strong covalent bonds. The covalent bonds are synthesised due to reactions like condensation, forming highly ordered, crystalline structures with large surface areas and tunable pore sizes (Figure 2a). Since the pioneering work by Yaghi and co-workers⁷⁰ in 2005, it has attained significant interest in terms of synthesis and applications.^{71–73} Owing to their well-defined⁷⁴ structures, high crystallinity, permanent porosity, unlimited tenability, metal-free nature, and appreciable stability, COFs have been established as a promising material for catalysis,^{75,76} capture and separation,^{77,78} energy materials,^{79,80} bio application,⁸¹ sensing,^{82,83} pollutant degradation,⁸⁴ CO₂ reduction⁸⁵ etc. In particular, enhanced charge separation, excellent light-harvesting capabilities, conjugated structures, semiconductor nature, and an opportunity to tune the band gap have made COF an interesting photocatalyst material. The first semiconductor behaviour of COF was reported by Jiang et al., with boronic ester COF.⁸⁶ Later, in 2014, Stegbauer et al. explored the efficiency of a hydrazine-based COF in producing hydrogen from pure water upon irradiation with visible light, marking the first application of COF as a photocatalyst. COFs exhibit various intrinsic features that make them ideal for photocatalytic applications, including their crystalline, porous structure for efficient charge transport, extended π -conjugation for enhanced light absorption, and a high surface area that provides abundant active sites. Their modular design enables the precise tuning of electronic properties through the incorporation of functional groups, while excellent chemical and thermal stability ensure durability during photocatalytic reactions. To date, extensive research has reported the use of COFs as efficient metal-free heterogeneous photocatalysts for various applications, including CO₂ reduction, organic transformations, H₂ evolution, ammonia synthesis, and pollutant degradation.^{87,88} The photocatalytic application of COFs towards H₂O₂ production was pioneered by Voort and coworkers in 2020, with a series of 2D imine-based COFs.⁸⁹ Since then, various strategies have been implemented to improve the photocatalytic efficiency of COFs. To be precise, donor-acceptor optimisation, functional group incorporation, linkage modification, topological and structural modification and post-synthetic

modification (PSM), are some of the important areas that can severely impact the photocatalytic efficiency of COF (Figure 2b). These strategies have been meticulously discussed as subtopics in this review.

Donor-acceptor (D-A) COF for photocatalytic H₂O₂ production:

The donor-acceptor (D-A) architecture is an inherent property of COF. The monomers, often comprising aromatic and π -electron-rich moieties, typically act as donors, while functionalities containing electron-deficient groups generally serve as acceptors. The alternating arrangement of D-A units in COFs enables band gap tunability, enhances charge transport, and promotes efficient electron-hole separation, collectively leading to improved photocatalytic performance.⁹⁰ D-A moieties within the framework also create a strong push-pull effect that promotes efficient charge separation and transfer. This effect lowers the electrostatic attraction between photogenerated carriers, thereby improving overall charge-separation efficiency. Further, COFs designed with D-A configurations exhibit a markedly lower exciton binding energy compared to their symmetric counterparts.⁹¹ The strong intraframework charge-transfer interactions shift electron density from the donor units toward the acceptor domains upon photoexcitation, generating a built-in electric field that spatially separates charge carriers. This separation reduces the Coulombic attraction between electrons and holes, thereby facilitating rapid exciton dissociation into free carriers. Consequently, D-A COFs display enhanced charge mobility, suppressed recombination, and improved photocatalytic efficiencies. Various D-A COFs have been reported recently that possess superior activity towards photocatalytic H₂O₂ production. For instance, considering the large π -conjugated structure, excellent light-harvesting abilities, and electron donor capabilities of pyrene moieties, Voort and group reported the synthesis of four novel pyrene-based COFs.⁹² The π -electron-rich pyrene acts as a donor, and its combination with an appropriate electron acceptor monomer has been found to be efficient towards H₂O₂ production, with a rate of 1242 $\mu\text{mol g}^{-1} \text{h}^{-1}$ at the biphasic system (benzyl alcohol and water). The biphasic system has also been advantageous as it successfully inhibited the breakdown of H₂O₂ and facilitated efficient photocatalytic generation of H₂O₂.

Modulating the D-A property of COF through linkage chemistry toward H₂O₂ production has been thoroughly examined by Jiang et al. Using a hexaphenyl triphenylene donor and a benzothiadiazole acceptor, they constructed hexavalent COFs featuring hydrazone, imine, or cyano-vinylene linkages (Figure 3a).⁹³ These materials possess sites that enable both 2e⁻ ORR and 4e⁻ WOR, allowing concurrent formation of H₂O₂ and O₂. Among the linkages, the hydrazone bridge provided the most favourable characteristics, including superior stability, higher polarity, and abundant adsorption sites for water and oxygen (Figure 3b). As a result, Hz-TP-BT-COF delivered the highest H₂O₂ production rate (5.7 mmol g⁻¹ h⁻¹),

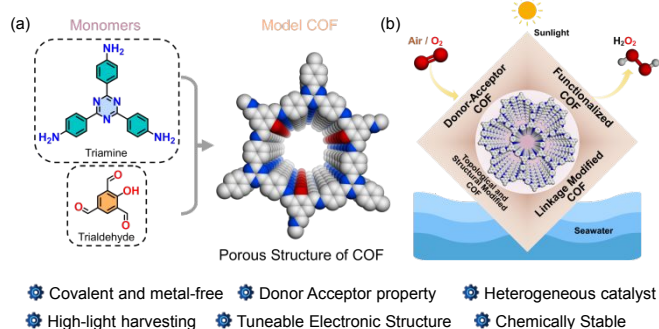


Figure 2: (a) Model reaction for COF formation through a condensation reaction. (b) Practices in COFs, discussed in this review, to enhance photocatalytic H₂O₂ production.



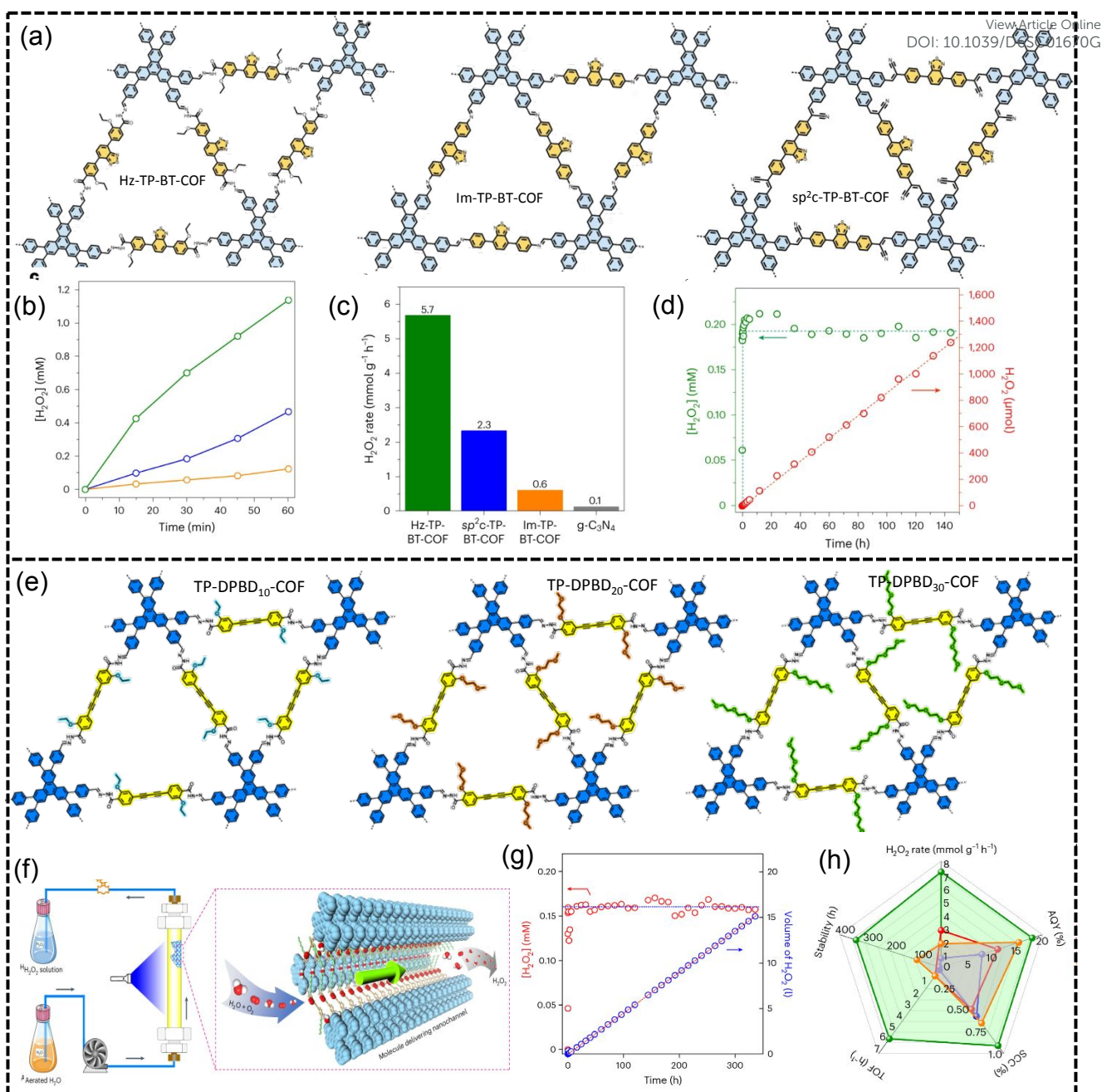


Figure 3: (a) Structural representation of Hz-TP-BT-COF, IM-TP-BT-COF, and sp²c-TP-BT-COF (b) (c) Photocatalytic H₂O₂ production comparison of synthesised catalyst with benchmark g-C₃N₄. (d) Continuous H₂O₂ production up to 6480 mL within 140 h with Hz-TP-BT-COF. (Reproduced and reprinted with permission from the Ref.⁹³ Copyright 2024, Springer Nature). (e) Structural representation of TP-DPBD₁₀-COF, TP-DPBD₂₀-COF, and TP-DPBD₃₀-COF (f) representation of WOR and ORR active sites in TP-DPBD₃₀-COF, and (g) Schematic illustration of the production of H₂O₂ solution through continuous photocatalysis in a flow reactor. (Reproduced and reprinted with permission from the Ref.⁹⁴ Copyright 2024, Springer Nature).

significantly outperforming the imine-linked (0.6 mmol g⁻¹ h⁻¹) and vinylene-linked (2.3 mmol g⁻¹ h⁻¹) analogues (**Figure 3c**) without sacrificial agents alongside an apparent quantum yield (AQY) of 17.5% and a TOF of 4.2 h⁻¹ at 420 nm. All synthesised COFs also show better performance towards photocatalytic H₂O₂ production compared to the benchmark g-C₃N₄ catalyst (**Figure 3c**). The hexavalent hydrazone-linked COF also demonstrated the continuous photosynthesis of H₂O₂ in flow reactors with air-saturated water, reporting a record-high yield of 6,480 mL of H₂O₂ over 144 h (**Figure 3d**). Building on their earlier success with hydrazone-linked

hexavalent COFs, the same group advanced their H₂O₂ photosynthesis strategy by designing a new series of hexavalent D-A COFs through precise tuning of π -frameworks and pore environments.⁹⁴ In this design, diphenylbutadiyne units replaced benzothiadiazole as the electron-accepting component. Besides serving as an active site for the 2e⁻ oxygen-reduction process, the hydrophobic diphenylbutadiyne motif discourages water adsorption and promotes spontaneous oxygen enrichment within the pores. The overall hydrophobicity of the COFs was further modulated by extending the ether side chains on the linker (**Figure 3e**). Under



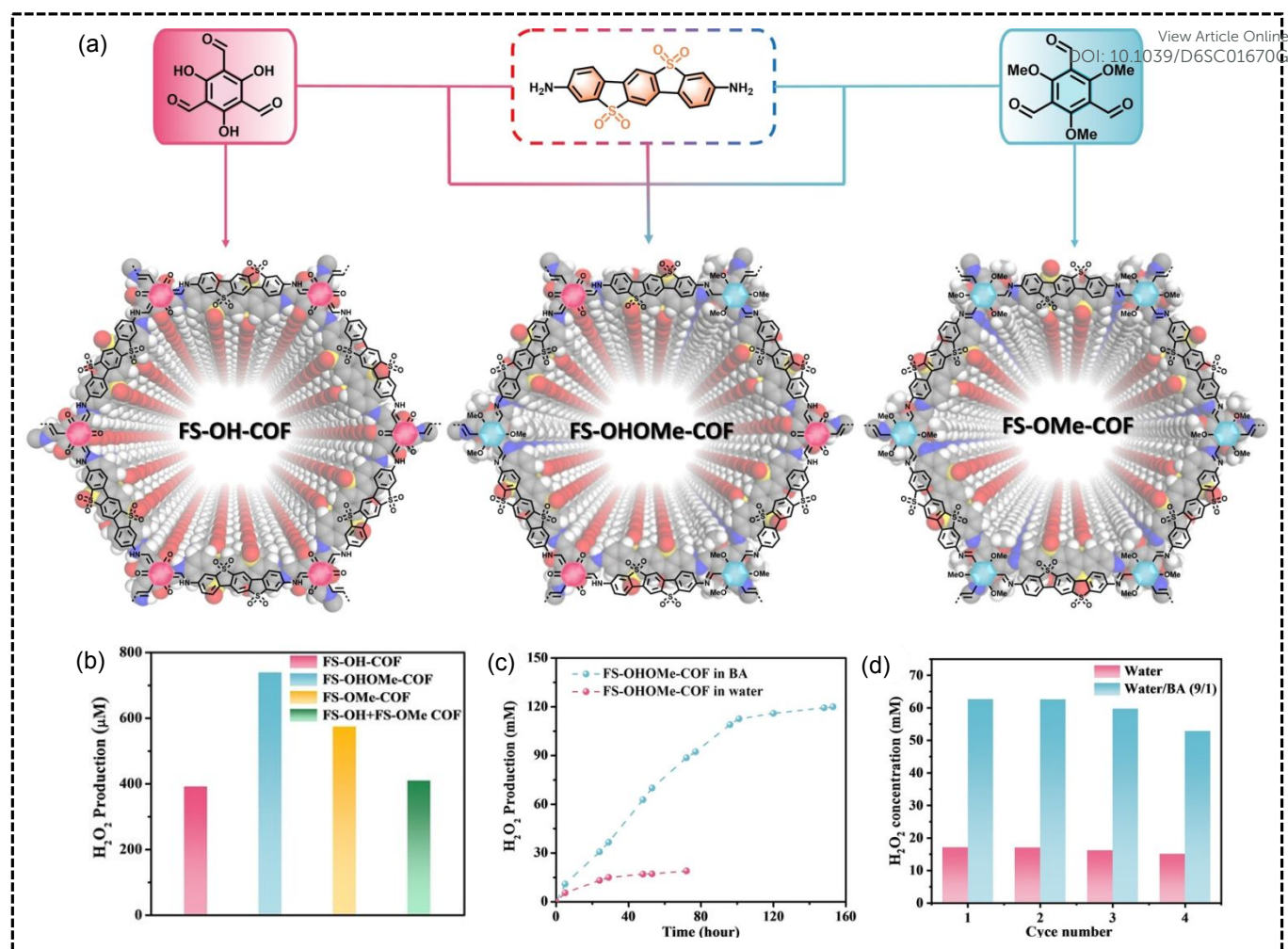
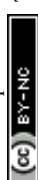


Figure 4: (a) synthesis scheme and structure of FS-COF. (b) H₂O₂ production comparison of different FS-COF. (c) Long-term stability of FS-OHOMe-COF in benzyl alcohol (BA) and water over 160 h. (d) Performance of recycled FS-OHOMe-COF in benzyl alcohol (BA) and water over four cycles. (Reproduced and reprinted with permission from Ref.⁹⁵ Copyright 2024, Wiley-VCH GmbH)

visible light in pure water, the resulting COFs delivered H₂O₂ at rates of 7.2, 5.9, and 3.4 mmol g⁻¹ h⁻¹ for TP-DPBD₃₀-COF, TP-DPBD₂₀-COF, and TP-DPBD₁₀-COF, respectively, consistent with a 2e⁻ ORR mechanism. When exposed to natural sunlight, TP-DPBD₃₀-COF maintained a high activity of 3.4 mmol g⁻¹ h⁻¹. Their practical potential was demonstrated in a continuous-flow reactor (Figure 3f), which produced 15.1 L of H₂O₂ solution (0.16 mM) over two weeks/336 hours, highlighting the scalability of this COF-based system (Figure 3g). The overall performance of TP-DPBD-COF has been shown through a radar plot (Figure 3h), which highlights the production, solar-to-chemical conversion (SCC), AQY, stability, and turnover frequency (TOF) during photocatalytic H₂O₂ production. Tuning the D-A acceptor property of COF by the introduction of a heteroatom is one of the well-known strategies. The thiophene-S units are well known for ORR, and its increased density within the COF enhances the ORR efficiencies.⁹⁶ The study performed by Wang et al demonstrates the photocatalytic efficiency of benzenetri thiophene (Btt)-based COF towards H₂O₂ production.⁹⁷ Three D-A COF (TpaBtt, TapbBtt, and TaptBtt) have been reported by combining sulphur-rich Btt-based aldehyde with different types of triphenylamine (Figure 4a). The synthesised COF acquired a dual D-A structure that

promotes an appropriate energy band position and a feasible intermediate anion towards H₂O₂ photosynthesis. Under visible light irradiation, TaptBtt with triazine core produced a high rate of H₂O₂ 2111 μM h⁻¹ in pure water and air with an SCC of 0.296%. Similarly, Cao et al. reported that BBT-ACN COF-1, synthesised via a Knoevenagel condensation between benzotri thiophene (BTT) and benzo[1,2-d;4,5-d']bisthiazole (BBT), exhibits higher efficiency for photocatalytic H₂O₂ production than BBT-ACN COF-2, which is formed by coupling conjugated pyrene aldehyde with BBT.⁹⁸ Both COFs are sp²-carbon-linked and have distinct D-A properties. BBT-ACN COF-1 features a D-A structure with BBT as the acceptor and BTT as the donor, whereas BBT-ACN COF-2 adopts a π-A architecture with pyrene as the π-unit and BBT as the acceptor. The thiophene-containing COF for photocatalytic H₂O₂ production has also been reported by Yue et al.⁹⁹ By regulating the N-heteroatom into the framework, they have synthesised two thiophene COFs (TD-COF and TT-COF). The regulation in N atoms has brought differences in their wettability, as TD-COF is super hydrophilic and TT-COF has a hydrophobic nature. Consequently, the TD-COF demonstrated H₂O₂ production of 4060 and 3364 μmol g⁻¹ h⁻¹ in deionised water and seawater, both of which are higher than those of TT-COF. The



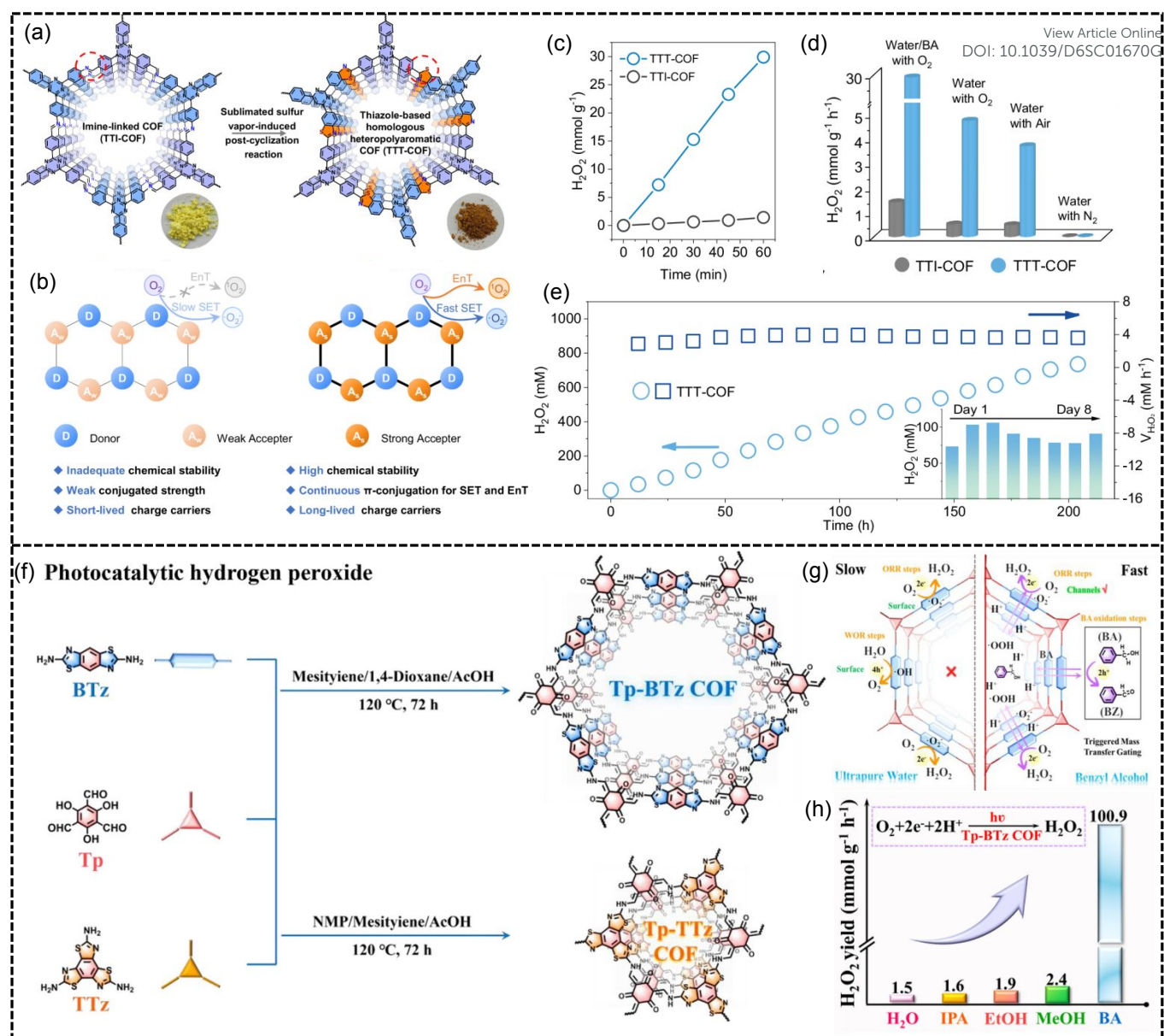


Figure 5: (a) Schematic illustration of the synthesis of thiazole-based homologous heteropolyaromatic COFs. (b) Representation of D-A moieties and the structural advantages of homologous heteropolyaromatic COFs. (c) Time-dependent photocatalytic activity of TTI-COF and TTT-COF for H_2O_2 production (d) Photocatalytic H_2O_2 production TTI-COF and TTT-COF under different conditions. (e) Long-term H_2O_2 production of TTT-COF (inset: daily yield over eight days). (Reproduced and reprinted with permission from Ref.¹⁰⁰ Copyright 2025, Springer Nature). (f) Schematic illustration of the synthesis of Tp-BTz COF and Tp-TTz COF. (g) H_2O_2 production through mass-transfer gating (MTG). (h) Photocatalytic H_2O_2 production with Tp-BTz COF in different solvents. (Reproduced and reprinted with permission from Ref.¹⁰¹ Copyright 2025, Wiley-VCH GmbH)

mechanistic pathway revealed the photocatalytic production of H_2O_2 through indirect 2e^- ORR and direct 2e^- WOR dual pathways, where thiophene is likely the photo-reduction unit, while benzene is the probable photo-oxidation unit. Beyond simple D-A assemblies in COFs, incorporating multiple D-A moieties has been shown to further enhance photochemical efficiency. As shown by Shu et al., multiple donor-acceptor-acceptor (D-A-A) type FS-OHOMe-COF shows more efficiency for H_2O_2 production compared to FS-OH-COF and FS-Ome-COF, which have simple D-A units (Figure 4a).⁹⁵ The presence of the sulfone group within the COF linker serves as an active site and enhances stability by strengthening interlayer forces. Furthermore, compared to the pristine COF mixed ligand strategy, the synthesised FS-OHOMe-COF structure features extended π - π conjugation, long

excited-state lifetime, low exciton binding energy, and high photostability. The H_2O_2 production rate of FS-OHOMe-COF measures a production rate of 1.0 mM h^{-1} in O_2 -saturated water under visible light irradiation, which is higher than that of its pristine counterpart (Figure 4b). Further, the AQY of 9.6% at 420 nm, and an SCC of 0.58% was also observed. Most reported photocatalysts generate only very low H_2O_2 concentrations, typically below 2 mM, far from the levels needed for practical use. In contrast, FS-OHOMe-COF demonstrated steady and long-term accumulation of H_2O_2 , achieving 19 mM in pure water after 72 h of irradiation. When benzyl alcohol was added, the concentration further increased to 120 mM after 153 hours, although part of this enhancement may arise from autocatalytic H_2O_2 formation associated with BA (Figure 4c). Further,



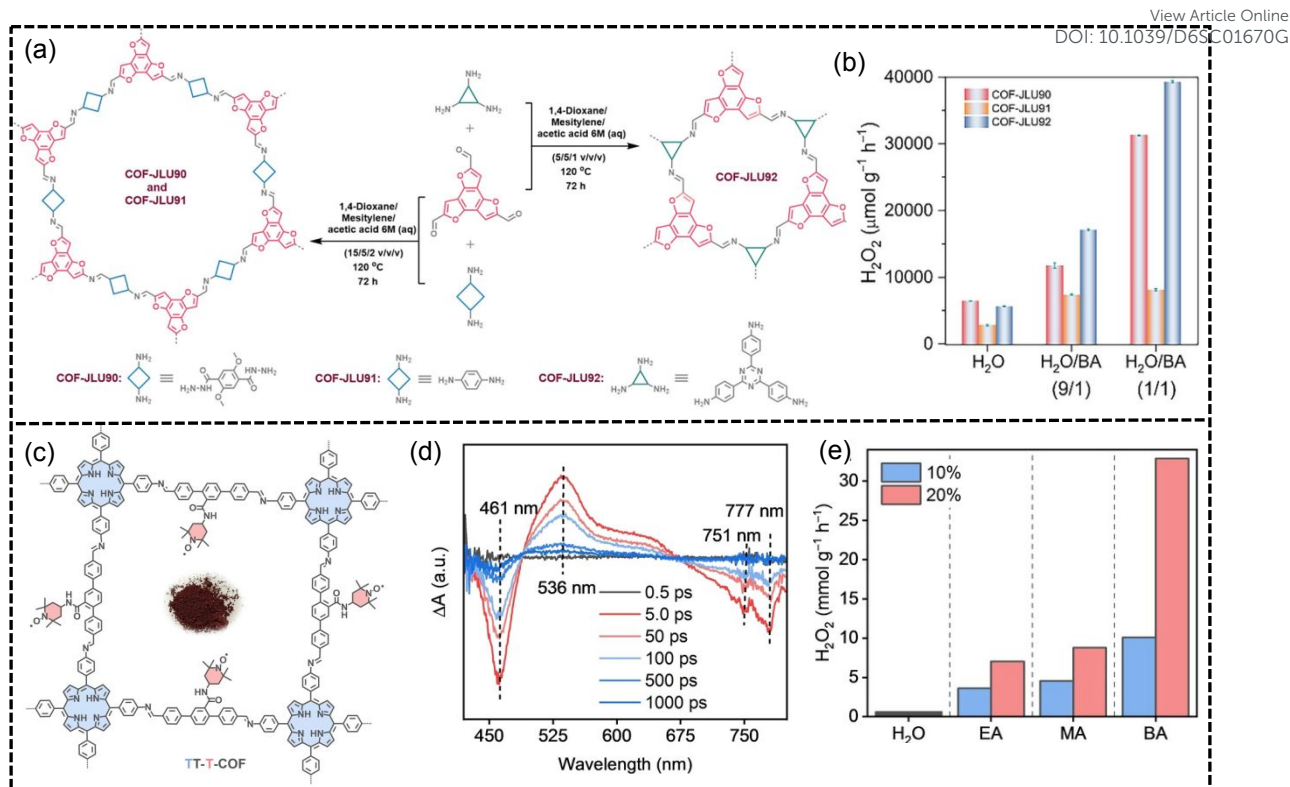


Figure 6: (a) Schematic illustration of the synthesis of oxygen-rich COF-JLU. (b) Photocatalytic H₂O₂ production with COF-JLU in pure water and BA. (Reproduced and reprinted with permission from the Ref.¹⁰² Copyright 2025, Wiley-VCH GmbH). (c) Schematic illustration of the synthesis of TEMPO decorated TT-T-COF. (d) Photocatalytic H₂O₂ production with COF-JLU in different conditions. (Reproduced and reprinted with permission from the Ref.¹⁰³ Wiley-VCH GmbH).

the recyclability up to four cycles has been demonstrated by FS-OHOMe-COF in both pure water and BA (Figure 4d). The importance of the S-atom towards improving various properties of the COF photocatalyst has also been demonstrated by Cheng and coworkers.¹⁰⁰ They constructed a heteropolyaromatic TTT-COF by introducing thiazole units through a post-cyclisation reaction (Figure 5a), which resulted in three key improvements (Figure 5b): (i) markedly higher chemical stability, (ii) a fully extended π -conjugated framework that supports efficient single-electron and energy-transfer processes, and (iii) increased intramolecular polarity that strengthens the D-A character and promotes charge separation. Owing to these features, TTT-COF shows far superior stability, conjugation, and photocatalytic performance compared to its imine-linked counterpart, TTI-COF. Consequently, using 10% benzyl alcohol, TTT-COF produces H₂O₂ at 29.9 mmol g⁻¹ h⁻¹, which is about 20 times higher than the imine-linked COF and superior to many state-of-the-art photocatalysts (Figure 5c-d). TTT-COF shows excellent durability, operating continuously for over 200 h with no significant loss in photocatalytic activity (Figure 5e). Thiophene-based COFs are generally effective for H₂O₂ production. Notably, when thiophene density was tuned using bis and tris(thiazole) amines, the bis(thiazole)-based COF showed higher H₂O₂ production efficiency.¹⁰¹ Qiao et al. reported two COFs—Tp-BTz and Tp-TTz (Figure 5f) and assessed their H₂O₂ production using a mass-transfer-gating (MTG) (Figure 5g) strategy based on sacrificial agents. The MTG approach improves interfacial reactions by easing mass-transport constraints, increasing access to catalytic sites, scavenging photogenerated holes, and providing protons for downstream coupling steps.

Introducing benzyl alcohol (BA) into the system activated a catalytic mode-switching behaviour, dramatically boosting performance. Under 10% BA and O₂-saturated conditions, Tp-BTz COF delivered a record H₂O₂ production rate of 100.9 mmol g⁻¹ h⁻¹, outperforming state-of-the-art photocatalysts and exhibiting 1.8-fold higher activity than Tp-TTz COF (Figure 5h). Also, the AQY of these COF at 420 nm were calculated to be 18.0% and 16.5%, and SCC efficiency evaluated using a solar simulator (AM 1.5G), yields values of 1.47% and 0.72% for Tp-BTz for Tp-BTz COF and Tp-TTz COF, respectively. Sulfur-containing thiophene unit has moreover served as an electron-accepting site for the reduction of oxygen during H₂O₂ production. However, the electron donor strength of sulfur-containing moieties with the COF framework has also been explored and found to be efficient for H₂O₂ production. Voort and coworkers¹⁰⁴ report the synthesis of three D-A COFs (TMT-TT, TMT-N, and TMT-BT) by combining the triazine (TMT) unit with aldehydes containing either thienothiophene (TT), naphthalene (N), or benzothiazole (BT) moieties, where the TT unit, with its two sulfur groups, exhibited the highest donor strength, followed by N and BT, with the electron-donating ability following the order: TT > N > BT. Therefore, with the D-A property in synthesised COF, the H₂O₂ production rates in the O₂-purged pure water system were measured to be 1952, 1742, and 748 $\mu\text{mol g}^{-1} \text{h}^{-1}$ for TMT-TT, TMT-N, and TMT-BT-COF, respectively. The presence of nitrogen can also play a significant role in improving charge-carrier transport. As shown by Zhang et al., the systematic regulation of nitrogen atoms within the framework modulates the electron-accepting capacity of COF.¹⁰⁵ Regulating the nitrogen content in COFs leads to a well-defined D- π -A architecture. A higher



Table 1: Summary of the representative D-A COFs photocatalysts in H₂O₂ photosynthesis.View Article Online
DOI: 10.1039/D6SC01670G

Sl. No	Catalyst	Reaction condition	Cat. Dosage (mg) & Solvent volume (mL)	H ₂ O ₂ Yield (μmol g ⁻¹ h ⁻¹)	AQY	SCC	Ref
1.	Py-Py COF	H ₂ O: BA (9:1)	10 mg & 20 mL	1242	4.5% @ 420 nm	-	92
2.	H ₂ -TP-BT-COF	H ₂ O	3 mg & 15 mL	5700	17.5% @420 nm	-	93
3.	TP-DPBD ₃₀ -COF	H ₂ O	2.5 mg & 15 mL	7200	18% @420 nm	0.91%	94
4.	FS-OHOMeCOF	H ₂ O	10 mg & 20 mL	1100 μM h ⁻¹	9.6% @420 nm	0.58%	95
5.	TaptBtt-COF	H ₂ O	15 mg & 50 mL	1407	4.6% @ 450 nm	0.296%	97
6.	BBT-ACN COF-1	H ₂ O	5 mg & 50 mL	2500	3.12%@420 nm	-	98
7.	TD-COF	H ₂ O and O ₂	1 mg & 4 mL	4620	-	0.15%	99
8.	TTT-COF	H ₂ O:BA (9:1)	5 mg & 45 mL	29905	12% @ 400 nm	0.32%	100
9.	TP-BTz COF	H ₂ O:BA (9:1)	5 mg & 20 mL	100864	18% @ 420 nm	1.47%	101
10.	COF-JLU92	H ₂ O:BA (1:1)	5 mg & 50 mL	39283.3	15.4%@ 420 nm	2.35%	102
11.	TT-T-COF	H ₂ O:BA (9:1)	5 mg & 25 mL	10066	19.2%@ 420 nm	-	103
12.	TMT-TT-COF	H ₂ O and O ₂	10 mg & 30 mL	1952	-	-	104
13.	Tf-TAPT-COF	H ₂ O and O ₂	10 mg & 50 mL	2700	2.48%@ 420 nm	-	105
14.	TTF-BT-COF	H ₂ O and O ₂	5 mg & 10 mL	2.76mM g ⁻¹ h ⁻¹	11.19%@420nm	0.49%	106
15.	JUC-65	BAm, O ₂ and ACN	5 mg & 10 mL	22800	15.7%	1.09%	107
16.	COF-2	Seawater	5 mg & 50 mL	6930	2.5% @420 nm	0.26%	108
17.	TACOF-1-COOH	H ₂ O and O ₂	2.5 mg & 18 mL	3542	5.7% @420 nm	0.55%	109

Light Irradiation: λ>420 nm, BA: Benzyl alcohol, BAm: BA: Benzyl amine, ACN: acetonitrile

density of nitrogen atoms in the heterocyclic units strengthens charge migration along the π-conjugated pathway. As a result, these COFs can promote ORR through both the π-bridge and acceptor centres, while WOR proceeds at the donor sites. This synergistic division of functions greatly enhances their overall efficiency in photocatalytic H₂O₂ generation. Notably, Tf-TAPT-COF with triazine unit can reach H₂O₂ production of 2700 mmol g⁻¹ h⁻¹ from water and O₂.

Apart from sulfur and nitrogen-containing COFs, oxygen-rich frameworks have also demonstrated notable efficiency in H₂O₂ photosynthesis. In particular, benzotriuran-based COF-JLU92 (Figure 6a) featuring an electron D-A character with a hydrazone linkage has been reported by Zhang et al for photocatalytic H₂O₂ production.¹⁰² The partially separated D-A π-stacks in benzotriuran-based COF promote efficient charge separation and provide active sites for O₂ reduction and H₂O oxidation. Also, 1D heteroatom-rich pores within the framework enhance water transport and lower the energy barrier for oxidation, enabling high H₂O₂ production rates of up to 9800 μmol g⁻¹ h⁻¹ from water and oxygen with AQY of 8.7% at 450 nm. Varying the ratio of water to benzyl alcohol from 9:1 to 1:1, the H₂O₂ production rate drastically increased from 17089 to 39284 μmol g⁻¹ h⁻¹ (Figure 6b). The high yield of H₂O₂ in BA was also recently reported with nitroxyl radical decorated TT-T-COF.¹⁰³ Owing to the presence of an unpaired electron in 2,2,6,6-Tetramethylpiperidine N-oxyl (TEMPO), it has been used as a nitroxyl radical mediator within COF (Figure 6c). TEMPO-based COF TT-T-COF showed good crystallinity and has a Brunauer-Emmett-Teller (BET) surface area of

88.48 m² g⁻¹. The radical-based D-A architecture in TT-T-COF promoted efficient separation of photogenerated electron-hole pairs, extends charge lifetimes, and enhances overall electron utilisation. However, COFs incorporated with TEMPO have band edges suitable for ORR but not for WOR (2e- or 4e-). Femtosecond transient absorption (fs-TA) studies reveal that TT-T-COF undergoes ultrafast charge-separated state (CSS) formation (<5 ps) upon 365 nm excitation, as evidenced by characteristic ground-state bleaching (GSB, ~461 nm) and excited-state absorption (ESA, ~536 nm) signals (Figure 6c). The rapid ESA evolution indicates efficient intramolecular electron transfer from the TAPP donor to the TEMPO acceptor within the D-A framework. Notably, incorporation of the redox-active TEMPO unit significantly prolongs the photogenerated electron lifetime (~671 ps), highlighting enhanced charge separation and carrier utilisation compared to conventional COFs. The photocatalytic H₂O₂ production rate of 10066 and ~34000 μmol g⁻¹ h⁻¹ in 10% and 20% BA under light irradiation >420 nm was noted for TT-T-COF (Figure 6d). In situ diffuse reflectance infrared Fourier transform spectroscopy (in-situ DRIFTS) showed the increase in the intensity at 1178 cm⁻¹, 809 cm⁻¹, and 850 cm⁻¹ corresponding to *OOH and HO-OH bonds, respectively. Combined theoretical and experimental (in situ DRIFTS) investigations demonstrate that the enhanced ORR activity and stability of TT-T-COF arise from the participation of the nitroxyl radical (N-O•). The redox-active site modulates local electron density and facilitates selective O₂ adsorption via a Yeager-type direct 2e- ORR pathway.



COF with different functional groups for photocatalytic H₂O₂ production:

The profound opportunity to synthesise COFs with various functional groups represents one of the most important advancements in the field. Functional group modification in COFs involves altering the chemical groups attached to the framework to enhance its properties or tailor its functionality. The customisation of desired functional groups within the framework can enhance the electronic characteristics of COFs, boosting their ability to absorb visible light and improving charge separation efficiency. The nature of substituents on COF linkers plays a decisive role in dictating both framework characteristics and catalytic behaviour. Fluorinated groups, for instance, can reshape the crystallinity, pore environment, and acid-base properties, ultimately influencing oxygen-reduction pathways and light-driven activity.¹¹⁰ In contrast, hydroxyl functionalities help capture photogenerated holes and suppress charge-recombination events, thereby improving durability.¹¹¹ Cyanide units steer the oxygen activation pathway by favouring the generation of singlet oxygen (¹O₂) instead of superoxide species.¹¹² Additionally, the functional modifications can increase the stability of COFs under various operational conditions, ensuring reliable performance over time. Moreover, the strategic addition or removal of groups facilitates efficient charge transfer, minimising the recombination of electron-hole pairs and increasing the production of H₂O₂.

The functionalization of COF with heteroatoms (N, O, S) has a profound effect towards enhancing the photocatalytic activity.¹¹³ The presence of heteroatoms alters the electronegativity of adjacent carbon atoms, potentially making these carbon atoms catalytically active as well. Moreover, the inherent hierarchy in electronegativity among the three heteroatoms significantly influences the resulting framework characteristics. In addition to the type of heteroatom present, its density and spatial arrangement within the framework also play critical roles in modulating the charge-transfer dynamics of COFs.¹¹⁴ Some studies show that COFs containing nitrogen-rich triazine, heptazine, can rationally induce the electrophilicity and results in more efficient ORR, forming H₂O₂.¹¹⁵ The effect of different nitrogen content in COF for photocatalytic H₂O₂ production has been demonstrated by Zhang et al.¹¹⁶ Two photoactive COFs (COF-JLU51 and COF-JLU52) were synthesised *via* Schiff base condensation reaction between [1,2,4]-triazolo-[1,3,5]-triazine (TTT) and triphenylbenzene as a building block. COF-JLU51 and COF-JLU52 have nitrogen content of 23.01 wt% and 26.79 wt%, respectively. TTT moieties are strong electron-withdrawing in nature, and their combination with electron-donating triphenylbenzene has constructed an optimum electron D-A character in COF-JLU51. Consequently, the photochemical activity of COF-JLU51 is higher than that of COF-JLU52. The H₂O₂ production rate of 4260.3 μmol g⁻¹ h⁻¹ and 3033.3 μmol g⁻¹ h⁻¹ was observed for COF-JLU51 and COF-JLU52, respectively. However, in a biphasic system containing water and benzyl alcohol in a ratio of 9:1, COF-JLU52 could produce H₂O₂ at a rate of 7624.7 μmol g⁻¹ h⁻¹ with AQY in 420nm of 18.2%. The SCC efficiency of COF-JLU51 and COF-JLU52 was reported to be 0.19% and 0.12%, respectively. Similarly, the influence of thiophene and

high nitrogen content in COF towards enhanced photocatalytic activity has been reported by Zeng and co-authors by demonstrating the N-site engineering strategy on thiophene-containing COF.¹¹⁷ Through the Schiff base condensation of various N-heterocycles (pyridine, pyrimidine, and triazine) units with a thiophene building unit, five COFs were synthesised. Among them, TTA-BT-COF and TTA-TF-COF were multicomponent COFs as both triphenyltriazine aldehyde and triphenyl triazine-NH₂ reacted with the thiophene moiety. The multicomponent TTA-TF-COF, which has more N-sites, was efficient towards photocatalytic H₂O₂ production with a maximum rate of 3343 μmol g⁻¹ h⁻¹ in pure water and air. These results suggest a direct correlation between the nitrogen atom density in the COF and photocatalytic H₂O₂ production. However, recent studies indicate that not only the nitrogen density but also its spatial positioning within the framework plays a crucial role in governing the efficiency of H₂O₂ formation. The effect of adjacent-N in the COF skeleton towards photocatalytic H₂O₂ production has been demonstrated by Zhao and co-authors.¹¹⁸ Three COFs, namely, BD-COF, Bpy-COF and Pylm-COF, were synthesised via Schiff base condensation reaction by reacting pyrene-NH₂ with various aldehydes that contain either 1,1' byphenyl (BD) or 2,2' bypyridine (Bpy) or 3,3' bypyridine (Pylm). The photocatalytic H₂O₂ production was evaluated using pure water under Xe light irradiation without any sacrificial agent. The H₂O₂ production with Pylm-COF was found to be 5850 μmol g⁻¹ h⁻¹, which is the highest amongst Bpy-COFs (3060 μmol g⁻¹ h⁻¹) and BD-COFs (670 μmol g⁻¹ h⁻¹). The AQY and SCC of Pylm-COF were 3.70% at 420 nm and 0.28% under AM 1.5G simulated sunlight. The theoretical investigation shows the pyrimidine unit responsible for the enhanced separation of the photogenerated electron-hole pair, which prevents the recombination and strong adsorption of O₂ on the adjacent N-atoms. It is well known that H₂O₂ formation proceeds through a 2e- ORR pathway; the electrophilicity of the COF and the nature of its oxygen-adsorption sites are crucial determinants of its photocatalytic efficiency. Rationally introducing electrophilic function groups such as fluorine, vinylene, and cyanide has also been shown to improve the photocatalytic H₂O₂ generation performance. For instance, Zhao *et al.*¹¹⁹ have synthesised pyridyl-imine functionalized D-A COFs (Pylm-B and Pylm-BT_X, X=H, F or 2F), by regulating the electronegative fluorine atoms (**Figure 7a**). The different F-atoms within the framework regulated the electron-deficient nature of the acceptor moiety. The electrochemical impedance spectra (**Figure 7b**) show the lowest electrochemical impedance and smallest charge-transfer resistance for Pylm-BT_F, followed by Pylm-BT_2F, Pylm-BT_H, and Pylm-B. These results demonstrate that tuning the D-A configuration effectively modulates photoinduced charge separation and transport in Pylm-COFs, with Pylm-BT_F showing superior optical and electrochemical performance due to its monofluorinated benzothiadiazole unit. Consequently, Pylm-BT_F achieved the highest H₂O₂ production rate of 5342 μmol g⁻¹ h⁻¹, surpassing both Pylm-BT_H (3577 μmol g⁻¹ h⁻¹) and Pylm-BT_2F (4061 μmol g⁻¹ h⁻¹) (**Figure 7c**). The COF exhibited good structural integrity and sustained photoefficiency during stability tests conducted for up to 10 h. The photoexcited carrier dynamics were evaluated through femtosecond



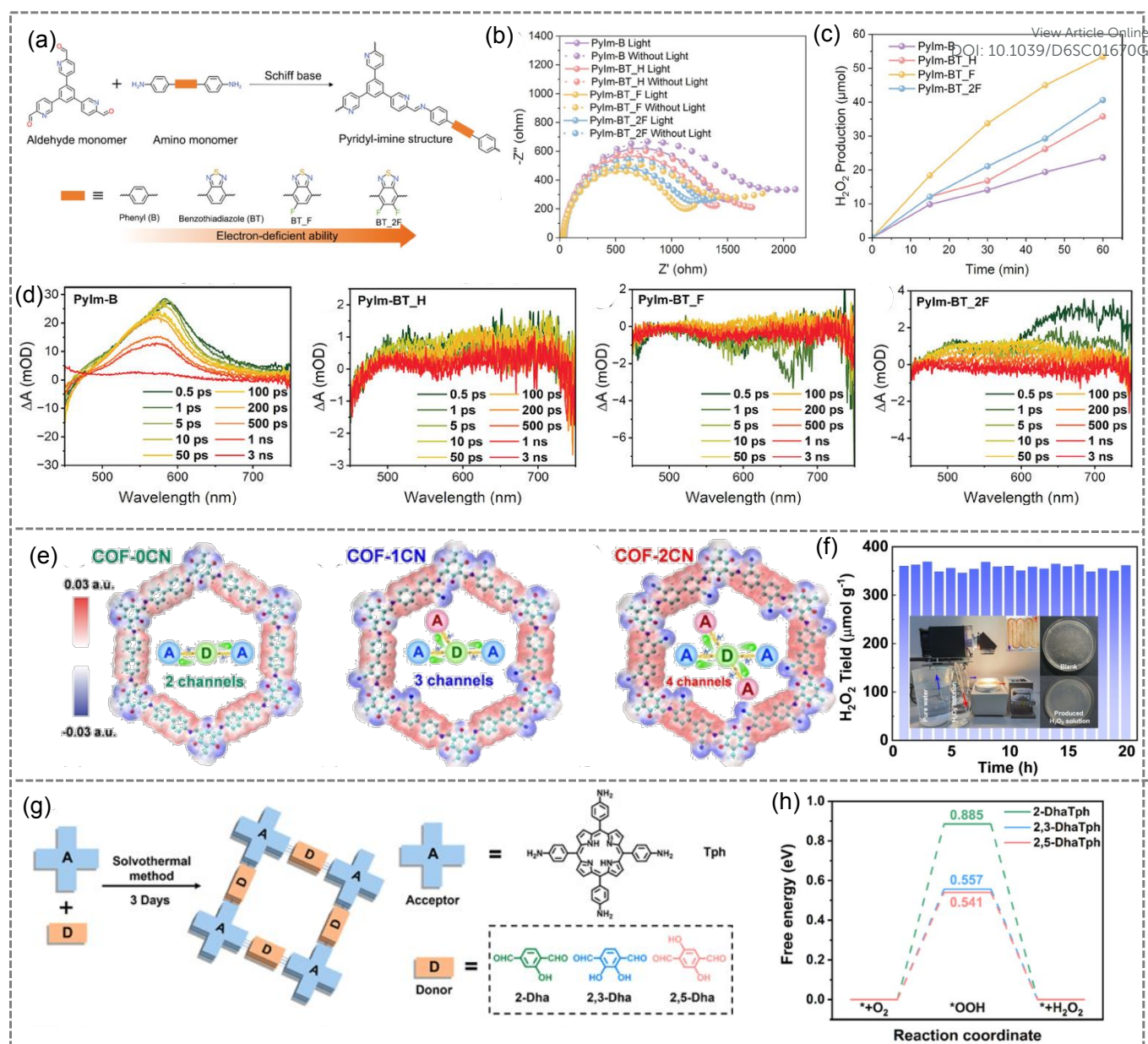


Figure 7: (a) Synthetic pathway of pyridyl-imine COF and the structure of synthesised COFs with regulated F-atoms. (b) Nyquist plots of PyIm-COFs (c) Time-dependent photocatalytic H₂O₂ production with pyridyl-imine COF. (d) Fs-TSA plots of PyIm-COFs. (Reproduced and reprinted with permission from the Ref¹¹⁹ Copyright 2025, Wiley-VCH GmbH). (e) Structure of Cyanide decorated COFs highlighting its D-A moieties. (f) Long-term photocatalytic H₂O₂ production using COF-2CN via flow catalysis, and the inset shows the reaction setup for flow catalysis. (Reproduced and reprinted with permission from the Ref¹²⁰ Copyright 2023, Wiley-VCH GmbH). (g) Schematic illustration of the synthesis of three hydroxyl-functionalized D-A COFs. (h) The Gibbs free energy spectra of the 2e⁻ ORR process on hydroxyl-functionalized D-A COFs. Reproduced and reprinted with permission from the Ref¹²¹ Copyright 2025, American Chemical Society.

transient absorption spectroscopy (fs-TAS), where all PyIm-COFs displayed ultrafast excited-state absorption (ESA) signals after photoexcitation (Figure 7d). PyIm-B exhibited a strong ESA band at 580 nm, indicating a high excited-state population. In contrast, BT-functionalized COFs (PyIm-BT_H, PyIm-BT_F, and PyIm-BT_2F) showed negative peaks at 740 nm, attributed to photoinduced emission from interfacial charge transfer between Py and BT units. These results confirm that the D-A architecture enhances charge transfer and suppresses electron-hole recombination. Although PyIm-BT_2F contains more fluorine atoms, the superior activity of PyIm-BT_F suggests that an optimal, rather than excessive, electrophilic character is essential for efficient H₂O₂ generation.

Similarly, the regulation of cyanide moiety with the framework has been reported by Tong et al., where they have synthesised three-ketoenamine-based D-A COF by regulating the CN groups (COF-xCN, where x 0,1,2) (Figure 7e).¹²⁰ The H₂O₂ photosynthesis performance of synthesised COF in pure water and O₂ under visible light irradiation shows an increasing production with an increasing number of the CN functional group. Consequently, the highest production for COF-2CN (1601 mmol g⁻¹ h⁻¹) was observed, followed by COF-1CN (573 mmol g⁻¹ h⁻¹), and lastly COF-0CN (194 mmol g⁻¹ h⁻¹). The remarkable efficiency of COF-2CN can be attributed to the presence of two CN groups within the framework, which activate the adjacent carbon atom, facilitating the formation of the key *OH intermediate that



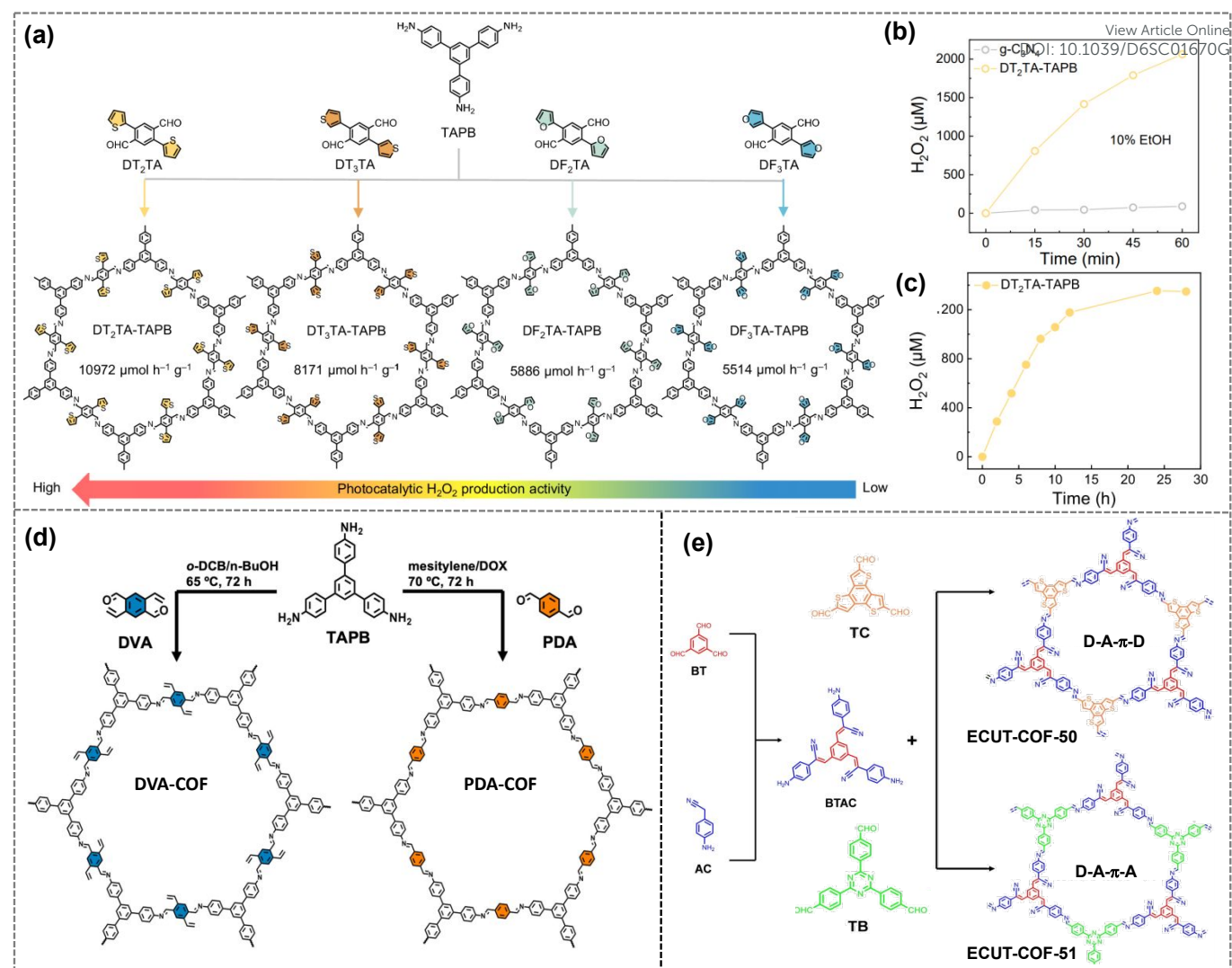


Figure 8: (a) Schematic route for the synthesis of thiophene and furan-decorated imine COFs. (b) Photocatalytic H₂O₂ production comparison of DT₂TA-TAPB and g-C₃N₄ photocatalyst. (c) Long-term photocatalytic H₂O₂ production plot with DT₂TA-TAPB. (Reproduced and reprinted with permission from the Ref¹²² Copyright 2025, Springer Nature). (d) Schematic route for the synthesis of vinylene decorated COF. (Reproduced and reprinted with permission from the Ref¹²³ Copyright 2024, Wiley-VCH GmbH). (e) Synthetic scheme for the synthesis of cyanide-functionalized D-A COF. (Reproduced and reprinted with permission from the Ref¹²⁴ Copyright 2024, Wiley-VCH GmbH).

lowers the energy barrier for the rate-determining two-electron water oxidation step in H₂O₂ photosynthesis. H₂O₂ was also produced efficiently and stably at a rate of ≈716 μmol g⁻¹ h⁻¹ under visible-light irradiation over a 20 h photocatalytic operation in a continuous-flow reactor (Figure 7f). The effect of regulating the number and position of hydroxyl (-OH) groups on photocatalytic H₂O₂ production has been investigated in porphyrin-based COFs by Liu *et al.* (Figure 7g).¹²¹ Three COFs, namely 2-DhaTph, 2,5-DhaTph, and 2,3-DhaTph, were synthesised, in which the porphyrin unit acts as the electron acceptor, while the hydroxyl-functionalized moiety serves as the electron donor. An increase in the number of -OH groups enhance the donor ability of the COFs, leading to improved photoefficiency. However, compared to 2,3-DhaTph with para-positioned hydroxyl groups, 2,5-DhaTph with para-positioned -OH groups exhibit higher crystallinity and better exposure of catalytically active sites. Consequently, 2,5-DhaTph showed a H₂O₂ production rate of 2103.1

μmol h⁻¹ g⁻¹, 1.1 times higher than 2,3-DhaTph. DFT analysis revealed that 2,5-DhaTph exhibits the lowest energy barrier (0.541 eV) for the formation of the *OOH intermediate, which is the rate-determining step, compared to the other COFs (Figure 7h). Similarly, incorporating thiophene and furan isomeric units into the side chains of COFs enables precise tuning of COF electronic structures, and photocatalytic activity was demonstrated by Tang *et al.*¹²² Four COFs, namely DT₂TA-TAPB, DT₃TA-TAPB, DF₂TA-TAPB, and DF₃TA-TAPB, were synthesised by reacting 1,3,5-tris(4-aminophenyl)benzene (TAPB) and terephthalaldehyde substituted with 2 or 3 thiophene or furan moieties (Figure 8a). Thiophene isomer-functionalized COFs exhibited superior performance relative to their furan isomer-based counterparts, which can be attributed to a more favourably matched D-A architecture. Consequently, DT₂TA-TAPB achieved the H₂O₂ production of 10972 and 8587 μmol g⁻¹ h⁻¹ in 10% ethanol and pure water, which is ~23 and ~41 times greater than the benchmark g-



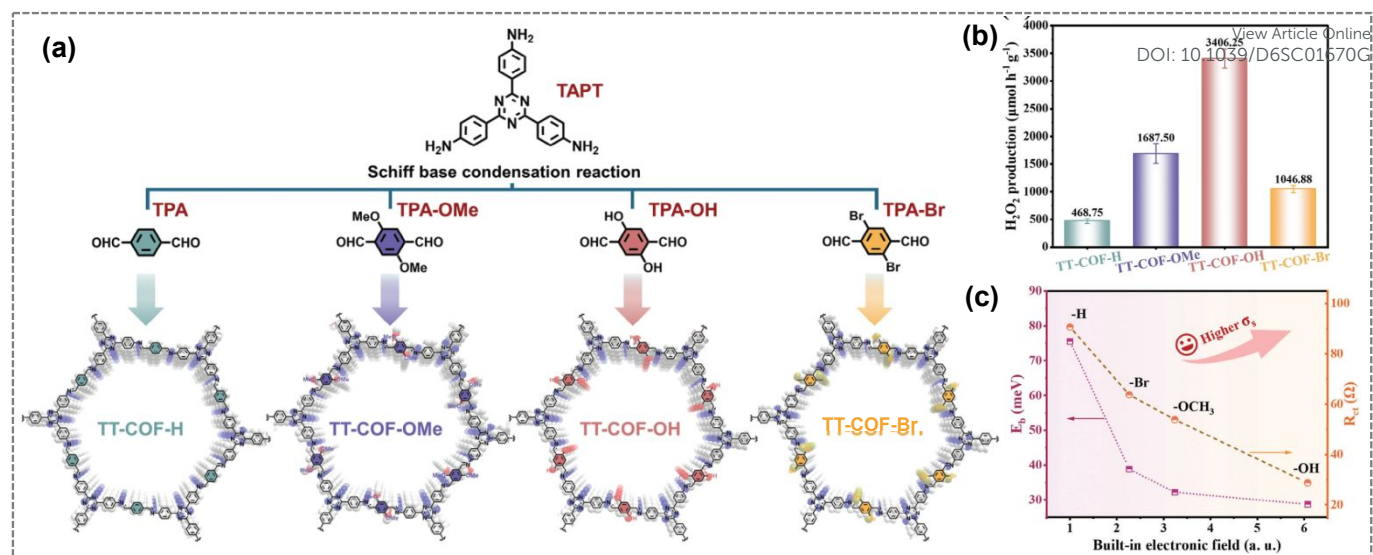


Figure 9: (a) Synthetic route for the synthesis of different functionalized imine COF. (b) Photocatalytic H₂O₂ production comparison of functionalized COFs. (c) built-in electric field (BIEF) plot of functionalized imine COF. (Reproduced and reprinted with permission from the Ref¹²⁵ Copyright 2025, Wiley-VCH GmbH)

C₃N₄ (Figure 8b). COF DT2TA-TAPB also showed stable photocatalytic H₂O₂ production for 24 h under simulated natural conditions, followed by a steady plateau up to 28 h, indicating a dynamic formation-decomposition equilibrium (Figure 8c).

The vital challenges in COFs, such as low charge-generation and -transfer efficiencies, as well as rapid charge recombination that severely hindered the H₂O₂ production, have also been addressed by anchoring the vinyl moieties within the COF skeleton. The recent work from Chen and group demonstrates the synthesis of two imine-based COFs, one decorated with a vinyl group (DVA-COF) and another without any functionalization (PDA-COF) (Figure 8d).¹²³ Owing to the excellent π - π conjugated structure, abundant electronics, non-polar nature, and other characteristics of the vinyl group, the role of intralayer electron delocalisation and interlayer π - π stacking on charge generation and separation has been rationally studied. The photocatalytic performance of the synthesised COF towards H₂O₂ production has been conducted in the two-phase water/benzyl alcohol (9:1, v/v) system. The vinyl containing DVA-COF could produce H₂O₂ photocatalytically at the rate of 84.5 $\mu\text{mol h}^{-1}$ per 10 mg photocatalyst, which is higher than that of non-functionalised PDA-COF (8.6 $\mu\text{mol h}^{-1}$ per 10 mg photocatalyst). The AQY and SCC efficiency values for DVA-COF were calculated to 2.84% at 420 nm and \sim 0.08% under AM 1.5G simulated sunlight. On investigation of the catalytic pathway, the vinyl group present in COF was found to inhibit photogenerated electron-hole recombination. DVA-COF shows excellent cycling stability over five irradiation cycles, with no noticeable changes in PXRD patterns. Continuous H₂O₂ production was maintained under light irradiation for 16 h, accompanied by nearly equimolar formation of H₂O₂ and benzaldehyde. The photo efficiency of COF could also be rationally enhanced by functionalizing with various D-A moieties. For instance, Luo et al.¹²⁴ have synthesised COF by integration of π -accepting cyanide functional group that acts as a π electron acceptor. Its combination with donor thiophene and acceptor triazine monomers yielded D-A- π -D (ECUT-COF-50) and D-

A- π -A (ECUT-COF-51) frameworks, respectively (Figure 8e). Interestingly, D-A- π -D COF demonstrated significantly higher efficiency than the D-A- π -A counterpart, achieving a remarkable H₂O₂ production rate of 4742 $\mu\text{mol h}^{-1} \text{g}^{-1}$ using only air and water. Furthermore, ECUT-COF-50 maintained consistent H₂O₂ production over 80 h of continuous operation without performance loss. Similarly, as hydroxyl moieties are known to enhance the hydrophilicity of COF, Shen *et al.* demonstrated that synergistic functional group modification, which tunes electronic conjugation and intramolecular polarity, significantly enhances light absorption, charge separation/transfer, and interfacial water-oxygen affinity.¹²⁵ This was achieved by synthesising a series of imine-linked COFs (TT-COF-X) with electronically tunable substituents (X = -H, -OMe, -OH, -Br) (Figure 9a). Photocatalytic H₂O₂ production proceeds via a dual-channel pathway involving 2e- ORR and WOR pathways, highlighting 100% atomic utilisation. Among the series, hydroxyl-functionalized TT-COF-OH delivered the highest H₂O₂ production rate (3406.25 $\mu\text{mol g}^{-1} \text{h}^{-1}$) (Figure 9b) and an impressive AQY of 8.1%. It also exhibits efficient performance over a wide pH range and in real water matrices. fs-TA spectroscopy (460-800 nm) was used to probe ultrafast exciton dissociation dynamics. The results show that a polarity-induced built-in electric field (BIEF) in TT-COF-OH enables a BIEF-mediated shallow trap state, facilitating exciton dissociation and suppressing electron-hole recombination, leading to a much longer average lifetime ($\tau_{\text{avg}} = 475.76$ ps) compared to TT-COF-H ($\tau_{\text{avg}} = 76.32$ ps). These results further reveal that exciton binding energy (E_b) and charge-transfer resistance (R_{ct}) decrease with increasing BIEF intensity (Figure 9c). A stronger BIEF introduces a trap state that promotes exciton dissociation and charge transport, thereby enhancing exciton dissociation efficiency (σ_d). Mechanistic studies reveal that hydroxyl-induced electronic microenvironment regulation enhances conjugation for improved light harvesting, generates a 6.01-fold stronger BIEF to accelerate exciton dissociation and charge transport, and promotes oxygen/water adsorption with



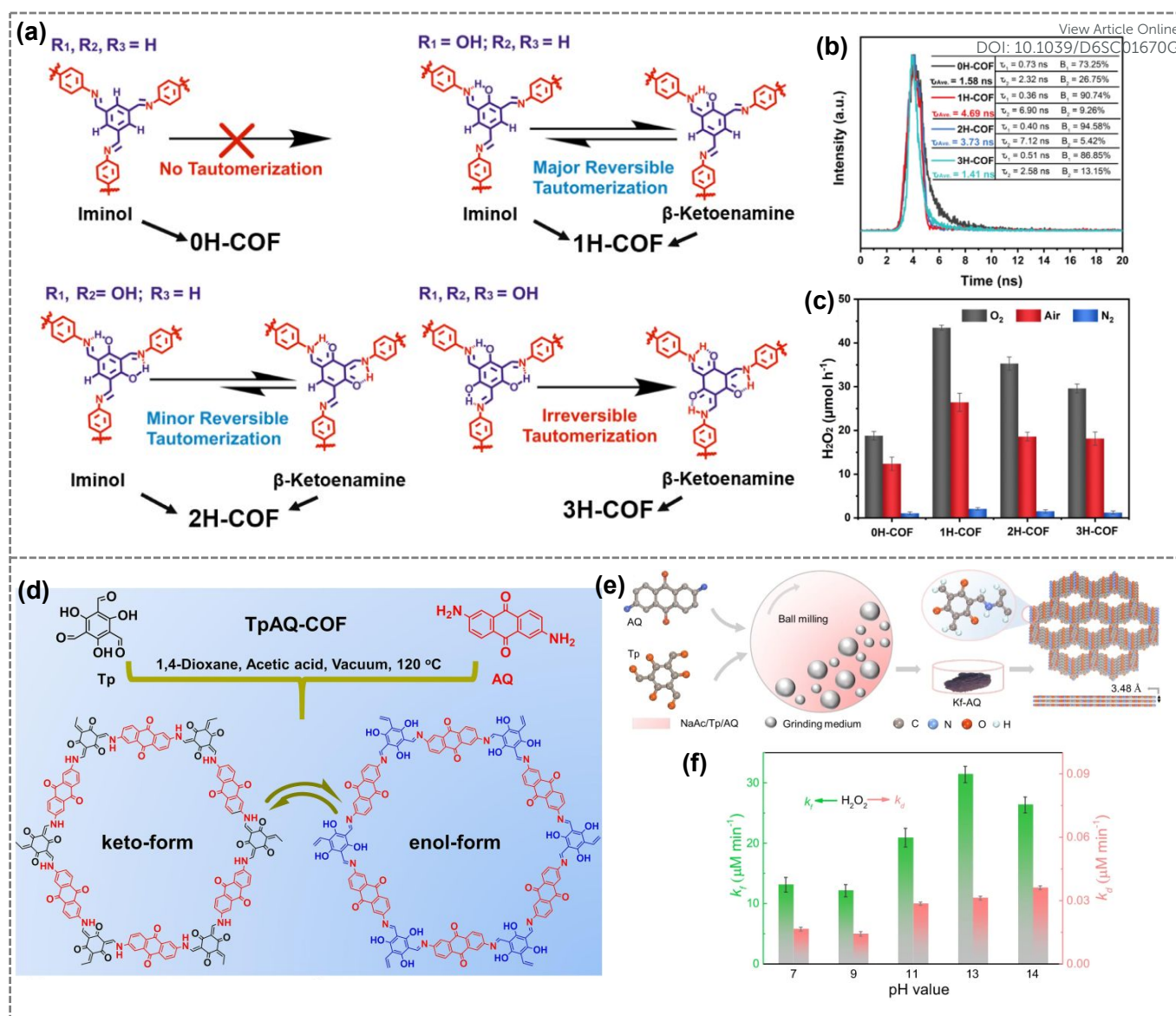


Figure 10: (a) Illustration of iminol-to-ketoenamine tautomerism in XH-COFs via proton transfer. (b) TRPL spectra of ketoamine COFs. (c) Photocatalytic H_2O_2 production comparison of ketoamine COFs. (Reproduced and reprinted with permission from the Ref.¹²⁶ Copyright 2023 Elsevier). (d) Structure of TpAQ-COF in its keto and enol form. (Reproduced and reprinted with permission from the Ref.¹²⁷ Copyright 2023 Elsevier). (e) Mechanochemical synthetic route for Kf-AQ COF. (f) H_2O_2 formation and decomposition plot using Kf-AQ COF in different pH solutions. (Reproduced and reprinted with permission from the Ref.¹²⁸ Copyright 2024 Springer Nature)

faster interfacial electron transfer. Schiff base condensation reaction between amines and aldehydes remains one of the most widely utilised techniques for synthesising COFs. However, a significant challenge encountered by researchers is the frequent hydrolysis of amine bonds formed through a condensation reaction, which leads to structural collapse. Notably, Bannerjee and co-workers addressed this COF challenge, and the stability of Schiff base-condensed COFs has been markedly enhanced by using triformylphloroglucinol (Tp) as an aldehyde linker.¹²⁹ The hydroxyl group adjacent to the formyl group in Tp facilitates irreversible keto-enol tautomerism, thereby inhibiting the hydrolysis of the amine bond. Although the availability of three hydroxyl groups in Tp provides stability to COF, its irreversible tautomerism decreases the crystallinity of COF and can

hinder photocatalytic activity. To this, the decrease of the hydroxyl group in Tp aldehyde has allowed for the partly reversible keto-enol tautomerism that enhances both the stability and crystallinity of COF.^{130,131} The presence of different hydroxyl groups towards its photocatalytic activity has been recently explored by Kong et al. as they report the synthesis of four imine-based COF (0H, 1H, 2H, and 3H-COF, **Figure 10a**) with different numbers of hydroxyl functionalized (0-3).¹²⁶ The degree of keto-enol tautomerism in imine-linked COFs can be controlled by varying the number of -OH groups attached to the aldehyde precursors. This adjustment significantly influences the crystallinity and photocatalytic properties of the COFs. The structure-activity relationship between the reversibility of bonding in supramolecular chemistry was thoroughly



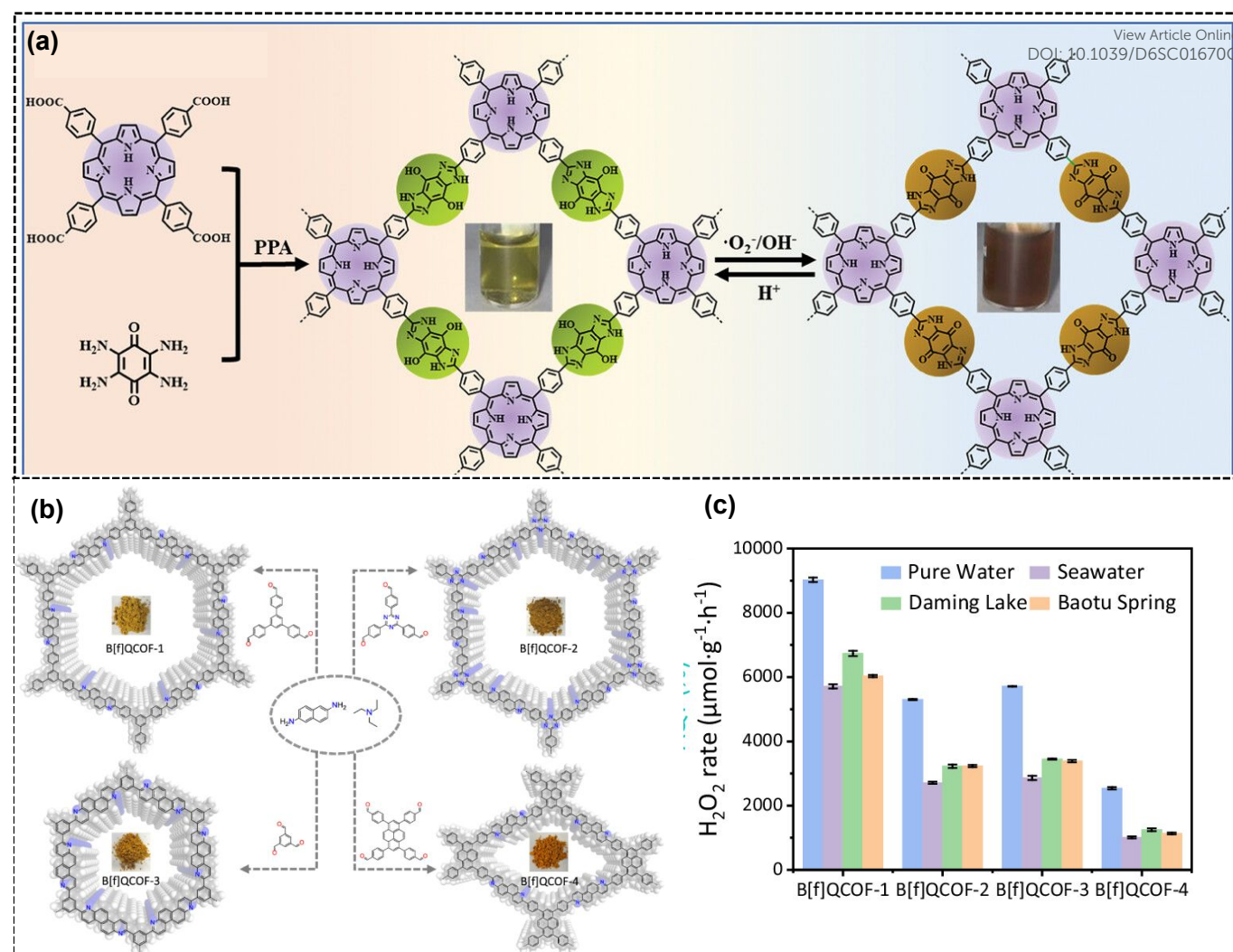


Figure 11: (a) Synthetic route for Por-HQ-COF and Por-BQ-COF. (Reproduced and reprinted with permission from the Ref.¹³² (Copyright 2024 Wiley-VCH GmbH). (d) Synthesis scheme and structure of benzo[f]quinoline-linked COFs. (e) Photocatalytic H_2O_2 production with benzo[f]quinoline-linked COFs using different water samples. (Reproduced and reprinted with permission from the ref.¹³³ Copyright 2024 Springer Nature).

studied towards photocatalytic H_2O_2 activity. Among the four COFs studied, 1H-COF, which contains a single -OH group, exhibits the most ordered structure and the highest conjugation due to the predominant tautomerization. Additionally, the rearrangement between enol-imine and keto-amine linkages optimises its optical absorbance, electron push-pull effect, and water stability. This dynamic charge redistribution suppresses electron-hole recombination, resulting in a longer excited-electron lifetime for 1H-COF, as confirmed by time-resolved photoluminescence (TRPL) measurements (Figure 10b). As a result, 1H-COF can produce H_2O_2 with a rate of $44.5 \mu\text{mol h}^{-1}$ in the presence of a 10% IPA solution (Figure 10c). The effect of keto-enol tautomerism on the photocatalytic efficiency of imine-based COF has also been studied by Long and Co-workers.¹²⁷ Intrigued by the anthraquinone moieties towards mass production of H_2O_2 , they have synthesised imine-based COF (TpAQ-COF) by Schiff base condensation reaction between 2,6-diaminoanthraquinone (AQ) and

triformylphloroglucinol (Tp) (Figure 10d). The anthraquinone moieties serve as the active sites for selective two-electron ORR, promoting the separation and migration of photogenerated charges. Interestingly, the keto-amine form of the COF was found to be more efficient for H_2O_2 production than the enol-imine form, and by adjusting the condensation time, researchers could vary the ratio of the two forms, with the keto-amine form promoting better D-A coupling structures that favour the migration of photogenerated carriers. Consequently, TpAQ-COF could produce H_2O_2 at the rate of $420 \mu\text{mol g}^{-1} \text{h}^{-1}$ with an AQY of 7.2% at 420 nm. The COF also showed good stability of 12 h upon prolonged irradiation for 12 h, with steady production of H_2O_2 . Motivated by the result, the same group has extended the research through synthesising keto-form anthraquinone COF (K_f COF) via a mechanochemical route (Figure 10e).¹²⁸ K_f -COF could form H_2O_2 under alkaline medium ($\text{pH}=13$) at a rate of $4784 \mu\text{mol g}^{-1} \text{h}^{-1}$. At $\text{pH} 13$, K_f -AQ exhibited the highest H_2O_2 formation rate constant ($k_f = 31.39 \mu\text{M min}^{-1}$), while maintaining a

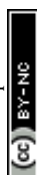


Table 2: Summary of the representative functionalization of COFs photocatalysts in H₂O₂ photosynthesisView Article Online
DOI: 10.1039/D6SC01670G

Sl. No	Catalyst	Reaction condition	Dosage (mg) & volume (mL)	H ₂ O ₂ Yield (μmol g ⁻¹ h ⁻¹)	AQY	SCC	Ref
1.	HEP-TAPT-COF	H ₂ O and O ₂	50mg & 100 mL	87.50 μmol h ⁻¹	-	0.65%	115
2.	COF-JLU51	H ₂ O and O ₂	5 mg & 50 mL	3388.3	6.4%	0.19%	116
3.	TTA-TF-COF	H ₂ O	1 mg & 8 mL	3343	4.1% @ 420 nm	0.13%	117
4.	PyIm-COF	H ₂ O	10 mg & 50 mL	5850	3.70% @420 nm	0.28%	118
5.	PyIm-BT_F	H ₂ O: IPA=9:1	10 mg & 50 mL	5342	2.7% @420 nm	-	119
6.	COF-2CN	H ₂ O and O ₂	12.5 mg & 50 mL	1601	6.8% @459 nm	0.6%	120
7.	2,5-DhaTph	H ₂ O: EtOH=9:1	10 mg & 50 mL	2103.1	0.15% @450 nm	-	121
8.	DT ₂ TA-TAPB	H ₂ O and O ₂	5 mg & 25 mL	8587	3.3% @380 nm	-	122
9.	DVA-COF	H ₂ O:BA=9:1, O ₂	10 mg & 20 mL	8450 ^b	2.84 @420 nm	0.08%	123
10.	ECUT-COF-50	H ₂ O	5 mg & 50 mL	5382	11.2% @400 nm	0.68%	124
11.	TT-COF-OH	H ₂ O	5 mg & 50 mL	3406	8.1% @400 nm	0.58	125
12.	1H-COF	H ₂ O: IPA (9:1), O ₂	30 mg & 30 mL	44.5	5.4% @ 420 nm	-	126
13.	TpAQ-COF	H ₂ O and O ₂	10 mg & 30 mL	420	7.4% @ 420 nm	-	127
14.	Kf-AQ	H ₂ O (pH=13), O ₂	5 mg & 30 mL	4784	15.8% @ 400 nm	0.87%	128
15.	POR-BQ-COF	H ₂ O (pH=13), O ₂	10 mg & 30 mL	1525	5.05% @420 nm	-	132
16.	B[f]QCOF-1	H ₂ O	10 mg & 50 mL	9025	8.9% @450 nm	0.23%	133

Light Irradiation: λ>420 nm, ^aSunlight, ^bLED light, BA: Benzyl alcohol, IPA: Isopropanol

moderate decomposition rate constant ($k_d = 0.031 \mu\text{M min}^{-1}$) (Figure 10f). The highly alkaline environment promoted the formation of OH⁻(H₂O)₂ clusters, which were adsorbed onto the keto moieties of the framework. This adsorption significantly lowered the energy barrier for hydrogen abstraction, facilitating their dissociation into O₂ and active hydrogen species. The generated hydrogen subsequently reduced anthraquinone to anthrahydroquinone, which was then re-oxidised by O₂ to yield H₂O₂. The integration of the quinone unit in COF has also demonstrated H₂O₂ production in the full pH range (pH 1-13), as demonstrated by Li et al.¹³² Two COFs, Por-HQ-COF and Por-BQ-COF, have been synthesised with p-hydroquinone (HQ) and p-benzoquinone (BQ) moieties. Interestingly, under alkaline conditions, Por-HQ-COF undergoes conversion to Por-BQ-COF (Figure 11a). In this transformed structure, the imidazole nitrogen in Por-BQ-COF facilitates water molecule dissociation to generate protons and enhances the ORR, resulting in a notable H₂O₂ production rate of up to 1525 μmol g⁻¹h⁻¹. Further, Por-BQ-COF showed the k_f of 13.55 μM min⁻¹ and the lowest k_d of 0.0165 μM min⁻¹ at pH 13. The efficiency of quinoline-linked COFs has also been widely explored by Dong et al. Benzo[f]quinoline-linked COFs have been synthesised through a one-pot, three-component [4+2] cyclic condensation strategy.¹³³ This approach involves the reaction of aldehydes and aromatic amines using triethylamine as a readily

accessible vinyl source, resulting in the formation of stable and highly photoactive benzo[f]quinoline-linked COFs (Figure 11b). The high crystallinity, improved stability, and strong light-harvesting ability of these COFs contributed to their excellent performance in H₂O₂ photosynthesis. As a result, B[f]QCOF-1 exhibited exceptional photocatalytic activity, reaching an H₂O₂ production rate of 9025 μmol g⁻¹ h⁻¹ in pure water (Figure 10e) without any sacrificial agent, accompanied by nearly equimolar formation of H₂O₂ and benzaldehyde.

Tuning of Linkage in COF for photocatalytic H₂O₂ production:

Linkage engineering has emerged as a powerful strategy to enhance the photocatalytic performance of COFs for H₂O₂ production. The chemical nature of the linkages, such as imine, β-ketoenamine, hydrazone, azine, or imidazole, directly influences the COF's electronic structure, charge separation efficiency, and interaction with oxygen molecules. By precisely tuning the linkage, researchers can modulate bandgap, charge transfer pathways, redox potentials, and surface adsorption sites, all of which are critical for the two-electron ORR producing H₂O₂. Electron-rich linkages improve light absorption and facilitate exciton dissociation, whereas electron-deficient linkages enhance O₂ adsorption and promote selective 2e⁻ reduction over the competing 4e⁻ pathway. Additionally, robust



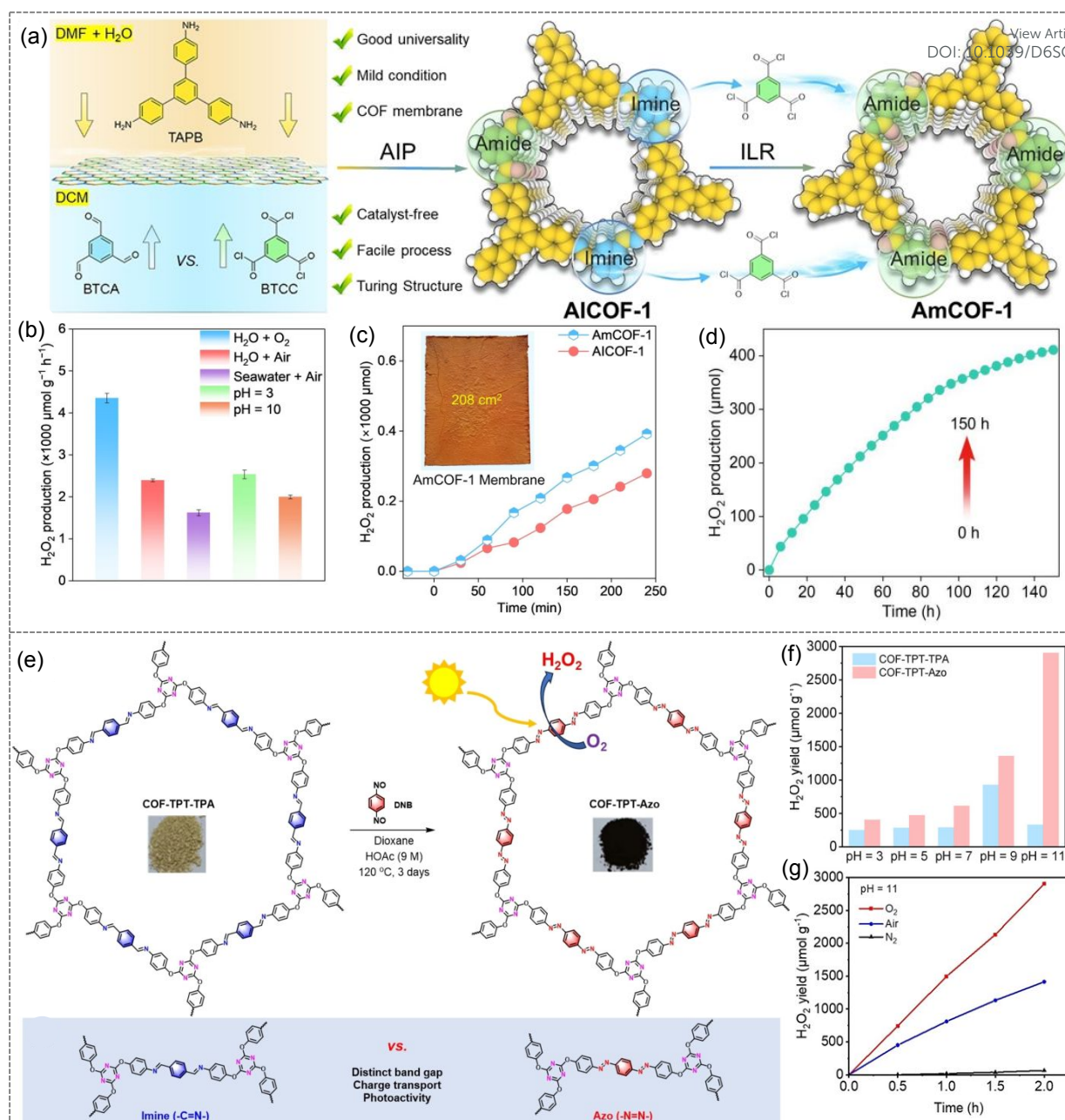


Figure 12: (a) Synthetic illustration of AmCOF-1 from AICOF-1. (b) Photocatalytic H_2O_2 production of AmCOF-1 in different conditions. (c) Time course of H_2O_2 production using the membrane of AICOF-1 and AmCOF-1 under natural light (inset: AmCOF-1 membrane). (d) long term production H_2O_2 over 150 h with AmCOF-1. (Reproduced and reprinted with permission from the Ref.¹³⁴ Copyright 2025 Wiley-VCH GmbH). (e) Synthesis scheme and structure of imine and azo-linked COFs. (f) Photocatalytic H_2O_2 production comparison under pH conditions. (g) Continuous H_2O_2 production with COF-TPT-Azo over 2h under different conditions at pH-11. (Reproduced and reprinted with permission from the Ref.¹³⁵ Copyright 2024 Wiley-VCH GmbH)

linkages can also improve chemical stability, allowing sustained catalytic activity under aqueous and oxidative conditions. To elucidate how linkage positioning governs the photocatalytic performance and stability of COFs toward H_2O_2 production, Yang et al. systematically investigated the influence of ortho and para linkages in COFs. Six COFs were synthesised from ortho/para-substituted diamines (Bda, Pda, Pzda) and Tp.¹³⁶ Pyridinic nitrogen favoured the $2e^-$ ORR, while β -ketoenamine carbons acted as $4e^-$ WOR active sites, making Pzda-based COFs the most efficient. Although p-COF-TpBda showed a high initial H_2O_2 rate ($6434 \mu\text{mol g}^{-1} \text{h}^{-1}$), it rapidly degraded, whereas o-COF-TpPzda maintained stable

H_2O_2 production ($4396 \mu\text{mol g}^{-1} \text{h}^{-1}$) for 48 h. DFT revealed a lower ΔG for the rate-determining WOR step in o-COF-TpPzda, enabling faster hole consumption and enhanced stability, while largely preserving $2e^-$ ORR activity. Linkage chemistry also plays a key role in achieving crystalline, robust COFs while enabling functionalities such as band-gap modulation and redox activity. Mou et al. reported azole-linked COFs synthesised from pyrene aldehyde and heteroatom-substituted phenylenediamines, yielding thiazole (TZ-COF), oxazole (OZ-COF), and imidazole (IZ-COF) frameworks.¹³⁷ These azole linkages introduce electron-donating conjugation within a D- π -A architecture, enhancing visible-light absorption and charge



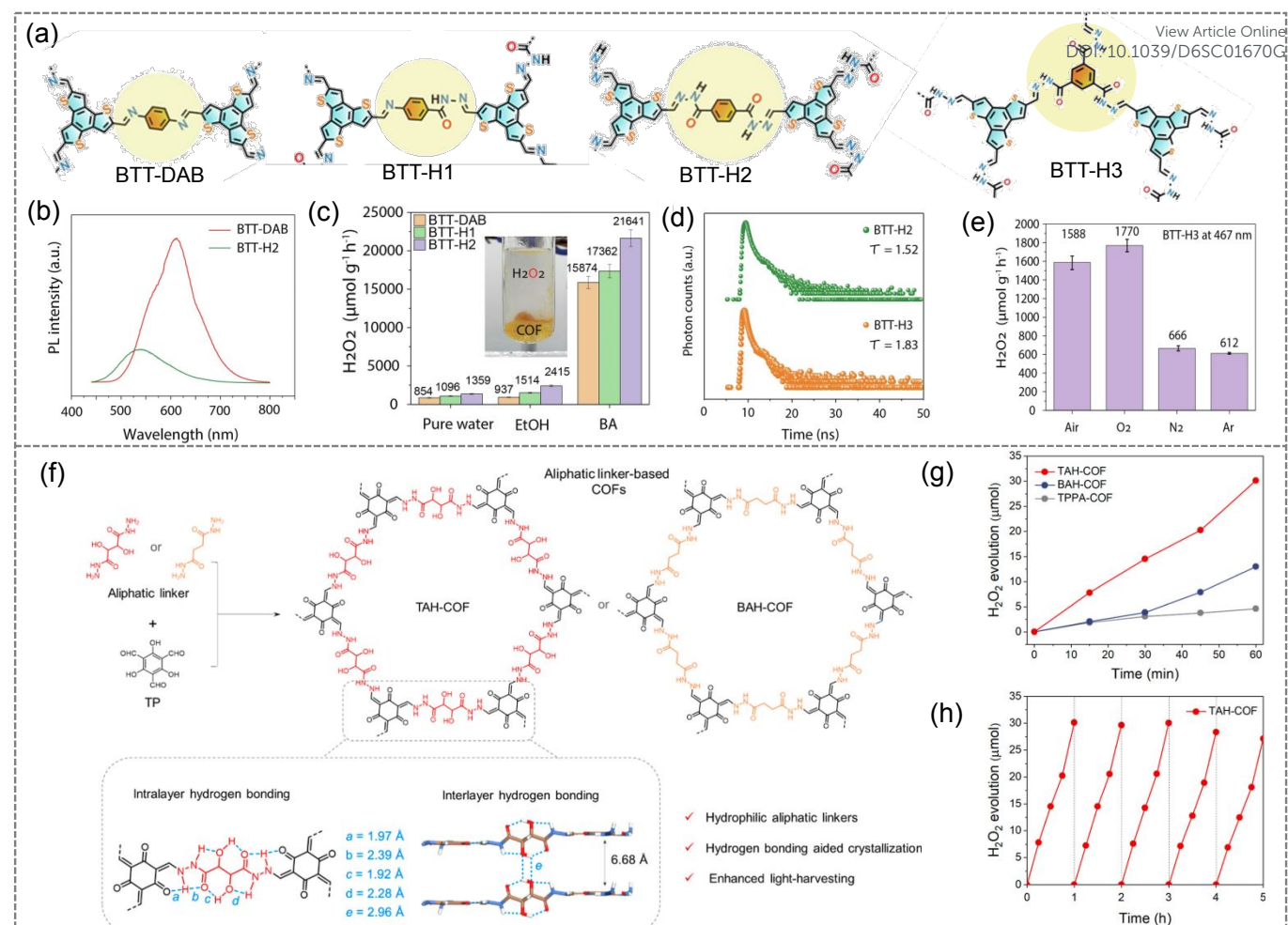


Figure 13: (a) Structure of benzotrithiophene-based COF with regulation of hydrazone linkage. (b) PL-spectra of benzotrithiophene-based COF with and without hydrazone linkage. (c) Photocatalytic H_2O_2 production comparison of benzotrithiophene-based COF in different sacrificial electron agents. (d) TRPL data of BTT-H2 and BTT-H3 COFs and (e) Photocatalytic H_2O_2 production with BTT-H3 in different environments. (Reproduced and reprinted with permission from the Ref.¹³⁸ Copyright 2025, Springer Nature). (f) Synthesis scheme and structure of COF with aliphatic linker. (g) Photocatalytic H_2O_2 production with aliphatic linker-based COFs. (h) Long-term photocatalytic H_2O_2 production with TAH-COF. (Reproduced and reprinted with permission from the Ref.¹³⁹ Copyright 2025, American Chemical Society)

transport. Femtosecond transient absorption revealed the longest excited-state lifetime for TZ-COF (5.94 ps), followed by OZ-COF (3.74ps) and IZ-COF (1.86 ps), indicating more efficient charge separation with thiazole linkages. Accordingly, the O_2 production activity follows the order: TZ-COF > OZ-COF > IZ-COF. A distinct difference in efficiency and stability between reversible imine-linked COFs (AICOF-1) and irreversible amide-linked COFs (AmCOF-1) has been demonstrated by Li et al for photocatalytic H_2O_2 production.¹³⁴ They have synthesised the self-standing membrane of crystalline COF for photocatalytic H_2O_2 production. In brief, AICOF-1 was synthesised using an ingenious autocatalytic interfacial polymerisation (AIP) strategy. Subsequently, AICOF-1 was converted into a fully amide-linked crystalline membrane (AmCOF-1) via a traditional irreversible linker renovation (ILR) reaction with acyl chlorides, yielding COFs with well-defined Turing structures (Figure 12a). This approach offers several advantages, including broad applicability, a simple and catalyst-free synthesis at ambient temperature, and the ability to produce large, free-standing membranes with diverse Turing patterns. Given the robust nature with an efficient electron-

withdrawing nature, and potential π -electron segregation effect of the amide units, the authors have demonstrated the photocatalytic efficiency of AmCOF-1 membrane towards H_2O_2 production. AmCOF-1 shows the production in varied water conditions, including pure water, seawater, and solutions with high pH and low pH (Figure 12b). A photocatalytic H_2O_2 production reached up to $4353 \mu\text{mol g}^{-1} \text{h}^{-1}$ in O_2 -saturated H_2O . Further, a large-area ($16 \text{ cm} \times 13 \text{ cm}$), self-standing AmCOF-1 membrane showed stable H_2O_2 production for 4 h under natural sunlight (Figure 12c). The AmCOF-1 membrane also shows remarkable stability over 150 h under sunlight without sacrificial agents (Figure 12d), which was further verified from PXRD of recovered samples. In a similar direction, Zhao and co-workers compared the photocatalytic performance of azo-linked and imine-linked COFs for H_2O_2 production.¹³⁵ They rationally synthesised two COFs, an imine-linked COF (COF-TPT-TPA) and an azo-linked COF (COF-TPT-Azo) via Schiff-base polycondensation (Figure 12e). Remarkably, despite differing by only a single atom ($-\text{N}=\text{N}$ -vs- $\text{C}=\text{N}$) COF-TPT-Azo shows a much narrower band gap, improved charge transport, and enhanced photoactivity compared to its imine



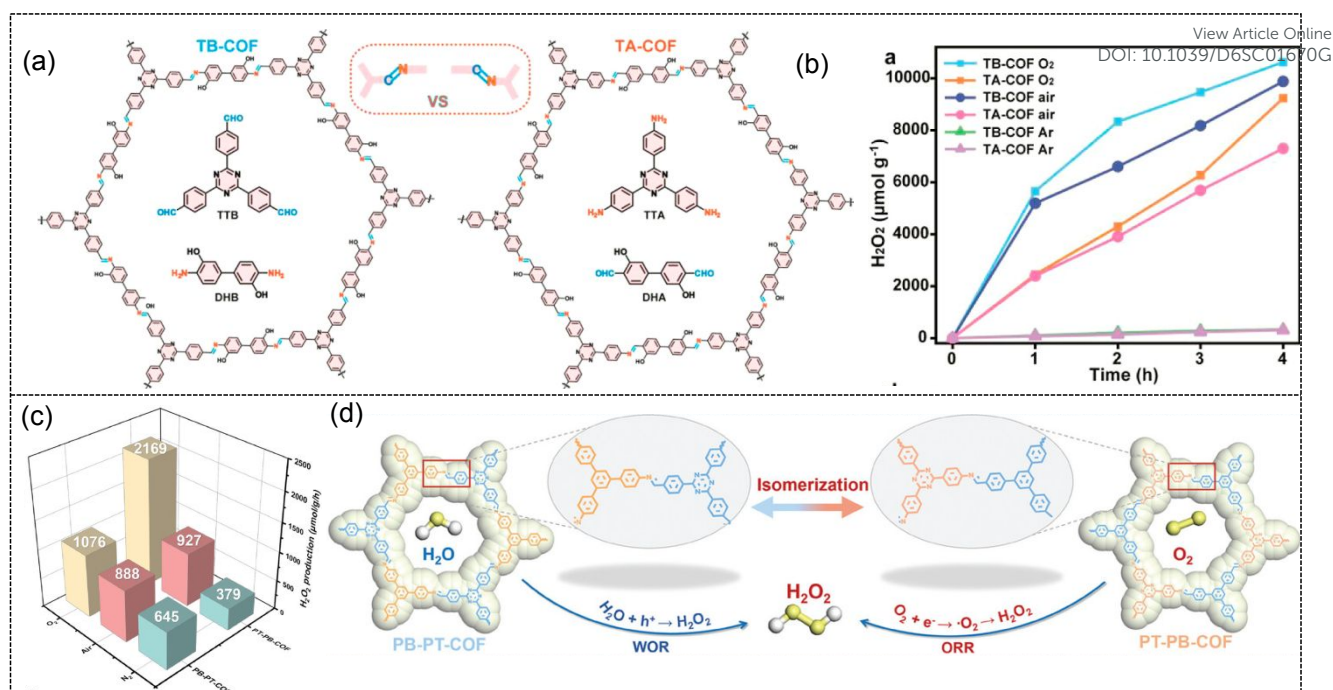


Figure 14: (a) Synthetic illustration of isomeric TA-COF and TB-COF. (b) Time-dependent H₂O₂ synthesis with isomeric COFs in different atmospheres. (Reproduced and reprinted with permission from the Ref.¹⁴⁰ Copyright 2025, American Chemical Society). (c) Photocatalytic H₂O₂ production comparison with PB-PT-COF and PT-PB COF. (d) Structures of isomeric PB-PT-COF and PT-PB COF highlighting their pathways for the production of H₂O₂. (Reproduced and reprinted with permission from the Ref.¹⁴¹ Copyright 2024 Wiley-VCH GmbH)

counterpart. Consequently, COF-TPT-Azo was found to produce H₂O₂ at a rate of 1498 μmol g⁻¹ h⁻¹ in O₂-saturated alkaline solution of pH=11 under visible light irradiation (λ > 420 nm), which is 7.9 times higher than that of imine-based COF-TPT-TPA (Figure 12f). COF-TPTAzo remarkable H₂O₂ production at alkaline solution both under O₂ and Air (Figure 12g). DFT studies show that HOMO is distributed at the N=N group, while LUMO is on the same azobenzene units. Therefore, the N=N groups in the COF-TPT-Azo and C=N groups in COF-TPT-TPA play an important role in light absorption and promote the photocatalytic oxidation.

The effect of hydrazone linkages and their density has recently been studied by Pachfule et. al.¹³⁸ They synthesised a series of D-A thiophene-based COF (BTT-DAB, BTT-H1 and BTT-H2), and regulated the hydrazone density (0-2) (Figure 13a). This gradual variation enabled a direct comparison of how hydrazone density affects photocatalytic behaviour. The introduction of hydrazone linkages has decreased e-h recombination as indicated by the decreased PL (Figure 13b). The production of H₂O₂ was observed to vary directly proportional to the number of hydrazone linkages. As a result, BTT-DAB, BTT-H1, and BTT-H2 produce H₂O₂ at a rate of 854, 1096, and 1359 μmol g⁻¹ h⁻¹ from water and air under irradiation of 467 nm light. BTT-H2 also delivered a dramatically higher output of 21,641 μmol g⁻¹ h⁻¹ in the presence of benzyl alcohol as a sacrificial agent (Figure 13c). Motivated by the results, the authors also synthesised BTT-H3 COF with three hydrazone linkages (Figure 13a). An increase in hydrazone density increases the lifetime of the photogenerated electron, as indicated from the TRPL plot (Figure 13d). BTT-H3 delivered H₂O₂ production of 1588 μmol g⁻¹ h⁻¹ from water and air (Figure 13e), higher than BTT-H2. The COF BTT-H3 also produced up to 550 μmol g⁻¹ h⁻¹ of H₂O₂ under natural sunlight, highlighting its

potential for practical solar-driven applications. It is well known that COFs have traditionally been built from aromatic linkers because their π-π stacking promotes high crystallinity and provides continuous π-channels for efficient exciton and charge transport. Despite these advantages, aromatic linkers are often hydrophobic, which reduces water affinity and limits the efficiency of COFs in aqueous photocatalytic systems. To overcome this challenge, Zhu and co-workers demonstrated that aliphatic linkers can also form crystalline COFs and show subsequent enhancement in their hydrophilicity by reacting with aliphatic linkers such as tartronic acid dihydrazide (TAH) or butanedioic acid dihydrazide (BAH) with 1,3,5-triformylphloroglucinol (TP) that resulted in, two hydrazone-linked COFs, termed as TAH-COF and BAH-COF (Figure 13e).¹³⁹ These two COFs are crystalline and have a BET surface area of 703 m² g⁻¹ and 530 m² g⁻¹ for TAH-COF and BAH-COF. These aliphatic linkers create dense hydrogen-bonding networks that stabilise the framework, enhance crystallinity, and ensure good compatibility with water while maintaining strong visible-light absorption. As a result, the COFs display narrow optical band gaps (~1.9 eV) and high photocatalytic activity, with TAH-COF delivering an impressive H₂O₂ production rate of 6003 μmol g⁻¹ h⁻¹ without sacrificial agents (Figure 13f). The aliphatic TAH-COF also showed notable structural integrity after photocatalysis, as highlighted by the nominal difference in PXRD of before and after photocatalysis (Figure 13g). The influence of linkage orientation on photocatalytic H₂O₂ production has also been clearly illustrated through the work of Yue et al.¹⁴⁰ Two isomeric COFs: TB-COF and TA-COF, were constructed with identical building blocks but opposite imine-bond orientations (Figure 14a). Although the structural difference between the two frameworks is subtle, their photocatalytic behaviours diverge sharply. The orientation present



Table 3: Summary of the representative linkage modification on COFs photocatalysts towards H₂O₂ photosynthesis

View Article Online

DOI: 10.1039/D6SC01670G

Sl. No	Catalyst	Reaction condition	Dosage (mg) & volume (mL)	H ₂ O ₂ Yield (μmol g ⁻¹ h ⁻¹)	AQY	SCC	Ref
1.	<i>o</i> -COFTpPzda	H ₂ O and O ₂	5 mg & 40 mL	4396	-	0.46%	136
2.	TZ-COF	H ₂ O: BA (1:1), O ₂	15 mg & 30 mL	4951	0.6% @ 475 nm	0.036%	137
3.	AmCOF-1	H ₂ O and O ₂	Membrane based	4353	8.72 % @ 420 nm	-	134
4.	COF-TPT-Azo	H ₂ O (pH 11) and O ₂	10 mg & 40 mL	1498	-	-	135
5.	BTT-H3	H ₂ O and O ₂	5 mg & 10 mL	1770	17.7% @ 467 nm	2.02%	138
6.	TAH-COF	H ₂ O	5 mg & 50 mL	6003	7.72% @ 500 nm	0.66%	139
7.	TB-COF	H ₂ O	1 mg & 8 mL	5186	3.45% @ 420 nm	1.08%	140
				4111 α			
8.	PT-PB-COF	H ₂ O and O ₂	5 mg & 20 mL	2169	0.74%	0.055%	141
9.	COF-Tfp-BDDA	H ₂ O and O ₂	10 mg & 20 mL	880	-	-	142

Light Irradiation: $\lambda > 420$ nm, α Sunlight, BA: Benzyl alcohol

in TB-COF generates a larger dipole moment and promotes more efficient charge separation, which together account for its markedly higher H₂O₂ production compared with TA-COF. Both COF show notable H₂O₂ production both in O₂ and air-saturated water (Figure 14b). The H₂O₂ production of TB-COF was measured to be 5186 and 4111 μmol g⁻¹ h⁻¹ in air-saturated water and natural seawater, respectively, which is higher than that of TA-COF (2387 and 1640 μmol g⁻¹ h⁻¹). A similar study was also reported by Zhou et al, where they synthesised constitutional-isomerised COFs (PB-PT-COF and PT-PB-COF) by swapping monomers around imine bonds.¹⁴¹ The two isomeric COFs have similar composition and pore sizes but discrete optoelectronic properties, leading to distinct photocatalytic efficiency. Consequently, under O₂-saturated conditions, PB-PT-COF and PT-PB-COF generated 1076 and 2169 μmol g⁻¹ h⁻¹ of H₂O₂, respectively. In contrast, when the reaction was carried out in N₂-saturated water, PB-PT-COF delivered a higher activity (645 μmol g⁻¹ h⁻¹) than PT-PB-COF (349 μmol g⁻¹ h⁻¹) (Figure 14c). DFT calculations revealed that PT-PB-COF has a stronger affinity for O₂ and activates it more effectively, thereby favouring H₂O₂ formation through the ORR pathway. PB-PT-COF, on the other hand, interacts more strongly with H₂O, leading to H₂O₂ production primarily via the WOR pathway (Figure 14d).

Tuning structural topology in COF for photocatalytic H₂O₂ production:

Topological structures, such as lattices, aggregations, and textural configurations, are fundamental in natural and synthetic systems.¹⁴³ In nature, these structures can be found in various biological, geological, and chemical systems.¹⁴⁴ The pursuit of designing and engineering topological structures at the molecular and atomic scale is driven by the potential to create materials with unprecedented precision and performance. At these small scales, the properties of materials can be radically different from those at the macro scale, often exhibiting enhanced or entirely new functionalities, such as

improved strength, electrical conductivity, or catalytic activity. In reticular chemistry,¹⁴⁵ COFs with various topologies can be designed by manipulating the arrangement of building blocks through geometric control. This method enables the creation of highly ordered structures by linking organic molecules with covalent bonds, offering precise tuning of properties such as surface area, stability, and functionality. The impact of various factors, such as changes in linkage, functional groups, and D-A incorporation, on the optical and electronic properties of COFs for H₂O₂ production has been extensively studied. Recently, there has been growing interest in exploring how topological changes in COFs influence their performance in H₂O₂ production. For instance, Yue et al. investigated the impact of topology on the photocatalytic production of H₂O₂ in 2D COFs.¹⁴⁶ They synthesised two 2D COFs, TBD-COF and TBC-COF, which exhibit similar chemical components but different topologies (Figure 15a). TBD-COF exhibited a cpt topology with six-arm cores, while TBC-COF displayed an hcb topology with three-arm cores. The topological differences have brought distinct variation in the photophysical properties of these two COFs. In addition, it has also influenced mass transport and charge transfer modulation, enhancing their photocatalytic performance for H₂O₂ production (Figure 15b). On evaluating the catalytic property towards light-driven H₂O₂ production, TBD-COF outperforms TBC-COF, producing H₂O₂ at a rate of 5448 and 4049 μmol g⁻¹ h⁻¹ from air and pure water. When evaluated for photocatalytic H₂O₂ production, TBD-COF exhibits superior performance over TBC-COF, showing a steady increase in H₂O₂ yield with prolonged irradiation, particularly beyond 6 h (Figure 15c). TBD-COF achieves production rates of 5448, higher than TBC-COF (4049 μmol g⁻¹ h⁻¹) using air and pure water. The mechanistic investigation revealed the formation of H₂O₂ through three channels: two distinct 2e⁻ ORR routes involving superoxide (O₂-O₂⁻ → H₂O₂) and singlet oxygen species (O₂-O₂¹ → O₂¹-H₂O₂), along with one 2e⁻ WOR pathway (H₂O-H₂O₂) (Figure 15d-f). The photocatalytic



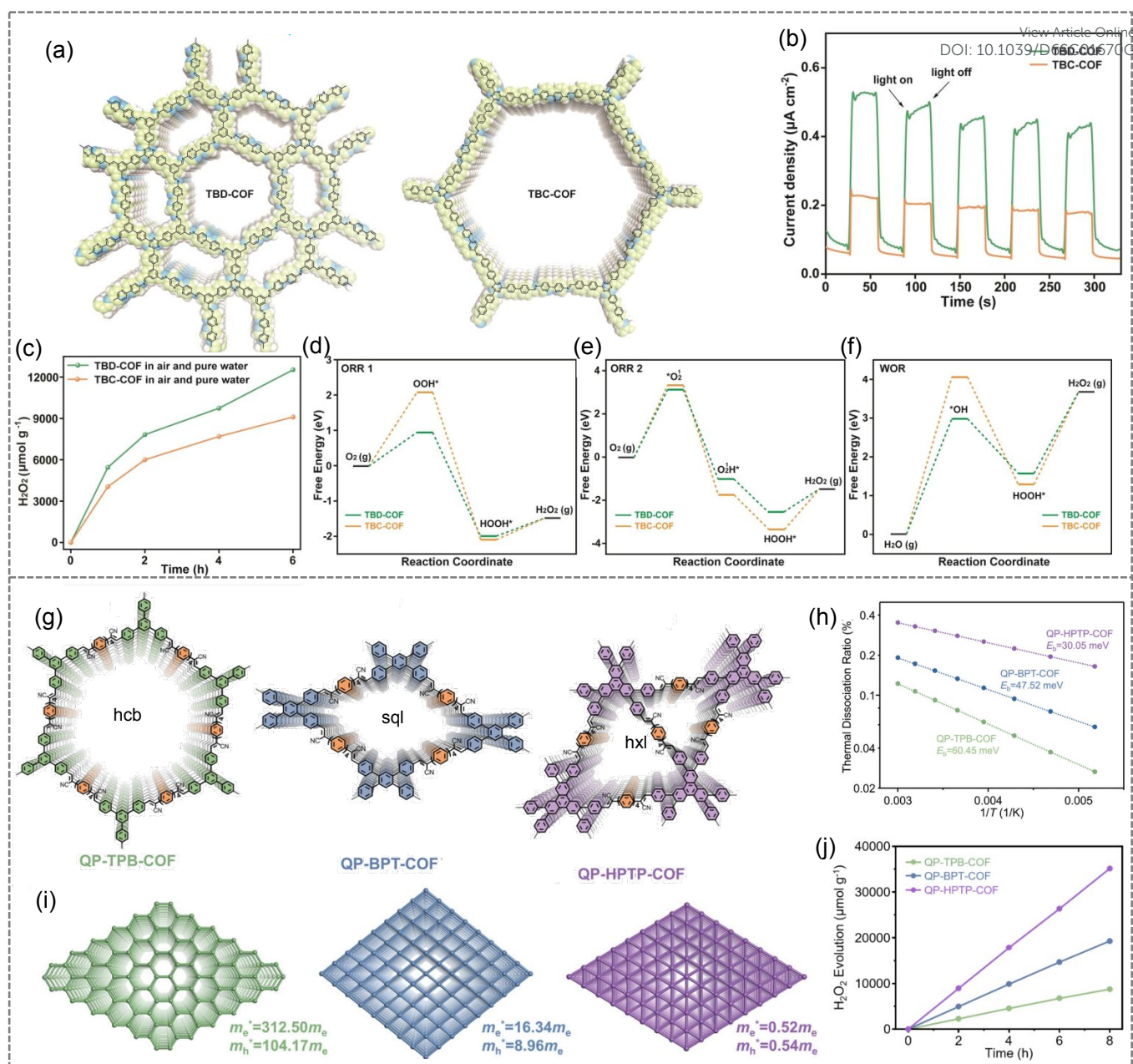


Figure 15: (a) Structures of TBD-COF and TBC-COF. (b) Photocurrent plot of TBD-COF and TBC-COF. (c) Photocatalytic H_2O_2 production comparison between TBD-COF and TBC-COF. (d-f) Gibbs free energy diagrams of TBD-COF and TBC-COF for H_2O_2 photoproduction via (d) $\text{O}_2^- - \text{O}_2^- - \text{H}_2\text{O}_2$ pathway, (e) $\text{O}_2^- - \text{O}_2^- - \text{O}_2^- - \text{H}_2\text{O}_2$ pathway, and (f) $2e^-$ -WOR pathway. (Reproduced and reprinted with permission from the Ref.¹⁴⁶ Copyright 2024 Wiley-VCH GmbH) (g) Structures of COF with different topologies. (h) Exciton dissociation rates in COFs. (i) Schematic illustration of the correlation between topology and effective masses (m_e^* and m_h^*) in different COFs. (j) Long-term H_2O_2 photoproduction over 8 h using P-TPB-COF, QP-BPT-COF, and QP-HPTP-COF. (Reproduced and reprinted with permission from the Ref.¹⁴⁷ Copyright 2024 Wiley-VCH GmbH)

generation of H_2O_2 is generally accompanied by its decomposition, typically following zero-order and first-order kinetics, respectively. For example, TBD-COF and TBC-COF exhibit H_2O_2 formation rate constants (k_f) of 0.84 and 0.64 mM h^{-1} , while the corresponding decomposition rate constants (k_d) are 0.49 and 0.54 h^{-1} . Long-term irradiation studies further illustrate a characteristic production-decomposition interplay. The concentration of H_2O_2 increases steadily during the initial reaction period (up to 10 h), followed by a gradual decline as decomposition becomes dominant. This behaviour is often associated with photocatalyst fatigue or partial structural

degradation under extended light exposure, induced by reactive oxygen species and accumulated charge carriers, which leads to reduced crystallinity and consequently shifts the balance toward faster H_2O_2 breakdown. The effect of topology on H_2O_2 production has also been meticulously studied by Xu et al, where they have synthesised three 2D sp^2 carbon-linked π -conjugated COFs, such as QP-TPB-COF, QP-BPT-COF, and QP-HPTP-COF, having hcb, sql, and hxl topology, respectively (Figure 15g).¹⁴⁷ Compared to COFs adopting hcb or sql lattices, the hxl-topology QP-HPTP-COF stands out by exhibiting the lowest exciton binding energy (E_b), markedly



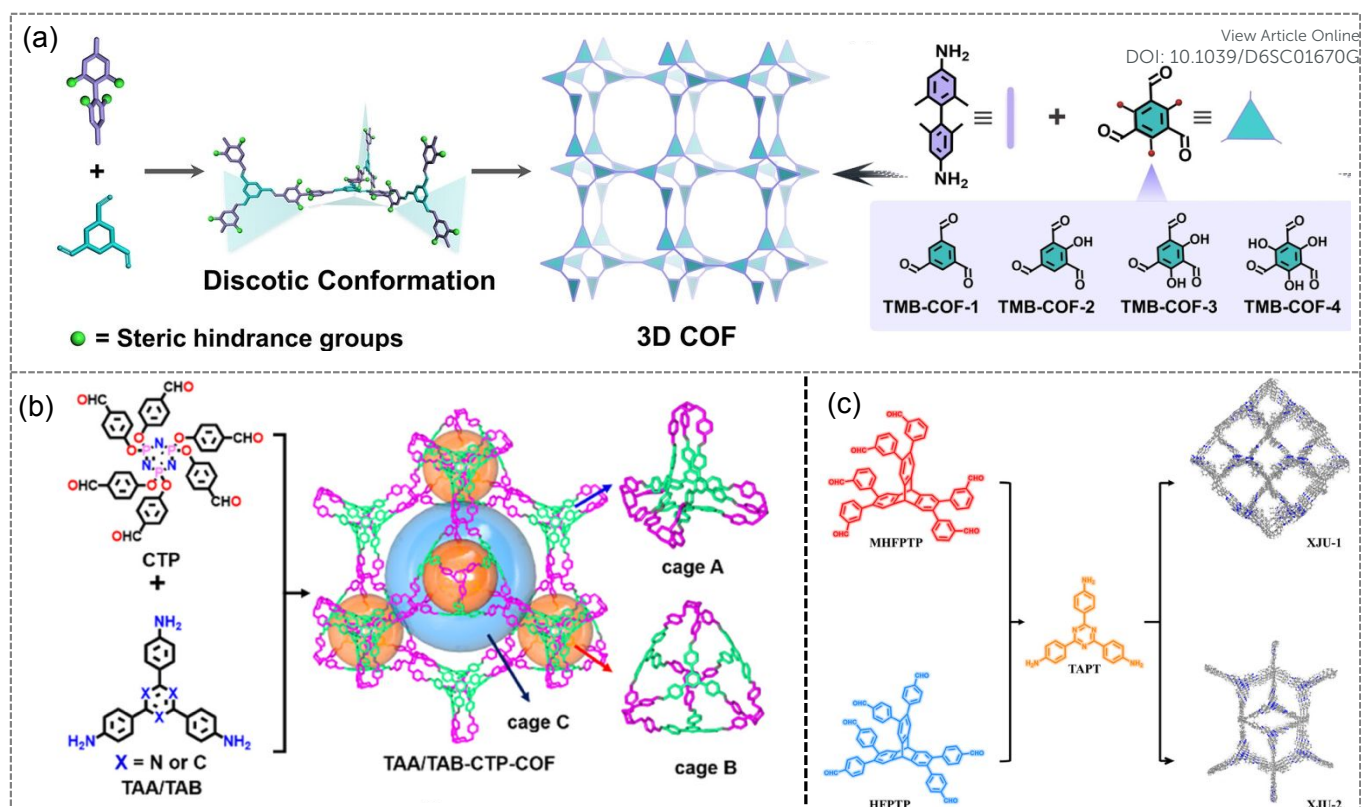


Figure 16. (a) Schematic route of formation of 2D COF using planar and linear monomers (Reprinted with permission from ref.¹⁴⁸ Copyright 2024 Wiley-VCH GmbH) (b) Schematic route to synthesis of 3D COF. (Reprinted with permission from ref.¹⁴⁹ Copyright 2024, American Chemical Society) (c) Synthetic scheme of 3D COFs XJU-1 and XJU-2. (Reprinted with permission from ref.¹⁵⁰ Copyright 2025 Wiley-VCH GmbH)

reduced carrier effective masses, and the highest charge-transfer efficiency (Figure 15h). To probe the topology-dependent electronic characteristics of COFs, the effective carrier masses (m^*) were evaluated through DFT calculations. Notably, QP-HPTP-COF displayed remarkably lower electron and hole effective masses ($m_e = 0.52m_e$; $m_h = 0.54m_e$) relative to QP-TPB-COF ($m_e = 312.5m_e$; $m_h = 104.17m_e$) and QP-BPT-COF ($m_e = 16.34m_e$; $m_h = 8.96m_e$) (Figure 15i), suggesting a substantially higher intrinsic carrier mobility and, consequently, enhanced photocatalytic potential for QP-HPTP-COF. Consequently, the photocatalytic tests conducted in O_2 -saturated pure water under visible light irradiation revealed the highest efficiency for QP-HPTP-COF with the hxl topology, followed by QP-BPT-COF with the sql topology, and finally QP-TPB-COF with the hcb topology. The respective H_2O_2 production rates for these materials were 4388, 1902, and 921 $\mu\text{mol g}^{-1} \text{h}^{-1}$ (Figure 15j). QP-HPTP-COF also exhibited an AQE of 22.78% and an SCC of 1.41%, the highest reported SCC value among other COFs. The synthesis of 3D COFs with high surface area, exposed active sites, and tunable frameworks has gained interest among researchers. However, synthesising 3D COF compromises various challenges, such as low-connectivity building units, low crystallinity, low yield, etc. With the use of a tetrahedral linkage, Omar M. Yaghi has reported the first 3D COFs in 2007.¹⁵¹ Since then, various 3D COFs have been synthesised, and different types of topologies have been reported for 3D COFs.¹⁵² The construction of 3D COFs generally demands linkers with predefined spatial orientation and high-connectivity nodes. In contrast to 2D

COFs, only a limited number of frameworks have been realised, primarily due to the synthetic complexity, harsh reaction conditions, scarcity of suitable 3D linkers, such as tetrahedral, hexavalent triangular prisms, anti-triangular prisms, and octavalent cubic units, and the inherent crystallisation difficulty arising from multiple degrees of rotational freedom. Recently, progress has been made through strategies that exploit the torsional characteristics of linkers, where modulation of the torsion angle enables the formation of stable 3D COF networks.¹⁵³ In line with this approach, Zhu et al. demonstrated a successful synthesis of a 3D COF by utilising controlled molecular torsion to drive the 3D framework.¹⁴⁸ They deliberately chose 2,2',6,6'-tetramethylbenzidine (TMB) as a linker where the four methyl groups introduce steric hindrance between the two phenyl rings, generating a stereoscopic disc-like conformation that preserves local planarity while promoting antiparallel stacking (Figure 16a). Four COFs were subsequently synthesised by coupling TMB with a series of trialdehydes containing varying numbers of hydroxyl groups (ranging from 0 to 3) (Figure 16a). The steric hindrance in TMB introduces an additional force that alters the torsion angles of the peripheral triangular units, directing the linear unit to connect with the trigonal unit and adapted 3D srs topology. By exploiting steric hindrance effects, these 3D COFs exhibit exceptionally high surface areas and well-defined pore architectures, which collectively promote greater exposure of catalytic sites and facilitate efficient mass transport. A clear structure-activity trend is observed: as the number of ketone-based



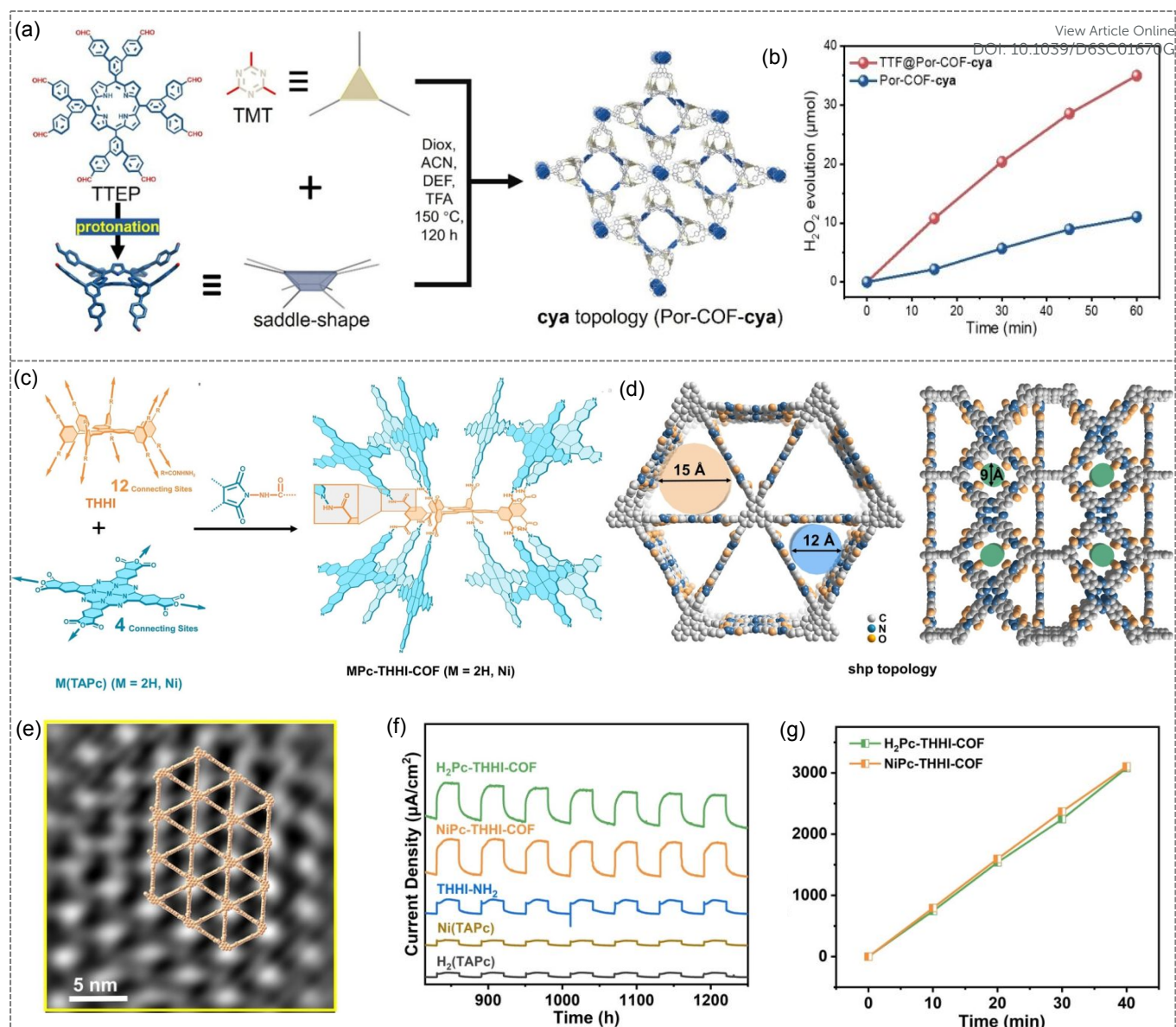


Figure 17: (a) Synthetic scheme for cya topology-based Por-COF-cya. (b) Reaction kinetics for H₂O₂ production. (Reprinted with permission from Ref.¹⁵⁴ Copyright 2024 Wiley-VCH GmbH) (c) Synthetic scheme of MPc-THHI-COF (M=2H, Ni) with 12 connecting sites. (d) Simulated packing structures in MPc THHI-COF (M=2H, Ni) along c axis (left) and a or b axis (right). (e) HRTEM images for H₂Pc-THHI-COF (f) photocurrent comparison of different 3D THHI-COF. (g) Kinetics for H₂O₂ production with H₂Pc-THHI-COF and NiPc-THHI-COF. (Reprinted with permission from Ref.¹⁵⁵ Copyright 2024 Wiley-VCH GmbH).

active sites increases, the photocatalytic H₂O₂ production performance improves accordingly. Under pure water and O₂-saturated conditions, TMB-COF-1, TMB-COF-2, and TMB-COF-3 deliver H₂O₂ formation rates of 218, 1293, and 2621 μmol g⁻¹ h⁻¹, respectively, while TMB-COF-4 achieves an impressive 5106 μmol g⁻¹ h⁻¹. TMB-COF-4 also exhibited H₂O₂ photocatalytic production rate of 1396 μmol g⁻¹ h⁻¹ under pure water and air conditions. In comparison, the analogous 2D BZD-COFs demonstrate considerably lower activity under identical conditions. Collectively, these findings highlight the strong correlation between 3D framework design, active-site incorporation, and photocatalytic efficiency, emphasising that deliberate structural optimisation is a powerful strategy for advancing COF-mediated H₂O₂ production. Since topology strongly

influences parameters such as pore arrangement, charge-transfer pathways, and crystallinity, different 3D COFs inherently exhibit diverse property profiles and performance behaviours. The photocatalytic performance of two topologically distinct 3D COFs for H₂O₂ production was recently reported by Liao et al. Two 3D COFs (TAA/TABCTP-COF) are obtained by reacting a trigonal antiprism (C3) monomer, denoted as CTP, with a planar amine linker monomer, denoted as TAA or TAB (Figure 16b).¹⁴⁹ CTP has N, O, and P that can act as active sites for WOR, whereas the amine linker has triazine (TAA) or benzene (TAB) in its core that acts as an acceptor to photogenerated electrons during ORR. The triazine-containing COF, denoted as TAACTP-COF, produced H₂O₂ at a rate of 1041 μM h⁻¹ from H₂O and O₂. In the presence of isopropanol as a sacrificial agent,



Table 4: Summary of the representative Topological and Structural modifications on COF photocatalysts towards H₂O₂ photosynthesis

View Article Online

DOI: 10.1039/D6SC01670G

Sl. No	Catalyst	Reaction condition	Dosage (mg) & volume (mL)	H ₂ O ₂ Yield (mmol g ⁻¹ h ⁻¹)	AQY	SCC	Ref
1.	TBD-COF	H ₂ O	1 mg & 8 mL	5448	5.95%@420 nm	0.90%	146
2.	QP-HPTP-COF	H ₂ O and O ₂	30 mg & 10 mL	4388	22.78%@420 nm	1.41%	147
3.	TMB-COF-4	H ₂ O and O ₂	-	5106	-	-	148
4.	TAA-CTP COF	H ₂ O and O ₂	10 mg & 5 mL	1041 mM h ⁻¹	-	-	149
5.	XJU-1	H ₂ O:BA EtOH (9:1), O ₂	5 mg & 20 mL	34777	9.7%@380 nm	-	150
6.	TTF@Por-COF-cya	H ₂ O	5 mg & 50 mL	6994	14.98%@420 nm	-	154
7.	H2Pc-THHI-COF	H ₂ O and O ₂	5 mg & 50 mL	4511	-	-	155

Light Irradiation: Xe lamp ($\lambda > 420$ nm) BA: Benzyl alcohol

the production rate increased to 2221 $\mu\text{M h}^{-1}$. The theoretical calculation showed that the distribution of HOMO, mostly on the CTP ring and LUMO on TAA or TAB, indicates CTP as an oxidising site for WOR and TAA/TAB as a reducing site for ORR. The unprecedented efficiency of 3D COFs over 2D COFs has also been recently reported by Lu et al. Two 3D COFs (XJU-1 and XJU-2) using a hexadentate triptycene-based monomer and a tridentate triazine amine linker were synthesised (Figure 16c).¹⁵⁰ The two COFs are isomeric, having a difference in the linkage position. The 3D COFs exhibit high crystallinity with a ceq topology. The two COFs have distinct photochemical properties, and in the presence of benzyl alcohol, XJU-1 and XJU-2 demonstrated impressive photocatalytic activity for H₂O₂ production, achieving rates of 34,777 $\mu\text{mol g}^{-1} \text{h}^{-1}$ and 11,922 $\mu\text{mol g}^{-1} \text{h}^{-1}$, respectively. In the absence of a sacrificial agent, the production reached up to 7453 and 8124 $\mu\text{mol g}^{-1} \text{h}^{-1}$, for XJU-1 and XJU-2, respectively. The larger pore aperture of XJU-1 relative to XJU-2 promotes faster mass diffusion and more efficient O₂ activation, resulting in enhanced H₂O₂ output. Mechanistic studies (radical quenching, EPR, RDE) confirmed ORR-dominated H₂O₂ formation in both COFs, where XJU-1 follows a mixed $1e^-/2e^-$ ORR process, while XJU-2 mainly adopts a direct $2e^-$ pathway. DFT results further attributed the performance differences to topology-dependent charge separation and strong O₂ binding at multiple active sites. The reduced singlet-triplet energy gap ($\Delta\text{ES-T}$) and orthogonal triptycene structure additionally favour ¹O₂ formation, collectively accelerating H₂O₂ evolution. The study underscores how 3D COF topology governs ORR selectivity and boosts photocatalytic H₂O₂ production efficiency. The synthesis of COF with connectivity up to four is well known, and its synthesis procedure has been generalised. However, designing 3D COFs with high connectivity (≥ 8) is challenging and scarce. The higher number of connectivity often associates with high stability of the framework; therefore, it is desirable to synthesise highly connected 3D COFs. Porphyrin units, known for their excellent light-harvesting capability, have been strategically employed as linkers in COF design for photocatalytic H₂O₂ generation. Upon protonation of the pyrrole nitrogen, the porphyrin macrocycle undergoes pronounced geometric distortion both within and out of the molecular plane, which can significantly influence charge separation and exciton dynamics. Leveraging this structural tunability, Jiang et al. synthesised two three-dimensional porphyrin-based COFs (Por-COF-cya) featuring vinyl linkages through an aldol condensation reaction.¹⁵⁴ Por-COF-cya adopts a first-ever-

reported cya topology that has the interconnectedness of 8-connected and 3-connected nodes (Figure 17a). The incorporation of porphyrin units into the Por-COF-cya framework imparts favourable photophysical and chemical stability. Moreover, the electron-deficient triazine moieties enable efficient encapsulation of the electron-donating tetrathiafulvalene (TTF) species within the hierarchical pores via electrostatic attraction and host-guest interactions. This results in the formation of a donor-acceptor architecture (TTF@Por-COF-cya) that promotes rapid charge transfer and ultimately enhances photocatalytic H₂O₂ production. Consequently, the H₂O₂ yield in pure aqueous solution reached 2209 and 6994 $\mu\text{mol g}^{-1} \text{h}^{-1}$ with Por-COF-cya and TTF@Por-COF-cya (Figure 17b). Analysis of H₂O₂ yields under different atmospheres, supported by isotope-labelling experiments, confirmed that 84% of the oxygen atoms in the generated H₂O₂ originated from the ORR pathway, while the remaining 16% were derived from the WOR route. DFT calculations identified two potential electrophilic sites in Por-COF-cya: the non-protonated porphyrin nitrogen and the triazine ring, where O₂ showed preferential adsorption at the triazine site, consistent with in-situ DRIFTS results and confirming it as the primary ORR-active centre. Moreover, TTF@Por-COF-cya displayed lower O₂ adsorption free energy and reduced intermediate-conversion barriers compared to Por-COF-cya, facilitating $\bullet\text{OOH}$ formation and thereby enhancing H₂O₂ production efficiency. Highly connected 3D COF for photocatalytic H₂O₂ production has also been reported by Wang et al.¹⁵⁵ They synthesised highly connected phthalocyanine-based (Pc-based) two 3D COFs MPc-THHI-COFs (M=H₂, Ni) with 12 connecting sites (Figure 17c). These COFs were found to adopt a shp topology, featuring 1D triangular channels with diameters of 12 Å and 15 Å along the *c* axis, which are further interconnected by rhombohedral windows, each with a size of 9 Å along the *a* and *b* axes (Figure 17d). The triangular channels similar to the open channel of the SHP networks of the COF can be visualised through HRTEM images, indicating the high crystallinity of the synthesised 3D COF (Figure 17e). The synthesised 3D COFs exhibit a broadened visible light absorption range, a narrow optical band gap, and 3D interconnected nanochannels, which collectively enhance their photocatalytic performance. These features enable efficient H₂O₂ generation at a rate of 4511 and 4589 $\mu\text{mol g}^{-1} \text{h}^{-1}$ from O₂-saturated H₂O via $2e^-$ ORR and WOR pathways under visible-light irradiation (Figure 17f).



Microenvironment tuning in COF for efficient H₂O₂ Production

The microenvironment usually refers to the local chemical and structural surroundings within and around the framework where catalytic reactions occur. The concept of microenvironment in COF has emerged as a critical determinant of their functional behaviour, particularly in catalysis. Beyond framework composition, the confined pore space, including its topology, chemical polarity, electronic distribution, and host-guest interactions, collectively shapes how reactants diffuse, adsorb, and activate within the lattice. Despite being a well-defined and widely applied strategy in zeolite catalysis, microenvironment control in COF-based catalysts is only beginning to emerge, offering substantial room for advancement.¹⁵⁶ The modulation in the microenvironment dictates molecular diffusion, O₂ adsorption, charge separation, and intermediate stabilisation. By tailoring these confined reaction spaces, COFs can selectively promote the 2e⁻ ORR/ WOR pathway while suppressing side reactions, enabling efficient H₂O₂ generation under mild conditions. In a recent report, Guo and co-workers revealed that Pauli repulsion combined with electron interactions leads to uneven electron distribution in COFs, creating selective O₂ binding sites that promote efficient photocatalytic H₂O₂ generation.¹⁵⁷ Two COFs were synthesised for further study, namely, TAPT-FTPB and TAPT-BPDB, with asymmetric and symmetric local electron distribution (Figure 18a). Their findings indicate that TAPT-FTPB COFs, featuring a locally asymmetric electron distribution, exhibit enhanced oxygen adsorption capacity and stronger adsorption interactions, contributing to improved photocatalytic performance. Consequently, H₂O₂ production of 3780 μmol g⁻¹ h⁻¹ was achieved (Figure 18b) with an SCC of 1.22%. The TAPT-FTPB also shows long-term H₂O₂ production over 30 h and exhibits no degradation after ten continuous cycles (Figure 18c). Similarly, Ding et al. reported a one-pot “grafting-to” approach to modulate the local electronic environment within a series of isoreticular multicomponent COFs (Figure 18d).¹⁵⁸ By incorporating electron-donating or electron-withdrawing groups into the pore channels, they successfully converted photo-inert COFs into photoactive ones through the formation of intramolecular D-A architectures. Remarkably, the COF functionalized with electrophilic 2-aminothiazole delivered an impressive H₂O₂ production rate of 3701 μmol g⁻¹h⁻¹ and attained a SCC efficiency of 0.13%. Recently, Zhang et al. reported the impact of

microenvironment regulation in COFs on overall photocatalytic activity by varying the number of nitrogen atoms within the framework.¹⁵⁹ An increased number of nitrogen atoms effectively modulated the local microenvironment and enhanced the electrophilicity of the COF. Among the series, the COF with the highest nitrogen content demonstrated superior performance, achieving efficient photogenerated charge separation and maximising H₂O₂ production from natural resources like sunlight and seawater. A remarkable H₂O₂ generation rate of 4881 μmol g⁻¹ h⁻¹ was attained. Typically, organic polymeric materials, including COFs, exhibit an exciton diffusion distance of only 5-10 nm, which is significantly smaller than the overall particle size of COFs.¹⁶⁰ As a result, it is believed that modifying the local structure within small domains of the COF, rather than across the entire particle, can more effectively enhance charge transfer and thereby improve photocatalytic performance. To elucidate the structure-activity relationship governing H₂O₂ generation in COFs, Guo et al. synthesised a series of quinoline-based COFs bearing different functional groups—COFs-R (R = -OH, -OMe, -H, -Br, -CN)—using a multicomponent reaction (MCR) strategy (Figure 18e).¹⁶¹ Inspired by natural enzyme systems, where catalytic efficiency is finely tuned by microenvironmental regulation, the authors introduced these diverse functional groups into the COF. The quinoline backbone, resembling that of glucose oxidase, allows its catalytic behaviour to be modulated by the attached R-groups. The aldehyde and amine building blocks used to construct the framework both contain a triazine core, making these COFs inherently highly electrophilic. Thus, as the electron-donating strength of the substituents increases, the overall donor character of the framework is enhanced, leading to improved D-A charge-separation efficiency. As a result, H₂O₂ generation reaches up to 4458 μmol g⁻¹ h⁻¹, with most electron-donating functional groups (COF-OH), and with most electron-withdrawing functional groups (COF-CN), it reaches only 2032 μmol g⁻¹ h⁻¹ (Figure 18f). This was further evidenced by a similar performance trend in pure water, showing a negative correlation with the Hammett σ_p values of the -R group, irrespective of the presence or absence of a sacrificial agent. (Figure 18g). A change in the local structure of COF was also achieved by Jiang et. al. by conducting a three-component solvothermal reaction between

Table 5: Summary of the representative microenvironment tuning on COF photocatalysts towards H₂O₂ photosynthesis

Sl. No	Catalyst	Reaction condition	Dosage (mg) & volume (mL)	H ₂ O ₂ Yield (mmol g ⁻¹ h ⁻¹)	AQY	SCC	
1.	TAPT-FTPB	H ₂ O and O ₂	10 mg & 10 mL	3780	-	1.22%	157
2.	COF-Thz	H ₂ O	2 mg & 40 mL	3701	22.78%@420 nm	1.41%	158
3.	N ₃ -COF	H ₂ O and O ₂	10 mg & 50 mL	4820	1.5%@420 nm	0.413%	159
4.	COF-OMe	H ₂ O:BA (9:1)	5 mg & 18 mL	5497	6.5%@420 nm	0.16%	161
5.	USTB-10-S	H ₂ O:BA (1:1)	2.5 mg & 25 mL	16152	4.98%@420 nm	0.06%	162
Light Irradiation: Xe lamp ($\lambda > 420$ nm) BA: Benzyl alcohol							



diamines, thiadiazole-based tetraaldehydes, and sulfur (Figure 18h).¹⁶² The reaction yielded mixed USTB-x-S (x=7-10) COFs, which are composed of approximately 90% imine and 10% thiazole linkages. Compared to their fully imine-linked D-A counterparts (USTB-7-10), the USTB-x-S series demonstrated significantly enhanced photocatalytic performance, with H₂O₂ production rates

increased by 77-95% in pure water under O₂. Notably, USTB-10-S achieved a rate of 5041 μmol g⁻¹ h⁻¹, which further increased to 16,152 μmol g⁻¹ h⁻¹ upon the addition of benzyl alcohol as a sacrificial agent. This work highlights that the minor local structural modifications in COFs can markedly improve charge separation, thereby boosting photocatalytic performance.

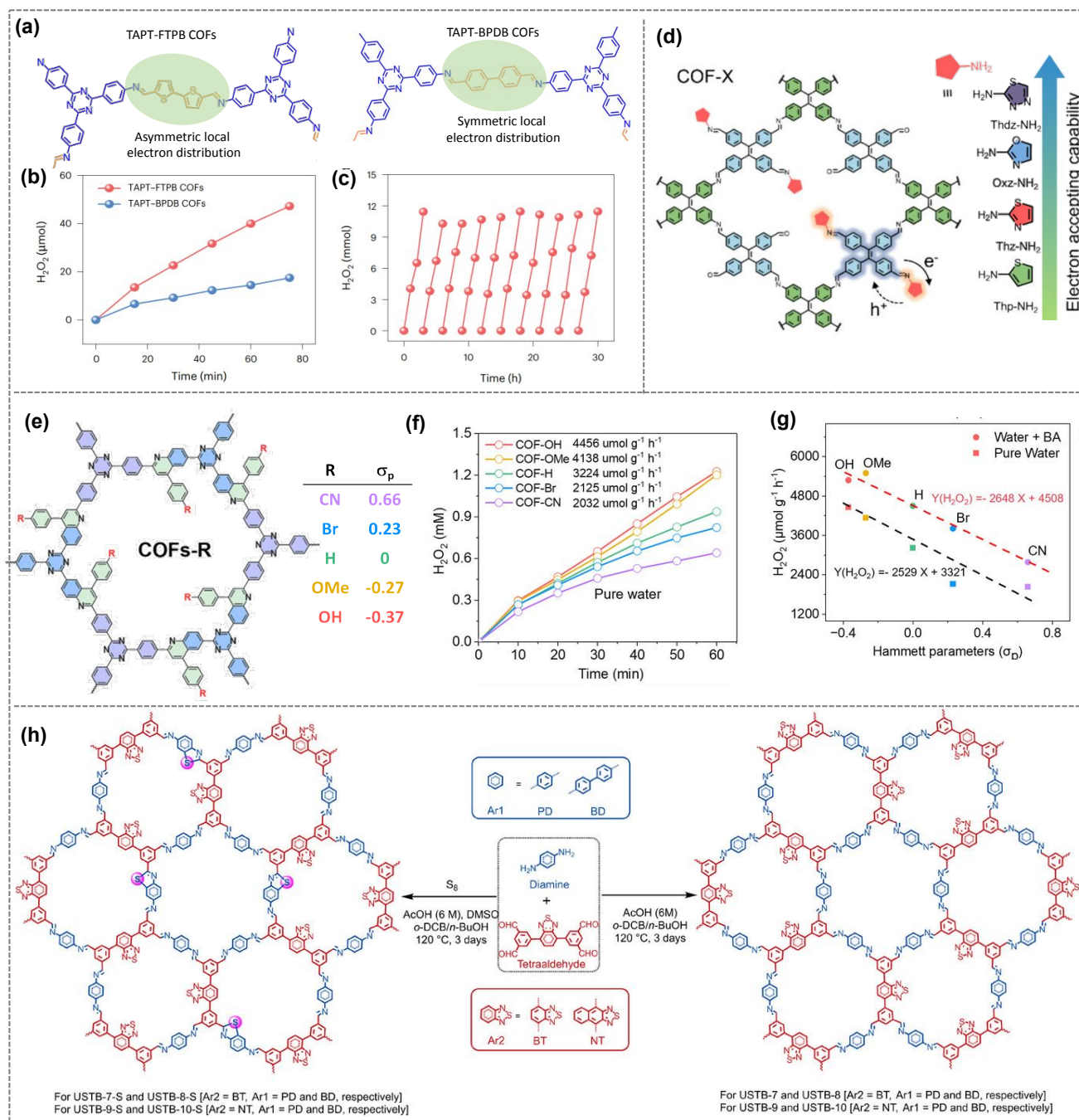


Figure 18: (a) Structures of TAPT-FTP-COF and TAPT-BPDB-COF highlighting symmetric and asymmetric local electron distribution. (b) Kinetics of two COFs for H₂O₂ production. (c) Recyclability experiment of TAPT-FTP-COF over 30 h. (Reprinted with permission from ref¹⁵⁷ Copyright 2025, Springer Nature) (d) Schematic representation of the structure of the COF synthesised through the one-pot 'grafting-to' and its different functional groups. (Reprinted with permission from ref¹⁵⁸ Copyright 2025, American Chemical Society) (e) Structure of COFs-R synthesised through multivariate reaction. (f) Photocatalytic H₂O₂ production comparison of COFs-R (g) Hammett plot showing the relation between the photocatalytic performance of COFs-R and Hammett parameters. Reproduced and reprinted with permission from the ref.¹⁶¹ (h) Schematic representation of the synthesis of USTB-COF. Reprinted with permission from ref¹⁶² Copyright 2024 Wiley-VCH GmbH)



Metal-organic frameworks (MOFs) based photocatalyst towards H₂O₂ production:

A significant class of crystalline porous materials, MOF, comprises metal ions or clusters and organic ligands. They have a large specific surface area, regular and controllable pore structures, and various chemical compositions and functionalities, including the ability to tune the metal centre.^{163–166} By altering the kinds of ligands and/or metal nodes, it is possible to rationally tailor the chemical reaction conditions and electrical structures of active centres for specific purposes.^{167,168} The increased porosity speeds up mass movement throughout the network of MOFs and encourages the exposure and accessibility of active sites. The high metal content, ordered crystallinity, large surface area, and adjustable pore size of MOFs have made them attractive candidates for various applications, such as catalysis,^{169–171} gas storage and separation,^{172–174} environmental remediation,^{175,176} sensing,^{177–179} biomedical applications.¹⁸⁰ Towards photocatalysis, the intrinsic photocatalytic properties of MOFs arise from their tunable band structure, photoactive metal nodes, and π -conjugated organic linkers. These features enable efficient light harvesting via the antenna effect of linkers, which transfer energy to metal sites through linker-to-metal charge transfer (LMCT), mimicking semiconductor behaviour with adjustable band gaps for visible-light response. Their high porosity and large surface area provide abundant accessible active sites and facilitate mass transport of reactants, while the ordered crystalline framework promotes directional charge transport. Additionally, internal electric fields originating from polar structures or donor-acceptor architectures enhance charge separation and suppress electron-hole recombination. Strong metal-ligand coordination imparts chemical and photostability, and selective adsorption of substrates such as O₂, CO₂, or H₂O further improves catalytic efficiency and selectivity, making MOFs intrinsically well-suited for photocatalytic applications. Recently, Park et al. have synthesised copper-based electrically conductive MOF and introduced a D-A moiety by integrating spatially separated electron D-A moieties via click reaction (Figure 19a).¹⁸¹ After the click reaction in MOF with phenylacetylene (PA) and 1-Ethynyl-4-fluorobenzene (EFB), the researcher observed the tuning in the band positions that further aligned with the redox potential of photocatalytic H₂O₂ production. Fluorine incorporation facilitates efficient charge separation by suppressing electron-hole recombination, thereby maximising photocatalytic efficiency. The photosynthesis of H₂O₂ with synthesised MOFs has been explored in pure water and O₂ irradiated by a 300 W Xe lamp. The maximum yield was obtained for clicked MOF with EFB, and the H₂O₂ production rate of 1676 $\mu\text{mol g}^{-1} \text{h}^{-1}$ was reported with an AQY of 1.03% at 410 nm. Toward developing the pristine MOF as an efficient photocatalyst, Wang et al. developed a uranyl-organic framework named YTU-W-2 using a mixed ligand strategy where thiophene and pyridine ligands were used (Figure 19b).¹⁸² The introduction of mixed ligands has increased the photon absorption and carrier transfer into the framework. Further, the H₂O₂ rate of 345 $\mu\text{mol h}^{-1} \text{g}^{-1}$ has been reported in a 9:1 water and ethanol mixture. The structural effect of pristine MOF towards photocatalytic

synthesis of hydrogen peroxide has also been recently studied by et al by synthesising two isomeric Ti-based MOF [NH₂-UiO-66(Ti) and NH₂-MIL-125(Ti)] (Figure 19c).¹⁸³ The researcher reported the efficient electron transport of the Ti-O oxygen cluster as NH₂-MIL-125(Ti) has a shorter bond length than NH₂-UiO-66(Ti). Consequently, the photocatalytic activity of NH₂-MIL-125(Ti) was better than NH₂-UiO-66(Ti). Furthermore, the defective structure in MOF was found to acquire more active sites that promote the photocatalytic activity, and the H₂O₂ production of defective NH₂-MIL-125 was found to be efficient among all, with a production rate of 101 $\mu\text{mol g}^{-1} \text{h}^{-1}$. Similarly, Zhou and co-workers engineered MIL-125-NH₂, including coexisting (111) and (001) facets, facilitating the formation of a Z-scheme structure to enhance spatial charge separation.¹⁸⁴ A dual-channel pathway for synthesising H₂O₂ was identified, including the ORR on the (111) facets and OH⁻ oxidation on the (001) facet. The exposure degree of the (111) facet of MIL-125-NH₂ was systematically adjusted by varying the quantities of acetic acid modulator during the preparation process; an increase in acetic acid resulted in a greater exposure modulator during the preparation process; an increase in acetic acid resulted in a greater exposure of (111) facets.¹⁸⁵ The (111) facets may reduce charge transport resistance and extend the lifespan of photo-induced electrons and holes, resulting in an ideal H₂O₂ production rate of 925.8 $\mu\text{mol g}^{-1} \text{h}^{-1}$ (visible light, triethanolamine as a sacrificial agent, pure O₂, indirect ORR). In another study, Zhu and co-workers discovered self-assembled tetrakis(4-carboxyphenyl) porphyrin supramolecular photocatalysts that generate H₂O₂ solely from H₂O and O₂, achieving a production rate of 1.72 mM h⁻¹ at 293 K, with quantum efficiencies of 14.9% at 420 nm and 1.1% at 940 nm.¹⁸⁶ The catalyst attains an SCC efficiency of 1.2% at 328 K under irradiation and heating with simulated sunlight. The findings indicated that photogenerated electrons and holes facilitate H₂O₂ generation by interacting with distinct active sites, such as the pyrrole N-H ring and carboxyl groups. They specifically suggest a hole-induced H₂O₂ generation method, which entails the photoconversion of -COOH to -CO₃H groups on the catalyst, succeeded by thermal breakdown. Furthermore, after 20 cycles, the buildup of photocatalytic H₂O₂ reached about 50 mM, indicating the materials' strong recyclability. The regulation of D-A interaction mode in Zr-based UiO-67 MOF has been recently reported by Guo et al.¹⁸⁷ The author reports the synthesis of a family of UiO-67-type D-A MOFs, in which pyrene, benzothiadiazole, and naphthalene-benzothiadiazole linkers of identical length are co-assembled with Zr₄⁺ nodes (Figure 19d). The precisely tuned short-range (through-bond) and long-range (through-space) D-A interactions were appropriate for the photocatalytic H₂O₂ production from water and O₂ in a water/benzyl alcohol biphasic system. Mixed-linker UiO-67-PENB, the first example of a MOF combining both DA modes in one framework, exhibits optimised band structure, enhanced charge separation, and suppressed recombination. Consequently, through an indirect two-step 2e⁻ ORR pathway with a high H₂O₂ formation rate of 5141 $\mu\text{mol g}^{-1} \text{h}^{-1}$ and an AQY of 4.24% at 400 nm was achieved. The MOF further demonstrated excellent structural and operational stability over 48 h and H₂O₂ accumulation up to ~32 mM. Comprehensive



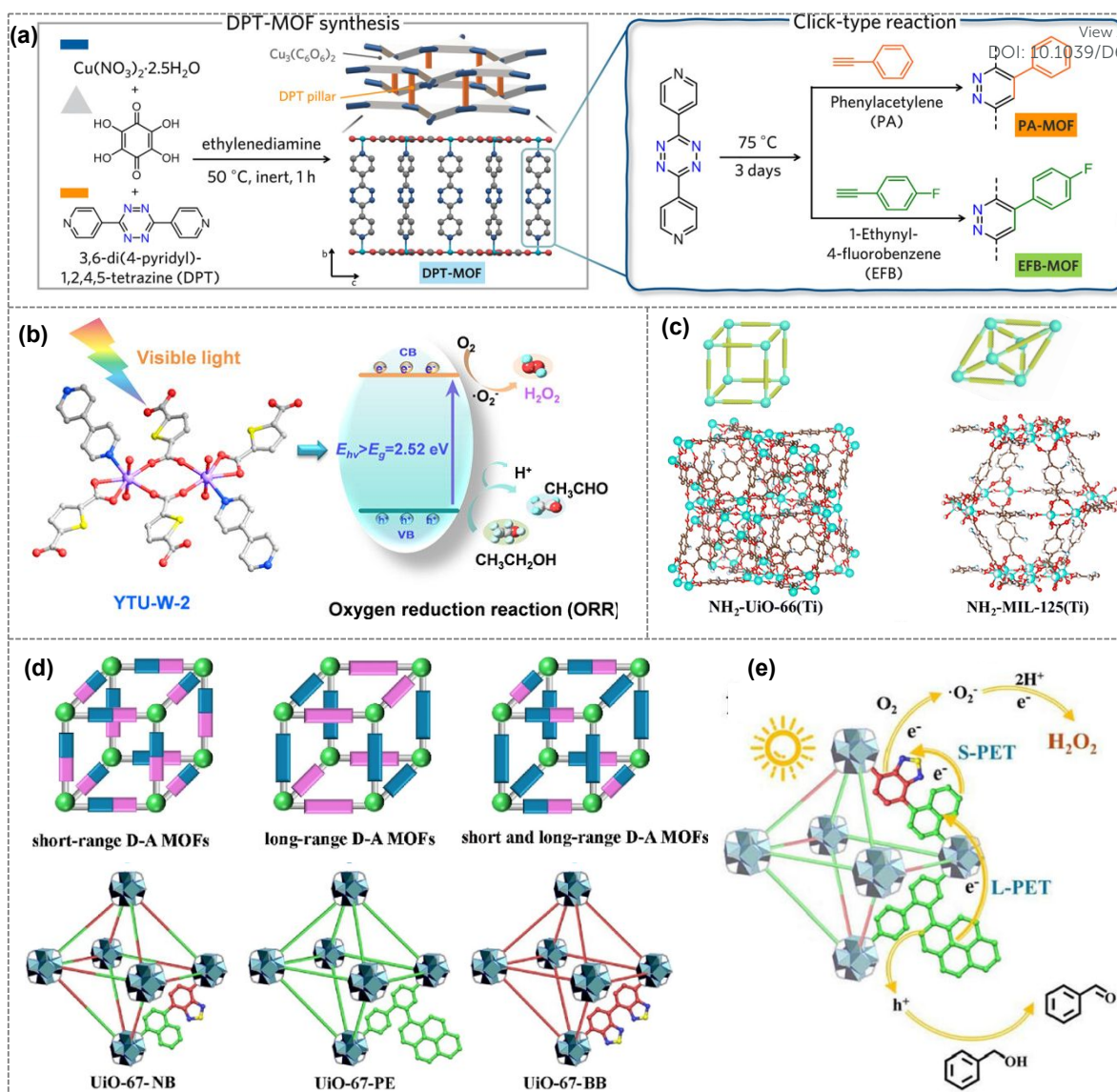


Figure 19: (a) Schematic route for the synthesis of electrically conductive MOF and its post-synthetic click reaction. (Reprinted with permission from ref.¹⁸¹ Copyright 2024, American Chemical Society). (b) Crystal structure of YTU-W2 and its band gap position towards H_2O_2 production. (Reprinted with permission from Ref.¹⁸² Copyright 2024 American Chemical Society) (c) Isomeric structure of isomeric Ti-based MOF; $\text{NH}_2\text{-UiO-66(Ti)}$ and $\text{NH}_2\text{-MIL-125(Ti)}$. (Reprinted with permission from Ref.¹⁸³ Copyright 2024 Royal Society of Chemistry) (d) Illustration of the strategic installation of different donor and acceptor interaction modes and the structure of synthesised UiO-67 -type D-A MOFs. (e) Catalytic Pathway for H_2O_2 photoproduction via the two-step 2e- ORR on UiO-67-PE/NB . (Reprinted with permission from Ref.¹⁸⁷ Copyright 2025 American Chemical Society)

spectroscopic and electrochemical studies (UV-vis DRS, Mott-Schottky, EIS, photocurrent, PL, fs-TA, EPR, in situ DRIFTS) underpin the mechanistic pathway for H_2O_2 photoproduction. The synergistic photoinduced electron transfer from pyrene to the NB-based DA linker, followed by efficient O_2 reduction and effective hole scavenging by benzyl alcohol (Figure 19e). This cooperative process enables UiO-67-PENB to outperform the single-mode D-A analogues UiO-67-NB and UiO-67-PEBB in H_2O_2 production. collectively accounts for the superior H_2O_2 photosynthesis performance that surpasses both single-mode D-A analogues (UiO-67-NB , UiO-67-PEBB). Toward sustainable H_2O_2 generation and its practical utilisation, Pal et al. demonstrated the use of MOFs as an emerging class of thermocatalysts capable of producing H_2O_2 by harvesting small temperature gradients under ambient conditions.¹⁸⁸ In their study, MOFs were immobilised onto carbon fibre fabrics (MOF@CFF)

to construct antibacterial filtration systems activated by temperature cycling. Three representative MOFs (Cu_2BDC , MOF-303 , and ZIF-8) were evaluated and benchmarked against bismuth telluride (Bi_2Te_3), a well-known thermocatalytic material. Among them, ZIF-8 exhibited the highest H_2O_2 production efficiency under low temperature differences, leading to ~96% antibacterial efficacy against *Escherichia coli* and *Staphylococcus aureus*. This work highlights the potential of MOF-based thermocatalysts for thermoelectric-assisted H_2O_2 generation, offering a promising strategy for real-time water purification and disinfection. Tailoring the morphology and size of photocatalysts has emerged as an effective strategy to enhance H_2O_2 generation by improving charge carrier dynamics and tuning band energetics. For instance, Li and co-workers developed an ultrathin 2D Al-MOF nanosheet of 1 nm (Al-P(AQ)) through the co-assembly of porphyrin (TCPP) as electron



donor and anthraquinone-based ligands (AQCA) as electron acceptor.¹⁸⁹ The resulting ultrathin framework significantly reduces the diffusion distance for photogenerated charge carriers, thereby facilitating rapid e⁻ and h⁺ transport to the catalyst surface and

improving photocatalytic efficiency. Moreover, incorporation of AQCA alters the electronic structure of the MOF, inducing a downward shift in the LUMO level, narrowing the band gap, and enhancing the thermodynamic driving force for the ORR.

Table 6: Summary of the representative of metal-organic framework (MOF) photocatalysts towards H₂O₂ photosynthesis

Sl. No	Catalyst	Reaction condition	Dosage (mg) & volume (mL)	H ₂ O ₂ Yield (μmol g ⁻¹ h ⁻¹)	AQY	SCC	Ref.
1.	EFB-MOF	H ₂ O and O ₂	5 mg & 30 mL	1676	1.03 @ 410 nm	-	181
2.	YTU-W-2	H ₂ O: EtOH (9:1)	10 mg & 50 mL	345	0.073@420 nm	-	182
3.	NH ₂ -MIL-125	H ₂ O and O ₂	15 mg & 50 mL	101	-	-	183
4.	MIL-125-NH ₂ ^a	H ₂ O/TEA and O ₂	5 mg & 20 mL	925.8	-	-	184
5.	SA-TCPP ^a	H ₂ O and O ₂	25 mg & 50 mL	0.66 mM h ⁻¹	14.9 % @ 420 nm	1.2 %	186
6.	UiO-67-PE/BB	H ₂ O: IPA (9:1)	10 mg & 50 mL	5141	4.24%@ 400 nm	-	187
7.	Al-P(20AQ)	H ₂ O and O ₂	0.5 g·L ⁻¹	163.2	4.8%@ 400 nm	0.11%	188

Light Irradiation: Xe lamp (λ>420 nm) except ^avisible light; BA= benzyl alcohol; TEA; triethanolamine

Porous organic polymers (POPs) based photocatalyst towards H₂O₂ Production:

Porous organic polymers (POPs) are a diverse class of materials known for their highly porous structures, which are constructed from organic monomers that primarily contain light elements such as C, H, O, N, B, etc.¹⁸⁹ POPs are primarily synthesised through the polymerisation of organic building blocks into macromolecular frameworks. POPs possess various properties that make them ideal for photocatalysis, such as high porosity, large surface areas, and tunable extended π-conjugated structures that enable broad visible-light absorption and efficient exciton generation. Their lightweight nature, excellent chemical/thermal stability, and pre-designable D-A building blocks facilitate superior charge separation, reduced recombination, and precise modulation of band gaps and redox potentials for targeted photocatalytic reactions. Unlike COFs, POPs can be synthesised under milder conditions, feature irreversible covalent bonds that impart greater robustness, and avoid harsh crystallisation steps. POPs can be further classified into two categories based on their long-range order, such as crystalline and amorphous POPs.¹⁹⁰ COFs and covalent triazine frameworks (CTFs) are well-known crystalline POPs, and some examples of amorphous POPs are porous aromatic frameworks (PAFs), hypercrosslinked polymers (HCPs), polymers of intrinsic microporosity (PIMs), and conjugated microporous polymers (CMPs), etc. The high crystallinity in a material can significantly promote electron/hole separation, reduce their possible recombination, and enhance the photocatalytic activity.^{191,192} Therefore, various reports could be seen regarding the development of crystalline POPs for the photosynthesis of H₂O₂, such as COF, as discussed above. CTF is also a crystalline POP, distinguished by its aromatic C-N linkage (triazine unit) and lack of weak bonds. Strong aromatic covalent connections mainly give CTFs

high nitrogen content and excellent chemical stability, which are valuable for various real-world uses and the intriguing heteroatom effect (HAE). Because of their unique qualities, CTFs are appealing for several uses, including energy storage, photocatalysis, heterogeneous catalysis, and gas separation and storage. CTFs may be divided into two groups based on the state of research: crystalline and amorphous CTFs. The kind of monomers and the synthesis procedure have a significant impact on the characteristics of CTFs. In recent years, significant research has been done on synthesis techniques such as aldehyde-amidine condensation, trifluoromethanesulfonic acid-catalysed synthesis, amino-aldehyde synthesis, and ionothermal polymerisation.^{193,194} CTFs are a promising candidate semiconductor in photocatalysis, including the photodegradation of organic pollutants, the conversion of chemical molecules, the splitting of water, the reduction of CO₂, and more, due to their abundance of nitrogen, strong conjugated structure, and absorption of visible light.^{195–197} By altering the phenyl and thiophene moieties, J. Byun and colleagues have synthesised two CTFs with the adjustable D-A character, demonstrating that regulating the oxidative reaction medium significantly affects photocatalytic H₂O₂ generation (**Figure 20a**).¹⁹⁸ The photocatalytic H₂O₂ generation ability of CTFs was assessed in both aqueous and non-aqueous conditions. The O₂ reduction process, in conjunction with toluene oxidation, is specifically made possible by CTF-Th, which has more thiophene donors. This results in a large generation of H₂O₂ up to 105 μmol, which is 4.7 and 2.5 times higher than that of H₂O (22.3 μmol) and H₂O/alcohol (42.4 μmol) oxidation, respectively (**Figure 20b**). According to the theoretical computation, benzaldehyde and H₂O₂ can be produced simultaneously on CTF surfaces due to the binding affinities of toluene and O₂, respectively. Toluene and water layers form a dual-phase system that makes it easy to separate the two very pure products. Inspired by the sequential energy- and charge-transfer processes from PS II to PS I in natural photosynthesis, K. A. I.



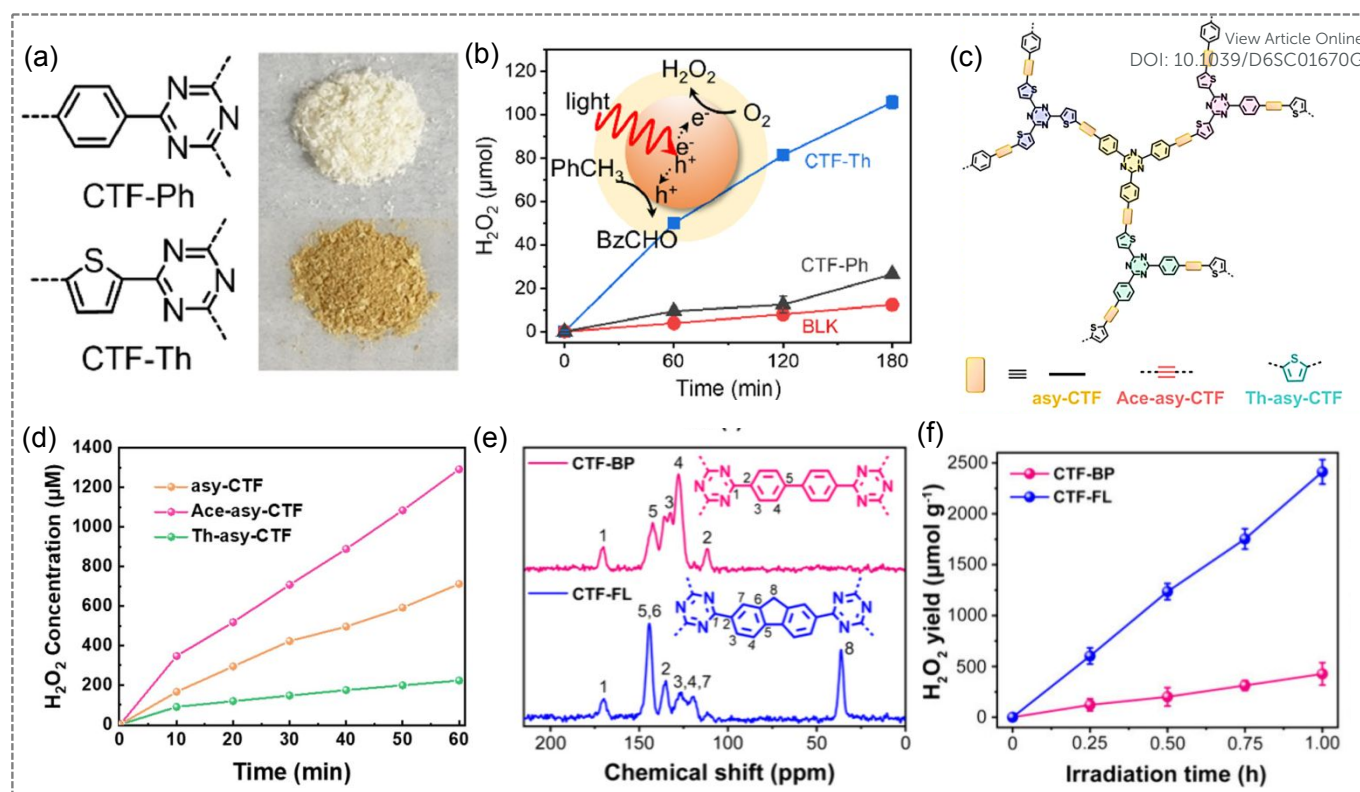


Figure 20: (a) Donor-acceptor type covalent triazine frameworks, CTF-Ph and CTF-Th, (b) Photocatalytic production of H₂O₂ in 50% toluene in acetonitrile under saturated O₂ conditions. (Reprinted with permission from Ref.¹⁹⁸ Copyright 2023 Elsevier). (c) Schematic illustration of the stepwise charge transfer within the CTF, (d) Time course of H₂O₂ evolution over CTFs (300 W xenon lamp with a 400 nm cutoff filter, light intensity: 100 mW cm⁻²). (Reprinted with permission from Ref.¹⁹⁹ Copyright 2024 American Chemical Society) (e) ¹³C CP-MAS NMR spectra of CTF-BP and CTF-FL, and (f) Time course of photocatalytic H₂O₂ production (λ > 420 nm, 300 W xenon lamp; 10 mg of catalyst in 100 mL of pure water; O₂-saturated, 25 °C). (Reprinted with permission from Ref.²⁰⁰ Copyright 2024 American Chemical Society).

Zhang and colleagues developed and synthesised three CTF photocatalysts with stepwise charge transfer (Figure 20c).¹⁹⁹ They created effective CTFs for high-efficiency photosynthesis of H₂O₂ from water and O₂ without the use of sacrificial agents by carefully designing linkers with different degrees of conjugation to act as electron transfer spacers and photocatalytic ORR centres between the four molecular donor-acceptor domains (M1-M4) in the asymmetric CTF framework. The acetylene moiety improved the spontaneous O₂ adsorption in the CTFs compared to the heavily conjugated thiophene moiety. Because Ace-asy-CTF's acetylene moiety effectively lowers the energy barrier for stepwise two-electron ORR, it has a higher photocatalytic H₂O₂ production efficiency than Th-asy-CTFs with strong conjugated thiophene units or asy-CTF without a spacer. This results in an enhanced photocatalytic H₂O₂ yield (2594 μmol g⁻¹ h⁻¹, Figure 20d) with an SCC of 0.48% without sacrificial agents. By creating and manufacturing two highly crystalline layered CTFs using 1,1'-biphenyl-4,4'-dicarbonitrile (BP-CN) and 9H-fluorene-2,7-dicarbonitrile (FL-CN) as the building blocks for the first time, Xu and colleagues created high-performance metal-free photocatalysts (Figure 20e).²⁰⁰ The direct photosynthesis of H₂O₂ generation on the as-prepared crystalline CTFs with a locked-in coplanar conformation has been significantly improved by utilising logical control of the torsion angle in the basal plane of the CTFs (Figure 20f). The exfoliated few-layer crystalline 2D

triazine polymer nanosheets from bulk CTF exhibit a remarkable SCC efficiency of 0.91% at a low catalyst concentration (0.5 g L⁻¹) and a noteworthy AQY of 16.8% at 420 nm, demonstrating an excellent photocatalytic H₂O₂ production rate up to 5007 μmol g⁻¹ h⁻¹ from oxygen and water without sacrificial agents. A series of CTFs with different numbers of acetylene groups were reported by H. Xu and colleagues as metal-free photocatalysts for the generation of H₂O₂. Acetylene or diacetylene moieties may be added to CTFs to increase photocatalytic H₂O₂ production significantly.²⁰¹ The integrated carbon-carbon triple bonds, which are crucial for adjusting the electrical structures of CTFs and preventing charge recombination, impart this natural improvement. Additionally, the acetylene and diacetylene moieties can drastically lower the energy required to generate OH*, opening up a novel two-electron oxidation route that produces H₂O₂. After 24 h, the H₂O₂ generation of CTF-BDBDN with two acetylene centres was greater than that of CTF-EDDBN with one acetylene moiety (39 μmol) and CTF-BPDCN without an acetylene moiety (21 μmol). Li and colleagues demonstrated how to increase the electrical conductivity of CTF by ten times for excellent, highly conductive carbon quantum dots (CQDs) as an electron transport medium inside the CTF pores.²⁰² In pure water without any sacrificial agent, the optimised CQD-CTF (0.5 wt%) shows a high H₂O₂ production rate up to 1036 μmol g⁻¹ h⁻¹ under visible light, 4.6 times that of CTF. According to this study, the presence of CQD will improve



the performance of charge separation and migration with higher electronic conductivity. The greater negative zeta potential, which can significantly trigger the ORR process, may also increase the affinity of H^+ . Additionally, photocatalysis increases the oxidation capacity, which benefits the WOR process. This work offers a novel approach to the practical H_2O_2 synthesis of low-conductivity organic semiconductors. Despite the challenges associated with amorphous POPs, such as low crystallinity, weak light absorption in the visible spectrum, poor separation of photogenerated carriers, and limited structural diversity, which hinder photocatalytic performance, there are only a few reports focusing on their development for photocatalytic H_2O_2 production. For instance, Nie et al. have reported the photocatalytic efficiency of four HCP photocatalysts with different arene monomers towards photocatalytic H_2O_2 production.²⁰³ A series of HCPs have been synthesised by facile Friedel Crafts alkylation reaction of different arene monomers, which include benzene (BE), diphenyl (DP), *p*-terphenyl (TP), and *p*-quaterphenyl (QP) (Figure 21a). Amongst all, HCP with QP group has the optimal separation and transfer efficiency of photogenerated e^-h^+ due to the higher degree of conjugation of the QP monomer. The efficiency of synthesised HCPs has been evaluated towards photocatalytic H_2O_2 production in acetonitrile and benzylamine under blue LED irradiation. The H_2O_2 production rate for BE, DP, TP, and QP was observed to be 6.0, 6.8, 7.8, and 9.3 $mmol\ g^{-1}\ h^{-1}$, respectively. Recently, Wang et al. have reported the synthesis of two alkynyl-containing POP (POP-DT and POP-DF) via Sonogashira cross-coupling reaction between acetylene-based monomer and thiophene or furan monomer (Figure 21b).²⁰⁴ The authors report that the acetylene moieties in the framework acted as the oxygen-reducing active site, while the thiophene or furan ring functioned as the electron donor unit. Further, the integration of acetylene and thiophene facilitated faster charge separation and improved charge transfer efficiency, thereby greatly enhancing the kinetic performance of the oxygen reduction reaction. Therefore, the H_2O_2

production rate of POP-DT, under visible light irradiation, reached $2422.2\ \mu mol\ g^{-1}\ h^{-1}$, which was 4.3 times higher than that of POP-DF, representing one of the best performances ever observed for polymeric photocatalysts. The coordination of the pyridine moiety with the acetylene-based monomer has also proved to be efficient for H_2O_2 photosynthesis. In this context, Wen et al have synthesised TEADP-POF by reacting tris(4-ethynylphenyl)amine (TEA) with 2,5-dibromopyridine (DP) and TEADB-POF with dibromobenzene.²⁰⁵ Triphenylamine functions as the electron-donating unit, while pyridine serves as the electron acceptor, enabling a push-pull effect within the 2D π -conjugated framework that facilitates charge separation and transfer. Consequently, a H_2O_2 production at a rate of $2136\ \mu mol\ g^{-1}\ h^{-1}$ was obtained with TEADB-POF from H_2O and O_2 . Similarly, the same group investigated photocatalytic H_2O_2 production in conjugated organic polymers through active-site position engineering. In this approach, 2,5-dibromopyridazine and 3,6-dibromopyridazine were employed in place of DP to synthesise TEAPYRA-COP and TEAPYRI-COP, respectively.²⁰⁶ TEAPYRI-COP, containing adjacent pyridazine nitrogen sites, exhibits stronger hydrogen-bonding with water compared to TEAPYRA-COP, where nitrogen atoms are positioned oppositely. This configuration facilitates O-H bond activation, enhances water oxidation to generate protons, and promotes efficient H_2O_2 formation via O_2 reduction. Additionally, the adjacent nitrogen sites in TEAPYRI-COP stabilise key intermediates through a low-energy six-membered transition state, improving the $2e^-$ ORR pathway. As a result, TEAPYRI-COP achieves a significantly higher H_2O_2 production rate ($2884\ \mu mol\ g^{-1}\ h^{-1}$), approximately 3.5 times greater than TEAPYRA-COP under visible light without additives.

In a study, Xhu et al. report the synthesis of TpMaTAE by multicomponent Schiff-base polycondensation of Tp-aldehyde, melamine (Ma), and 1,3,5-tris (4-aminophenyl) benzene (TAE).²⁰⁷ The reaction resulted in a covalently integrated acetylene donor with dual acceptors (triazine and carbonyl), and yields an amorphous,

Table 7: Summary of the representative Porous organic polymers (POPs) photocatalysts towards H_2O_2 photosynthesis.

Sl. No	Catalyst	Reaction condition	Dosage (mg) & volume (mL)	H_2O_2 Yield ($\mu mol\ g^{-1}\ h^{-1}$)	AQY	SCC (%)	Ref.
1.	CTF-Th	H_2O :IPA (9:1) and O_2	50 mg & 30 mL	43 μmol in 3 h	-	-	198
2.	Ace-asy-CTF	H_2O and O_2	5 mg & 10 mL	2594	4.4% @420 nm	0.48	199
3.	CTF-NSs	H_2O and O_2	10 mg & 100 mL	5007	16.8 % @420 nm	0.91	200
5.	0.5 CQD-CTF α	H_2O and O_2	5 mg & 20 mL	1036	1.03 % @420 nm	0.21	202
6.	QP-HCP	CH_3CN and BAm	10 mg & 20 mL	9300	-	-	203
7.	POP-DT	H_2O and O_2	10 mg & 50 mL	2422.2	2.67% @400 nm	-	204
8.	TEADP-POF	H_2O and O_2	30 mg & 50 mL	2136	2.39% @400 nm	-	205
9.	TEAPYRI-COP	H_2O and O_2	30 mg & 50 mL	2884	3.27% @400 nm	-	206
10.	TpMaTAE	H_2O and O_2	5 mg & 50 mL	6280	-	1.03	207
11.	CTF-BTT	H_2O /BA and O_2	5 mg & 50 mL	74956	7.61 % @420 nm	0.66	208
12.	CTF-DA-Film-3 α	H_2O and O_2	Thin Film	8920	1.242 % @450 nm	0.12	209
13.	BPYTEA-POF	H_2O and O_2	30 mg & 20 mL	3446	-	-	210

Light Irradiation: Xe lamp ($\lambda > 420\ nm$) except, ^avisible light IPA: isopropyl alcohol, BAm: Benzylamine



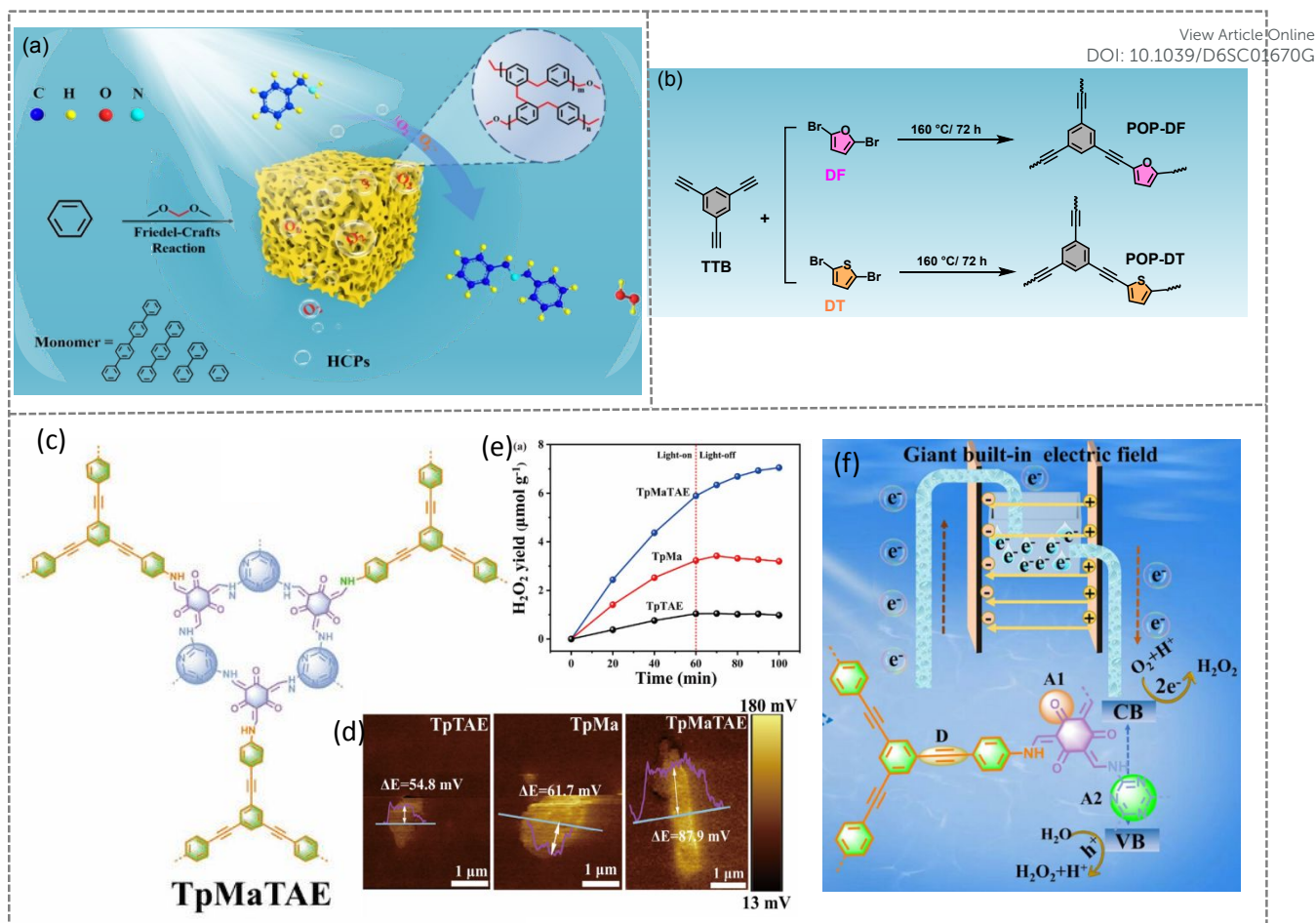


Figure 21: (a) Schematic illustration of the synthesis of different HCPs for benzylamine oxidation and H₂O₂ production. (Reprinted with permission from Ref.²⁰³ Copyright 2024 Wiley-VCH GmbH) (b) Schematic of the synthesis of POP-DT and POP-DF. (Reprinted with permission from Ref.²⁰⁴ Copyright 2024, Royal Society of Chemistry) (c) Structural representation of TpMaTAE. (d) Surface potential of TpMa, TpTAE, and TpMaTAE. (e) photocatalytic H₂O₂ production with TpMa, TpTAE, and TpMaTAE when light is on and off. (f) Mechanism for H₂O₂ production and built-in an electric field. Schematic of the synthesis of POP-DT and POP-DF. (Reprinted with permission from Ref.²⁰⁷ Copyright 2024 Wiley-VCH GmbH)

high-surface-area, fibrous COP with a strong built-in dipole and enhanced O₂ adsorption (Figure 21c). Band-structure analysis reveals visible-light absorption, suitable band edges for 2e⁻ ORR/WOR, and reduced exciton binding energy. Also, Kelvin probe force microscopy (KPFM) and surface charge measurements confirm a much stronger internal electric field than in D-A analogues TpTAE and TpMa (Figure 21d). Consequently, TpMaTAE achieves an H₂O₂ production rate of 5860 μmol g⁻¹ h⁻¹ from air and 7830 μmol g⁻¹ h⁻¹ (Figure 21e) under AM 1.5G with SCC 1.03% and 93.1% O₂ utilisation. Mechanistic analyses supported by experimental data reveal a stepwise single-electron 2e⁻ ORR via O₂⁻ and a one-step 2e⁻ WOR pathway (Figure 21f). Spectroscopy (fs-TAS, TRPL), together with EIS, OCVD, and light-induced EPR, shows that the D-A₁-A₂ architecture significantly improves exciton dissociation and reduces charge-transfer resistance. These measurements also reveal prolonged charge-carrier lifetimes and a higher density of stored electrons in TpMaTAE. In addition, in situ FTIR and dark H₂O₂ generation experiments confirm that the carbonyl groups function as electron reservoirs. This stored charge enables continued H₂O₂ formation even after the light is switched off.

Metal-organic polyhedra (MOP) based photocatalyst towards H₂O₂ production:

Metal-organic cages (MOC) or metal-organic polyhedra (MOP) are an old but rarely explored subclass of the AFPM.^{211,212} MOPs are attractive for their structural similarity to MOFs, except they have to cap terminal groups that prevent indefinite extension into networks, making them discrete molecules.²¹³ From the standpoint of the metal cation or cations and the organic linkers used in their self-assembly, MOP has demonstrated synthetic flexibility. The interior cavity, allowing guest molecules to be absorbed, is a distinguishing feature of these materials. Consequently, coordination cages have found utility in a wide range of applications, including molecular recognition and separation, host-guest chemistry, catalysis, and biological applications.^{214–217} In contrast to polymeric materials, MOP photocatalysts with well-defined active sites enable clear elucidation of structure-mechanism-performance relationships. Their photophysical properties can be precisely tuned through atomic-level modifications, leading to exceptional catalytic activity and attracting growing attention in recent years. MOPs are particularly



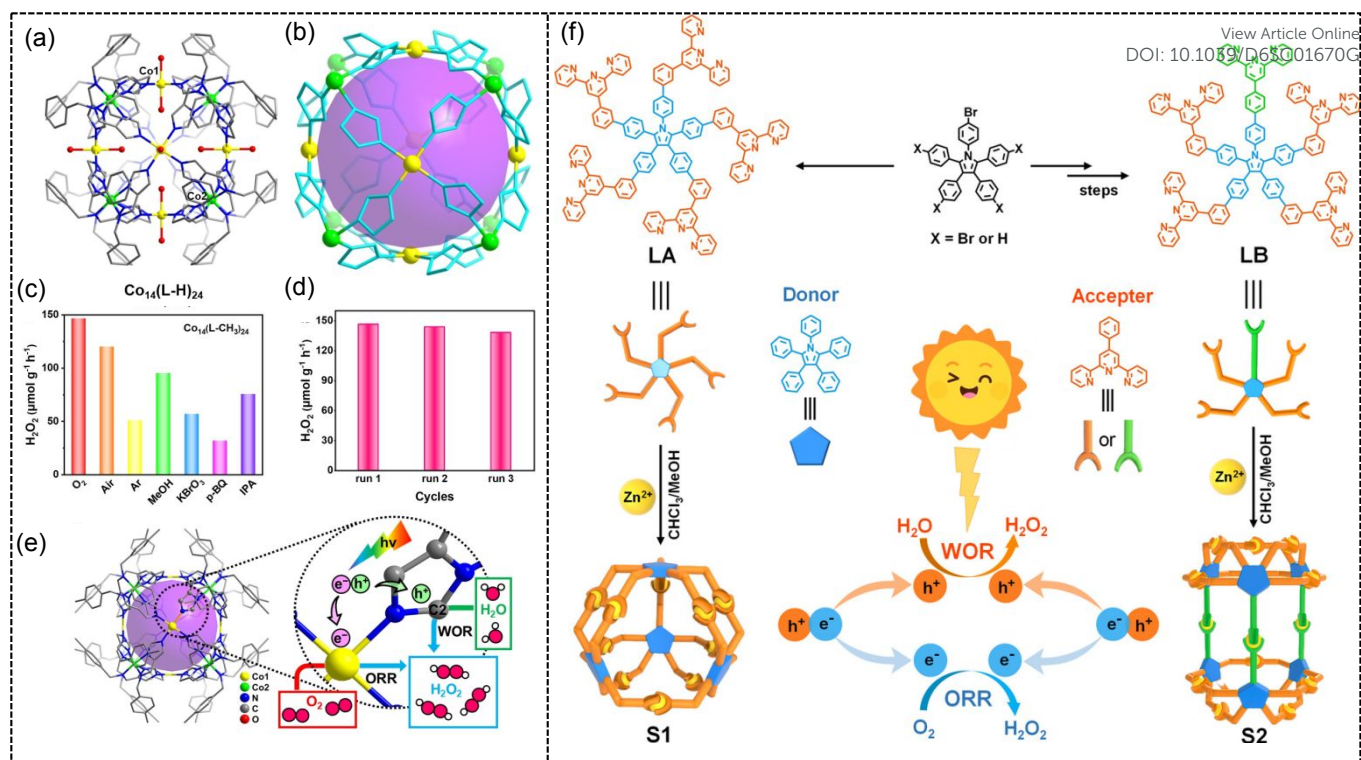


Figure 22: (a) Crystal structure of $(Co_{14}(L-H)_{24})$ (b) Polyhedral representation of $(Co_{14}(L-H)_{24})$ (c) Photocatalytic performances of H_2O_2 production by $Co_{14}(L-CH_3)_{24}$ in pure water and different atmospheres, and (d) Recyclability of $Co_{14}(L-CH_3)_{24}$ after photosynthesis of H_2O_2 . (e) Catalytic sites in $Co_{14}(L-CH_3)_{24}$ for ORR and OER (Reprinted with permission from ref.²¹⁸ Copyright 2023 Wiley-VCH GmbH) (f) Schematic representation for the synthesis of S1, S2, and their photocatalytic H_2O_2 production. (Reprinted with permission from Ref²¹⁹ Copyright 2025 Wiley-VCH GmbH)

advantageous due to their precisely controllable geometries, well-defined pore sizes, tunable electronic structures, and broad photoresponse windows. Furthermore, MLCT enhances the reactivity of the photoexcited states, while synergistic metal-ligand interactions promote efficient charge separation. Despite this, the photocatalytic applications of MOPs are less explored compared to other AFPMs. The first work with MOP towards photocatalytic H_2O_2 was reported in 2023, where Y. Q. Lan and co-workers reported two Co-MOCs ($Co_{14}(L-H)_{24}$ and $Co_{14}(L-CH_3)_{24}$) integrated with an imidazole-based ligand (Figure 22a-b).²¹⁸ The photocatalyst's light absorbance is enhanced, and the recombination efficiency of photogenerated electrons and holes is decreased due to MOC functionalization. According to theoretical simulations, the CH_3 functionalized ligand is better suited to adsorb the important $\cdot OH$ and $\cdot HOOH$ intermediates produced by WOR and ORR. $Co_{14}(L-CH_3)_{24}$ exhibits a higher H_2O_2 generation rate of $146.60 \mu mol g^{-1} h^{-1}$ in O_2 -saturated water, and subsequently, the MOP photocatalyst could produce a significant amount of H_2O_2 in different conditions such as air, MeOH and IPA (Figure 22c). The catalyst can be recycled up to three cycles with a nominal decrease in the yield (Figure 22d). Isotope tracing experiments and comparative studies show that for these two catalysts, the Co site acts as the reduction site, allowing the synthesis of H_2O_2 via the $2e^-$ two-step ORR route, while the imidazole site from the ligand acts as the oxidation site, producing H_2O_2 via the $2e^-$ two-step WOR pathway (Figure 22e). More significantly, in these Co(II)-based supramolecular cages, the imidazole site directly coordinates with the Co site, reducing the

spatial separation between the oxidation and reduction sites and increasing the charge migration efficiency, which in turn increases the catalytic activity of photocatalytic H_2O_2 synthesis. Similarly, Xiao et al present a novel supramolecular approach for photocatalytic H_2O_2 production using discrete, non-noble MOC, overcoming key limitations of conventional polymeric and framework-based photocatalysts.²¹⁹ Unlike MOFs or COFs, these cages offer atomic-level control over active sites, enabling direct correlation between structure, photophysical properties, and catalytic performance. Two Zn-based metallo-cages (S1 and S2) were rationally designed and synthesised with distinct electronic and photophysical properties (Figure 22f). The atomic-level control over active sites and charge-transfer pathways, with S2, exhibits high structural stability, low exciton binding energy, ultrafast intramolecular electron transfer, and prolonged excited-state lifetimes, all of which promote efficient charge separation. A bottom-up nanosizing strategy was further employed by dispersing MOC into DMF to generate ultrasmall, well-dispersed catalytic particles, significantly enhancing substrate accessibility and reaction kinetics. The photocatalytic H_2O_2 production was carried out in H_2O : DMF (9:1) solution using $Na_2C_2O_4$ as a sacrificial agent, and an exceptionally high H_2O_2 production rate of $77,401 \mu mol g^{-1} h^{-1}$ with a SCC efficiency of 0.97% was achieved. Mechanistic studies reveal that the cage architecture facilitates simultaneous $2e^-$ ORR and WOR pathways, while $Na_2C_2O_4$ suppresses charge recombination and provides a kinetically favourable route for superoxide radical formation, collectively overcoming ORR bottlenecks and enabling efficient and stable H_2O_2 production



Hydrogen-bonded organic framework (HOF) based photocatalyst towards H₂O₂ production:

Hydrogen-bonded organic frameworks (HOFs) are a class of porous crystalline materials formed by organic molecules linked through hydrogen bonding and other intermolecular forces.^{220,221} Although HOFs were proposed as porous materials in the 1990s, it was not until 2010 that their permanent porosity was confirmed through gas sorption studies.^{222,223} Most HOFs, constructed through weak intermolecular forces, generally exhibit lower stability compared to MOFs and COFs, which are built via coordination or covalent bonds. Nevertheless, the overall stability of HOFs can be significantly enhanced through synergistic effects of hydrogen bonding, π - π stacking, electrostatic interactions, and framework interpenetration.²²⁴ The π - π stacking interactions in HOFs not only enhance structural stability but also play a functional role in facilitating efficient electron transfer. As a result, HOFs have emerged as promising photocatalysts for various applications, including H₂-production²²⁵ and CO₂ reduction²²⁶. Recently, Zhong et al have reported the D-A HOF (TTF-Bpy-HOF) towards photocatalytic H₂O₂ production from H₂O and O₂ by reacting electron-rich tetrathiafulvalene tetracarboxylic acid (TTF) and electron-deficient 4,4'-bipyridine (Bpy) as the electron-accepting unit (Figure 23a-b).²²⁷

TTF-Bpy-HOF demonstrated a significantly enhanced photocatalytic performance, achieving a maximum H₂O₂ production rate of 681.2 $\mu\text{mol g}^{-1} \text{h}^{-1}$ (Figure 23c). In contrast, the Bpy-free counterpart, TTF-HOF, exhibited much lower efficiency, with a production rate of only 74.4 $\mu\text{mol g}^{-1} \text{h}^{-1}$. The HOF demonstrated excellent recyclability, retaining its photocatalytic efficiency over 10 consecutive cycles, showcasing its structural integrity over prolonged H₂O₂ production. The photodecomposition of H₂O₂ over TTF-HOF and TTF-Bpy-HOF was evaluated under light irradiation. The H₂O₂ concentration remained essentially unchanged over 2 h, confirming its stability in the presence of these materials under illumination. Mechanistic studies reveal that H₂O₂ formation in the HOF system proceeds via both the 2e⁻ ORR and WOR pathways. As illustrated in Figure 23d, under visible-light irradiation, the TTF units in TTF-Bpy-HOF absorb photons, generating separated electron-hole pairs. The photogenerated electrons migrate to the Bpy moieties, while holes remain on the TTF units, enabling spatially separated redox reactions. Water oxidation proceeds on the TTF units via a direct 2e⁻ pathway to produce H₂O₂, whereas O₂ reduction occurs on the Bpy units through a two-step 2e⁻ process involving $\cdot\text{O}_2^-$ intermediates, ultimately yielding H₂O₂.

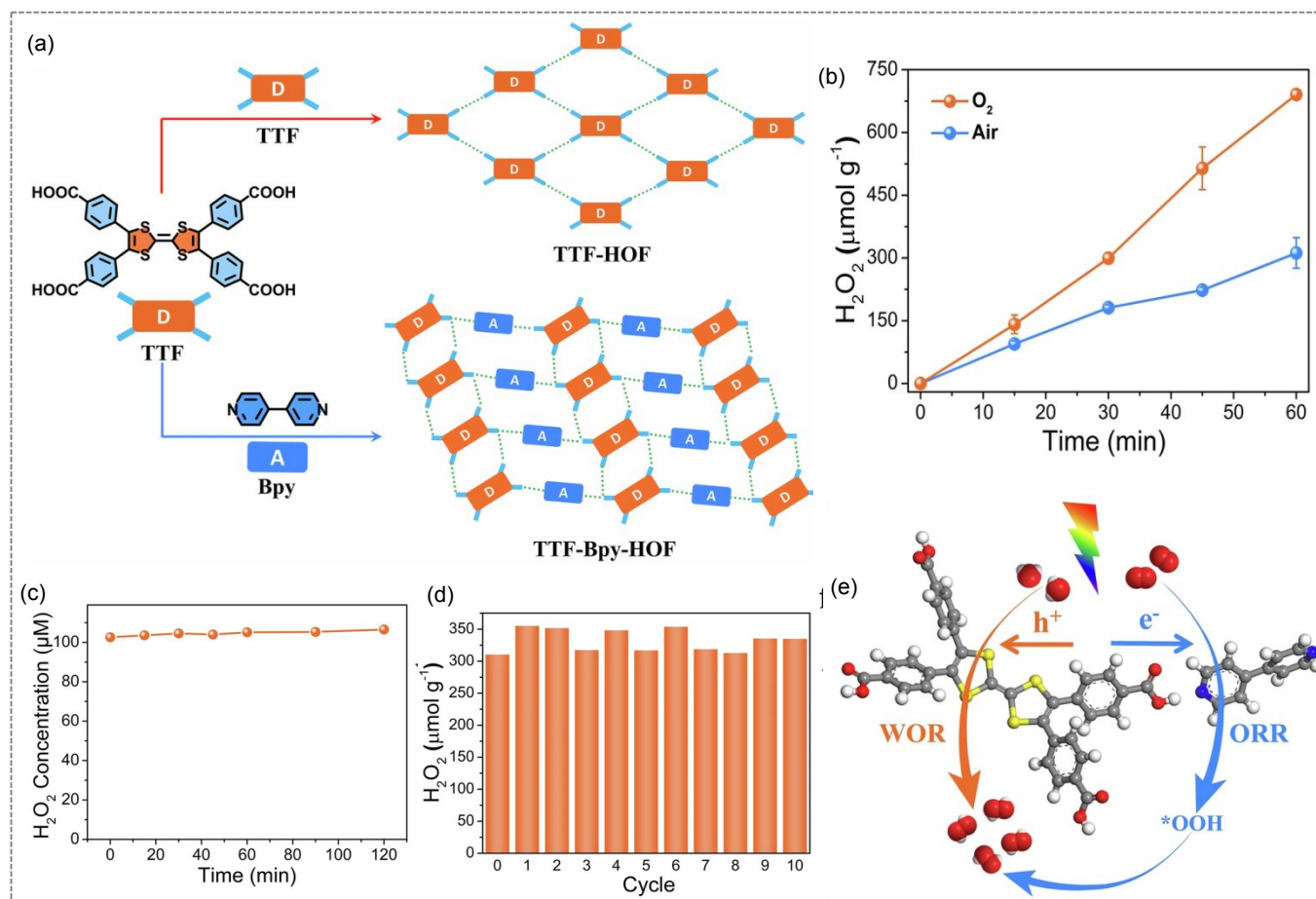


Figure 23: (a) Schematic representation of D-A HOF. (b) Time-dependent production of H₂O₂ by TTF-Bpy-HOF in O₂ and air-saturated solution (c) H₂O₂ decomposition study by TTF-Bpy-HOF in reaction medium (d) Recycle experiments of TTF-Bpy-HOF for H₂O₂ photosynthesis over 10 cycles. (e) Schematic diagram of the photosynthesised H₂O₂ through the ORR and WOR pathways (Reprinted with permission from Ref.²²⁷ Copyright 2025, Springer Nature.)



AFPM-based composites for photocatalytic H₂O₂ production:

One of the key advantages of functional porous materials is the vast potential for post-synthetic modification (PSM), thanks to their rigid framework and large surface area.²²⁸ Functionality that cannot be directly incorporated into functional porous materials during de novo synthesis can be introduced through post-synthetic modification (PSM) strategies. In the case of COF, there are current strategies for the PSM COF involve (i) incorporation of a variety of active metal species by using metal complexation through coordination chemistry, (ii) covalent bond formation between existing pendant groups and incoming constituents and (iii) chemical conversion of linkages. (iv) A monomer truncation strategy for the internal functionalization of COFs sometimes assists post-synthetic modification. Current strategies for post-synthetic modification (PSM) of COFs include (i) encapsulation of various active species without covalent threading, (ii) formation of covalent bonds between functional groups of COF and active species, (iii) chemical conversion of linkages into desired active sites and (iv) the use of a monomer truncation strategy to assist in the functionalization of COFs. In PSM, COF can be utilised as a host or template to encapsulate or wrap other substances, such as metal nanoparticles, organic molecules, or other porous materials and the material synthesised is generally referred to as COF-composites. These composites leverage the unique properties of COFs while enhancing functionality by including complementary substances. The resulting COF composites often exhibit synergistic properties beneficial for

desired applications.²²⁸ Cong et al. have reported the synthesis of two novel polyimide COF (MPa-COFs/CQDs and MNA-COFs/CQDs) composites using a different type of dianhydride and carbon quantum dots (CQDs) via a one-pot hydrothermal method.²³⁰ The CQDs on COFs were loaded by treating the synthesised COF with D (+) glucose and heating it in a Teflon-lined stainless-steel autoclave at 160 °C for 3 h. After the introduction of CQDs, both photocatalytic and electronic properties of polyimide COFs were boosted, and suppression of photoinduced electrons and holes recombination was also noticed. The photocatalytic activity of two COF composites towards H₂O₂ production was evaluated using pure water and O₂ under visible light irradiation, and the highest production yield up to 540 μmol g⁻¹ h⁻¹ was observed for MPa-COFs/CQDs-2. The synthesis of the COF composite with the desired heterojunction has also been a topic of interest for many researchers. As organic semiconductors, COFs can be combined with suitable inorganic semiconductors to form various types of heterojunctions, significantly enhancing redox capacity regarding thermodynamics and kinetics.²³¹ In that context, Wong et al. have combined the D-A conjugated TpMA-COF with inorganic semiconductor CdS by the hydrothermal method and report the formation of S-scheme heterojunctions.²³² The formation of the heterojunction enhanced the photocatalytic activity of the composites. To optimise the catalyst, various amounts of CdS were loaded onto the COF, with the resulting catalysts being named CT-5, CT-10, CT-15, CT-20, and CT-30. The photocatalytic activity of the COF composite material towards H₂O₂ production was evaluated using pure water simulated sunlight. The H₂O₂ production yield of CT-10 was found to be the highest, with a production rate of up to 608.41

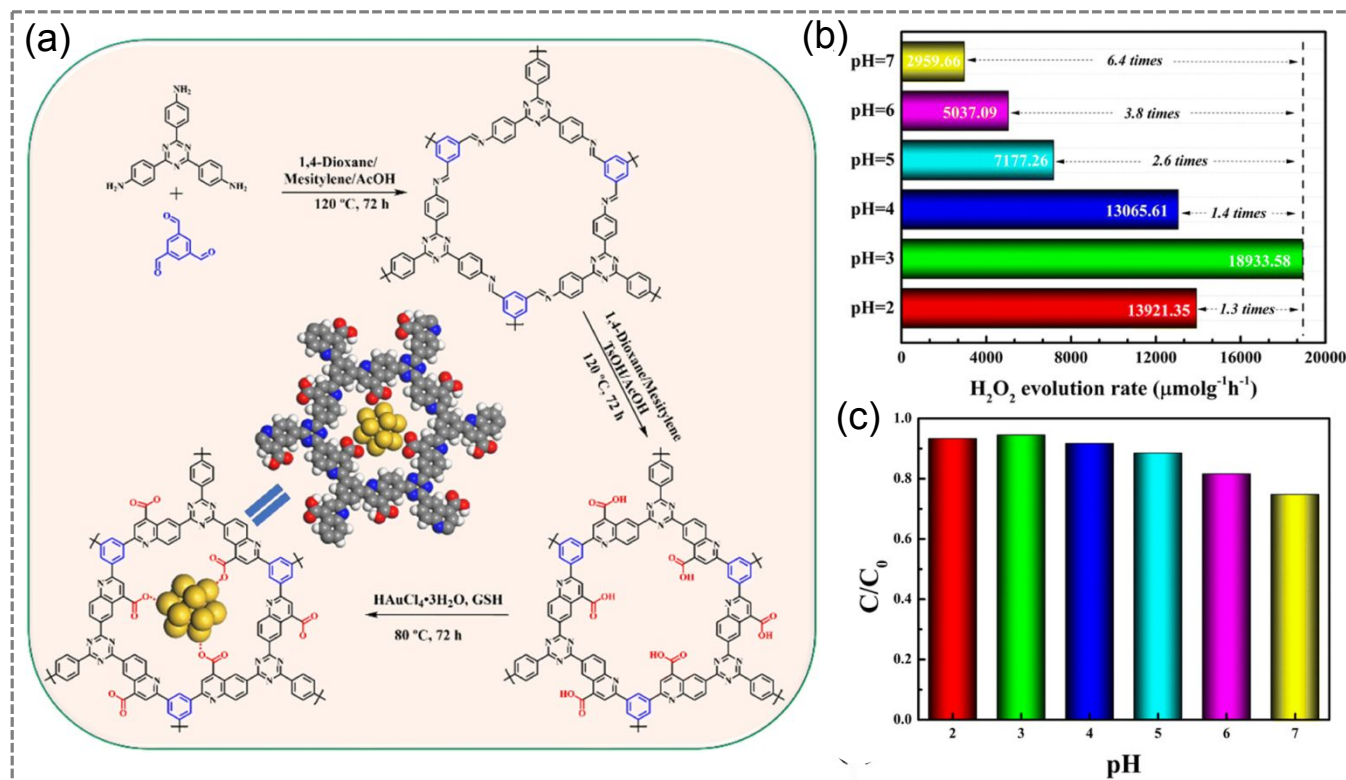


Figure 24: (a) Synthetic route for covalently treated Au@COF composite. (b) Photocatalytic H₂O₂ production of Au@COF at different pH. (c) The photocatalytic decomposition of H₂O₂ (200 mM) over Au@COF at different pH. (Reprinted with permission from Ref.²²⁹ Copyright 2023, Royal Society of Chemistry).



$\mu\text{mol L}^{-1}$ in 90 min. Similar work has also been reported by Xia et al. by constructing the heterojunction on TpPa-1 COF through the incorporation of ZnIn_2S_4 nanosheets on COF.²³³ The COF composite, $\text{ZnIn}_2\text{S}_4/\text{TpPa-1}$, with a hierarchical heterostructure, could produce H_2O_2 at a rate of $516 \mu\text{mol L}^{-1}$ under visible light irradiation, which is almost three times higher than individual COF and ZnIn_2S_4 catalysts. In a quest to synthesise COF composite with improved photocatalytic activity, et al. have incorporated tungsten oxide (WO_3) into Tp-TAPB-COF and report the formation of $\text{WO}_3/\text{Tp-TAPB}$ composite bearing Z-scheme heterojunction.²³⁴ The Z-scheme heterojunction has promoted the separation of useful e^-h^+ pairs, and overall composites have enhanced light absorption properties. To get the optimum catalyst, the amount of WO_3 was varied from 5mg to 40 mg and named as $\text{XWO}_3/\text{Tp-TAPB}$, where $X = 10, 20, 30,$ and 40 , respectively. The photocatalytic activity of different COF composites was evaluated in pure water and oxygen irradiating LED light with a wavelength $> 420 \text{ nm}$. Amongst all the catalytic activity of $20\text{WO}_3/\text{Tp-TAPB}$ was found to be optimum towards light-driven H_2O_2 production with a rate of $1488.4 \mu\text{mol h}^{-1} \text{g}^{-1}$. Towards the PSM of COF and encapsulation of metal nanocrystals (NCs), Shang et al. have

reported a novel strategy by generating anchoring sites within the framework of COF that bind targeted NCs.²²⁹ To achieve this, TAPB-COF was first synthesised solvothermally and then decorated with carbonyl groups using the well-known Doebner-Miller reaction (Figure 24a). The carbonyl groups acted as anchoring sites, and upon treatment of the functionalised COF with $\text{HAuCl}_4 \cdot 3\text{H}_2\text{O}$, gold NCs (Au NCs) were incorporated into the pores of the COF (Figure 24a). Additionally, the carbonyl groups within the COF served as a bridge. The Au NCs incorporated into the COF framework enhanced charge transfer and catalytic activity, while the COF provided structural stability and a high surface area for efficient H_2O_2 production. The Au modified COF (Au@COF) has shown the photocatalytic H_2O_2 production rate of $18933.58 \mu\text{mol g}^{-1} \text{h}^{-1}$ at $\text{pH} = 3$ (Figure 24b). Also, the decomposition rate of H_2O_2 over Au@COF was merely 5.5% at $\text{pH} = 3$, which was lower than that at $\text{pH} = 7$ (35.2%) (Figure 24c). The PSM of porous materials often uses toxic reagents or metal catalysts under harsh conditions, risking framework instability, metal contamination, and environmental hazards. Recently, Xu et al have reported an eco-friendly route for PSM of COF through an enzymatic reaction²³⁵. Through horseradish peroxidase (HRP)-catalysed click

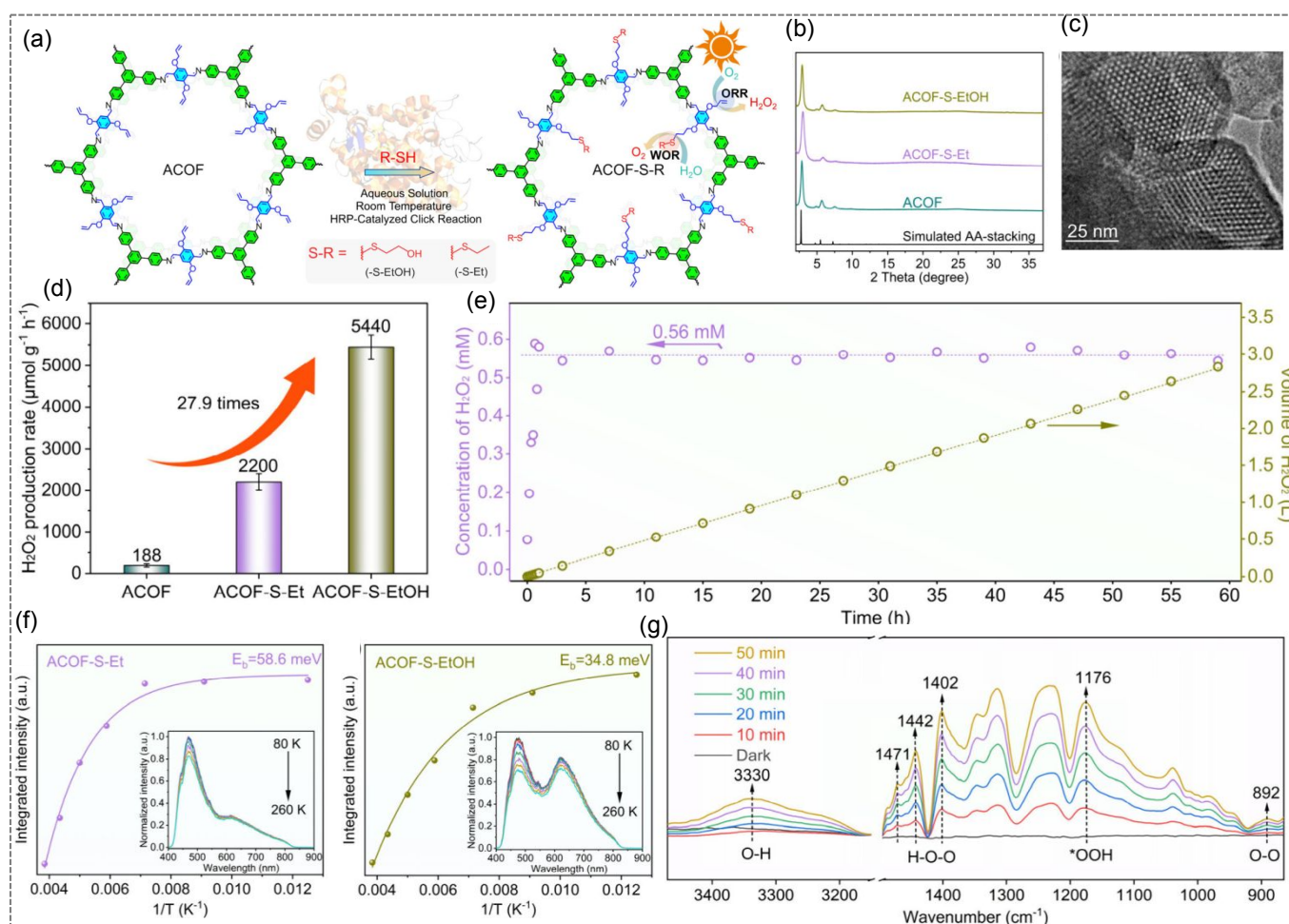
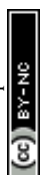


Figure 25: (a) Schematic route for PSM of ACOF through enzymatic click reaction. (b) PXRD of pristine & modified ACOFs. (c) HRTEM of ACOF-S-EtOH. (d) Comparative H_2O_2 production efficiency of pristine & modified ACOFs. (e) Long-term photocatalytic H_2O_2 production through continuous flow catalysis. (f) Integrated PL emission intensity as a function of temperature for ACOF-S-ET and ACOF-S-Et. In situ DRIFTS spectra of the photocatalytic H_2O_2 production on ACOF-S-EtOH. (g) In situ DRIFTS spectra of ACOF-S-EtOH during photocatalytic H_2O_2 production (Reprinted with permission from Ref.²³⁵ Copyright 2025, American Chemical Society).



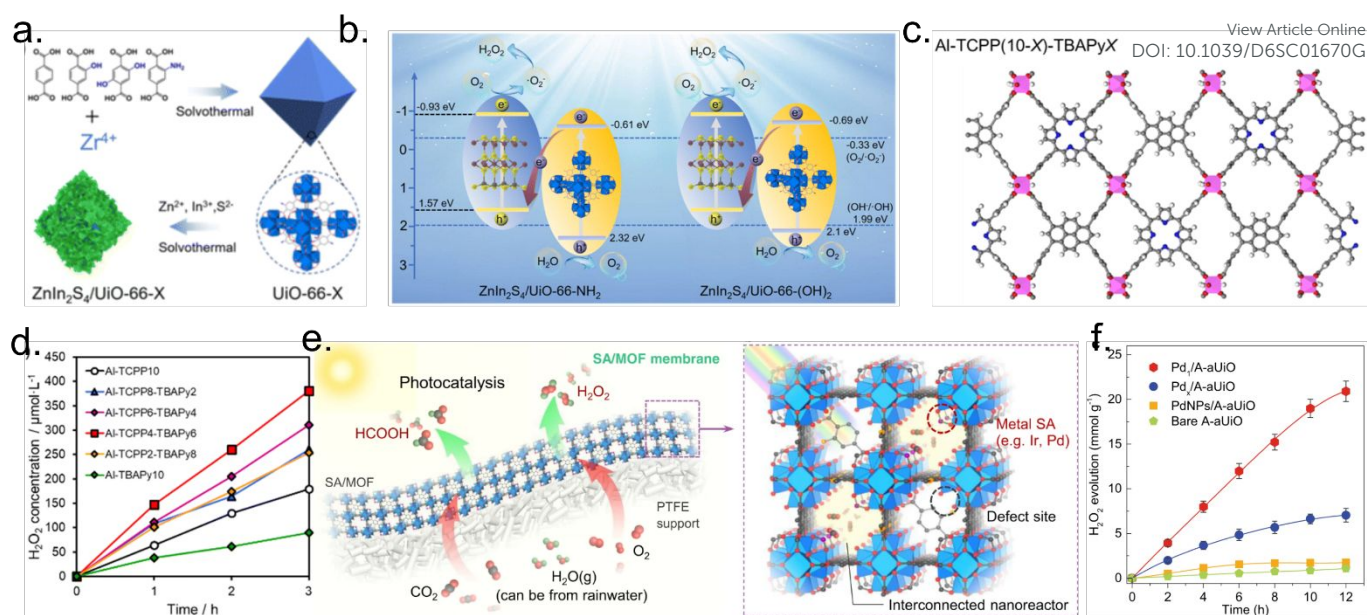


Figure 26: (a) Preparation diagram of ZnIn₂S₄/UiO-66-X hybrids, (b) the proposed mechanism for photocatalytic H₂O₂ evolution using Z-UN and Z-U(OH)₂,²⁴² (c) Schematics of Al-TCPP(10-X)-TBAPyX, (d) Comparison of photocatalytic H₂O₂ production over Al-TCPP(10-X)-TBAPyX samples,²⁴³ (e) Humidified gases (e.g., CO₂, O₂) can be fed through the gas-permeable MOF/PTFE membranes and photocatalytically reduced to value-added chemicals (e.g., HCOOH and H₂O₂) under visible light irradiation and ambient conditions and with controllable defect-engineering, specific metal SAs (e.g., Ir and Pd) can be precisely anchored on the edges of the Zr₆O₄(OH)₄(-CO₂)_{12-x} octahedral to act as programable catalytic centers for catalyzing different reactions, such as photocatalytic CO₂-to-HCOOH and O₂-to-H₂O₂ conversion. The open and interconnected MOF pores serve as the nanoreactors facilitating the diffusion and conversion of gas reactants, and (f) Time course of H₂O₂ generation on pristine A-aUiO and PdNPs, Pd_x, and Pd₁ decorated A-aUiO catalysts. (Reprinted with permission from Ref.²⁴⁵ Copyright 2023, Springer Nature

reactions, 2-hydroxyethylthio (-S-EtOH) and ethylthio (-S-Et) groups were covalently introduced into the COF pores under mild aqueous conditions (Figure 25a). The modified COFs (ACOF-S-EtOH and ACOF-S-Et) retained their crystallinity relative to the pristine COF, as confirmed by PXRD (Figure 25b) and HRTEM (Figure 25c). After the introduction of the functional group, the H₂O₂ production was escalated up to 27.9 times, reaching a maximum production rate of 5440 μmol g⁻¹ h⁻¹ with COF-S-EtOH from H₂O and O₂ (Figure 25d). Interestingly, the thermally modified sample showed a lower H₂O₂ production rate than the enzymatically modified route, confirming the advantage of the enzymatic PSM method. Further, a continuous-flow photocatalytic reactor packed with ACOF-S-EtOH (Figs. 3d, S24) sustained a steady H₂O₂ concentration of 0.56 mM over 58 h, achieving a cumulative output of 2.5 L (Figure 25e). The enhanced polarity after PSM has been verified through temperature-dependent photoluminescence (PL) studies. The altered PL emission of COFs was attributed to aggregation effects and enhanced charge polarisation induced by functionalization. Further, the exciton binding energies (*E_b*) derived from Arrhenius fitting were observed to be 68.4 meV (ACOF), 58.6 meV (ACOF-S-Et), and 34.8 meV (ACOF-S-EtOH) (Figure 25f). The significantly lower *E_b* of ACOF-S-EtOH indicates more efficient electron-hole separation, explaining its superior photocatalytic performance. Mechanistic investigation highlights the formation of H₂O₂ via both ORR and WOR pathways. In situ DRIFTS further verified the •OOH intermediate by the intensified

peak at 1176 cm⁻¹ (Figure 25g). The growing band at 892 cm⁻¹ indicated O₂ adsorption on ACOF-S-EtOH, while increased signals at 3330 cm⁻¹ (O-H stretching) and 1402, 1442, and 1471 cm⁻¹ (H-O-O bending) confirmed the formation and accumulation of H₂O₂. Similar to COF, the ubiquitous opportunity of MOF materials for PSM has been widely explored, especially for electrocatalytic applications.²³⁶⁻²³⁹ Due to their distinctive advantages, MOF-based materials have become promising electrocatalysts for the 2e⁻ ORR in H₂O₂ generation.^{240,241} Accordingly, MOF composites, pure MOF, and bimetallic MOF demonstrated a promising material for photocatalytic H₂O₂ generation. Yao and the team recently synthesised several ZnIn₂S₄/UiO-66-X (X = H, OH, (OH)₂, and NH₂) and discovered that amino or hydroxyl functionalisation may activate the effective photocatalytic production of H₂O₂ under visible light (Figure 26a).²⁴² The H₂O₂ yields for ZnIn₂S₄/UiO-66-NH₂, ZnIn₂S₄/UiO-66-(OH)₂, and ZnIn₂S₄/UiO-66-OH are 799, 733, and 165 μmol L⁻¹, respectively, whereas the yield for ZnIn₂S₄/UiO-66 is just 84 μmol L⁻¹ (without a sacrificial agent, in ambient air, indirect ORR). The enhanced visible-light absorption and Z-scheme heterojunctions of ZnIn₂S₄/UiO-66-NH₂ and ZnIn₂S₄/UiO-66-(OH)₂ led to their significant H₂O₂ generation (Figure 26b). The Yamashita research group synthesised an Al-MOF utilising mixed ligands of 1,3,6,8-tetrakis(*p*-benzoic acid) pyrene and tetrakis(4-carboxyphenyl) porphyrin for photocatalytic H₂O₂ generation under visible light (Figure 26c).²⁴³ Al-MOFs have the capacity to inhibit the breakdown of H₂O₂ and have

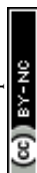


Table 8: Summary of the representative AFPM-based composites for photocatalytic H₂O₂ production.View Article Online
DOI: 10.1039/D6SC01670G

Sl. No	Catalyst	Reaction condition	Dosage (mg) & volume (mL)	H ₂ O ₂ Yield (μmol g ⁻¹ h ⁻¹)	AQY	SCC	Ref
1.	Au@COF	H ₂ O: BA (4:1), O ₂	5 mg & 50 mL	18933.58 ^a	-	-	229
2.	MPa-COFs/CQDs-2	H ₂ O and O ₂	20 mg & 100 mL	540	13.27% @ 400 nm	0.8%	230
3.	CdS/TpMA	H ₂ O and O ₂	20 mg & 50 mL	511.54 μmol L ⁻¹ h ⁻¹	-	-	232
4.	ZnIn ₂ S ₄ /TpPa-1	H ₂ O, EtOH and O ₂	20 mg & 40 mL	516 μmol L ⁻¹	-	-	233
5.	WO ₃ /Tp-TAPB	H ₂ O and O ₂	5 mg & 10 mL	1488.4 ^b	1.22% @ 420 nm	-	234
6.	ZnIn ₂ S ₄ /UiO-66-NH ₂ ^c	H ₂ O and Air	20 mg & 40 mL	799	-	-	242
7.	Al-TCPP (10-X)-TBAPyX	H ₂ O and O ₂	5 mg & 5 mL	127	-	-	243
8.	Al-MIL-101-NH ₂	H ₂ O and O ₂	5 mg & 5 mL	295	-	-	244
9.	Pd ₁ /A-aUiO	H ₂ O and O ₂	Membrane based	1.74 mmol g _{cat} ⁻¹ h ⁻¹	-	-	245
10.	COF@H ₃ PO ₄	H ₂ O and O ₂	10 mg & 20 mL	5214	-	0.69%	247
11.	Fe SAS-TpPP-COF	H ₂ O: BA (9:1), O ₂	5 mg & 50 mL	4130	6.4% @ 420 nm	0.20%	248

introduced a novel pathway for the generation of H₂O₂ utilising ¹O₂ as intermediates.²⁴⁴ The production of H₂O₂ *via* both the ORR (¹O₂ + 2H⁺ + 2e⁻ → H₂O₂) and WOR (¹O₂ + 2H₂O → 2H₂O₂) utilizing ¹O₂ was deduced. Wang et al. deposited Pd single atoms over faulty UiO-66-NH₂ and then fabricated gas-permeable Pd/UiO-66-NH₂ membranes for photocatalytic H₂O₂ production from humid O₂ at gas-solid interfaces.²⁴⁵ The positively charged Pd single atoms can enhance H₂O₂ generation and simultaneously impede H₂O₂ breakdown, as shown in the prior work.²⁴⁶ The defect sites facilitated light absorption and interaction with metal single atoms, whereas the UiO-66-NH₂ molecular structure functioned as several linked non-reactors. A notable H₂O₂ production rate of 10.4 mmol g⁻¹ h⁻¹ was achieved using Pd/UiO-66-NH₂ membranes in a gas-membrane-gas configuration, which is 4.9 times more than that produced with Pd/UiO-66-NH₂ particles in a particle-in-solution setup (utilising visible light, isopropanol as a sacrificial agent, and pure O₂ for the ORR) (Figure 26f).

Conclusion and future perspective:

In recent years, H₂O₂ has received gradually increasing attention, and it is recognised not only as an efficient oxidant in various fields but also as a prospective energy carrier. The photosynthesis of H₂O₂ over AFPM has attracted growing interest, and efforts are being made to regulate the efficiency of AFPM-based photocatalysts to achieve remarkable H₂O₂ production performance. In this review, we have elaborated on the recent strategies applied to increase the efficiency of various AFPM-based photocatalysts for H₂O₂ photosynthesis. More importantly, the modification strategies reported thus far for achieving improved photocatalytic H₂O₂ production performance over AFPM-based photocatalysts have been comprehensively summarised and discussed. Most of the reported articles have tried to understand the effect of linkage modification, heteroatom doping,

topology and structural modification, functional group incorporation, post-synthetic modification, etc, towards improving the D-A property, enhanced charge separation, and effect on band gap. The active site for H₂O₂ production has been meticulously studied in metal and metal-free AFPM using experimental and computational techniques. This has further enabled the better design of materials for practical implementation. Similarly, the range of applications has expanded, offering possibilities for photocatalytic H₂O₂ production that is efficient but also selective and recyclable for multiple cycles. The capability to adjust functionality in metal-free AFPMs has further provided an opportunity to tune band positions for efficient H₂O₂ production. The synthesis of composites using AFPMs has also showcased its photocatalytic efficiency by creating heterojunctions appropriate for photocatalytic H₂O₂ production. Though tremendous research is going on to improve the photocatalytic production of H₂O₂, there are still several challenges that need to be addressed to translate the potential of materials from laboratory to practical, real-world applications (Figure 27). This involves tackling the following aspects:

(i) **AFPM diversification with Hierarchical Porosity:** Among the various types of metal-free AFPM materials, there are numerous reports on COFs, while other AFPM materials have received less attention. Although COFs offer an ordered structure and larger surface area than other organic frameworks like POPs and CTFs, more detailed research on other AFPMs to enhance photocatalytic activity would be beneficial. The photocatalytic performance is strongly dependent on the crystallinity of COFs; however, crystallinity can deteriorate over time during long-term catalytic operation. Therefore, the development of porous materials that can sustain high photocatalytic performance independent of long-range crystalline order, while effectively leveraging porous architectures, is highly desirable. In this regard, the development of porous material-based aerogels for H₂O₂ photosynthesis represents a promising



breakthrough, as such systems can exploit hierarchical macro-mesoporosity to enhance mass transport and catalytic efficiency.

(ii) **ORR-WOR Engineering:** The rational design of porous materials for photocatalytic H₂O₂ production must be tailored to the targeted reaction pathway: ORR or WOR, as each imposes distinct electronic and structural requirements. After photoinduced electron-hole separation in a photocatalyst, the ORR proceeds via the excited electrons, while the WOR is driven by the photogenerated holes. The electron-deficient moieties like triazine, benzothiadiazole, cyano, groups function as ORR-active centres for efficient 2e⁻ ORR, while electron-rich sulfur-containing units such as pyrene, thiophene, and triaryl amines proved to be effective WOR-active sites for 2e⁻ WOR. COFs, with tunable π -conjugation and ordered porosity, are well suited for ORR-driven H₂O₂ generation through D-A engineering, band-edge alignment toward the O₂/H₂O₂ potential, and pore environments that enhance O₂ diffusion and H₂O₂ desorption while suppressing the 4e⁻ pathway. POPs, owing to their high chemical and oxidative stability, are particularly promising for WOR-driven H₂O₂ production, where functionalisable backbones and hydrophilic pores facilitate water adsorption, intermediate stabilisation, and proton-coupled electron transfer. MOFs offer site-isolated metal nodes (Zn, Zr, or single-site Fe/Co under controlled coordination) and modular coordination environments, enabling selective ORR via weak O-O activation or WOR through stable water-oxidation centres, provided oxidative robustness is ensured. MOPs and HOFs with an appropriate D-A site have shown H₂O₂ production through the simultaneous ORR-WOR pathway.

(iii) **NIR Photocatalysis:** The most practical and sustainable route for H₂O₂ synthesis relies on solar energy; however, nearly 53% of the solar spectrum lies in the near-infrared (NIR, $\lambda > 760$ nm) region. In contrast, photocatalytic H₂O₂ production over AFPM-based catalysts remains largely restricted to visible-light excitation ($\lambda < 760$ nm). To date, only a handful of studies have focused on the rational design of NIR-responsive catalysts, highlighting a significant research gap. Therefore, greater emphasis should be placed on the development of NIR-active porous photocatalysts to more effectively utilise the full solar spectrum. Furthermore, as AQY and SCC are key metrics for evaluating photocatalytic performance, improving photoefficiency should not be overlooked. The highest AQY of 22.78%, 14.9%, and 16.8% has been reported for COF, MOF, and CTF, respectively, at ~ 420 nm. Similarly, SCCs of 1.41%, 0.91%, and 1.2% were reported for COF, MOF, and CTF under artificial sunlight simulation. While SCC values above 1.0% have been reported under laboratory conditions, these are typically achieved through extensive parameter

(iv) optimisation rather than intrinsic catalyst efficiency. Under natural sunlight, the SCC efficiencies of photocatalysts for H₂O₂ production remain well below the $\sim 0.10\%$ efficiency of natural photosynthesis, posing a major barrier to industrial application.

(v) **Facile and scalable synthetic route:** From the viewpoint of practical photocatalytic H₂O₂ production, the scalability and facile synthesis of AFPM-based materials are of paramount importance. Although these materials have demonstrated impressive activity and selectivity toward the 2e⁻ ORR, most reported synthetic strategies remain complex, low-yielding, and difficult to translate to large-scale

manufacturing. Future efforts should therefore focus on developing cost-effective, environmentally benign, and scalable fabrication routes, while maintaining precise control over active sites and electronic structures. Further achieving batch-to-batch uniformity and reproducibility remains a key challenge for the commercialisation of porous materials. Therefore, the development of well-controlled and scalable synthetic routes, such as melt polymerisation and continuous-flow COF synthesis, to enable reliable bulk production is necessary. Addressing these challenges will be essential for advancing AFPM-based photocatalysts from laboratory studies toward industrially viable H₂O₂ production technologies.

(vi) **Artificial intelligence (AI) and machine learning (ML) guided photocatalytic screening:** AI and ML provide transformative high-throughput strategies for the discovery of efficient COF-based photocatalysts for H₂O₂ production. By learning structure-property-performance relationships from existing experimental and computational datasets, ML models should be employed to rapidly predict key descriptors such as band-edge alignment, charge-carrier separation efficiency, pore polarity, and adsorption energies of ORR intermediates (*OOH, H₂O₂). These data-driven predictions enable virtual screening of vast COF chemical spaces, significantly reducing reliance on trial-and-error synthesis. Coupled with automated synthesis and high-throughput photocatalytic evaluation, AI-guided frameworks can iteratively optimise COF architectures to selectively promote the 2e⁻ ORR pathway while suppressing competing reactions. Such AI-assisted discovery platforms are expected to accelerate the development of high-performance, solar-driven COF photocatalysts with improved AQY and SCC values. Further, the integration of AI/ML automation and robotics into COF synthesis can also offer a powerful approach for rapidly screening reaction parameters and discovering new chemistries, thereby accelerating the transition of porous material from laboratory-scale materials to industrially viable platforms.

(vii) **Decentralised H₂O₂ production and industrial validation:** Although the anthraquinone process remains the benchmark for large-scale H₂O₂ production, porous-material-based photocatalytic systems are not yet positioned to compete directly at the industrial scale. While the anthraquinone process remains the established benchmark for large-scale, centralised H₂O₂ production. Rather than serving as direct replacements, AFPM-based systems are better suited for decentralised and on-demand H₂O₂ generation at low-to-moderate concentrations (10-100 mM), where transportation, storage, and safety considerations become critical. Operating under mild conditions and enabling integration with flow reactors and in situ utilisation, these systems are well-positioned to complement existing technologies in applications such as water treatment, disinfection, and selective oxidation.

(viii) **Extraction and utilisation of in-situ produced H₂O₂:** The extraction and utilisation of generated H₂O₂ remain critical challenges for its practical deployment. While ex-situ extraction and purification are often necessary for off-site applications, they introduce additional energy and separation costs and can accelerate H₂O₂ decomposition during handling. In contrast, in-situ utilisation



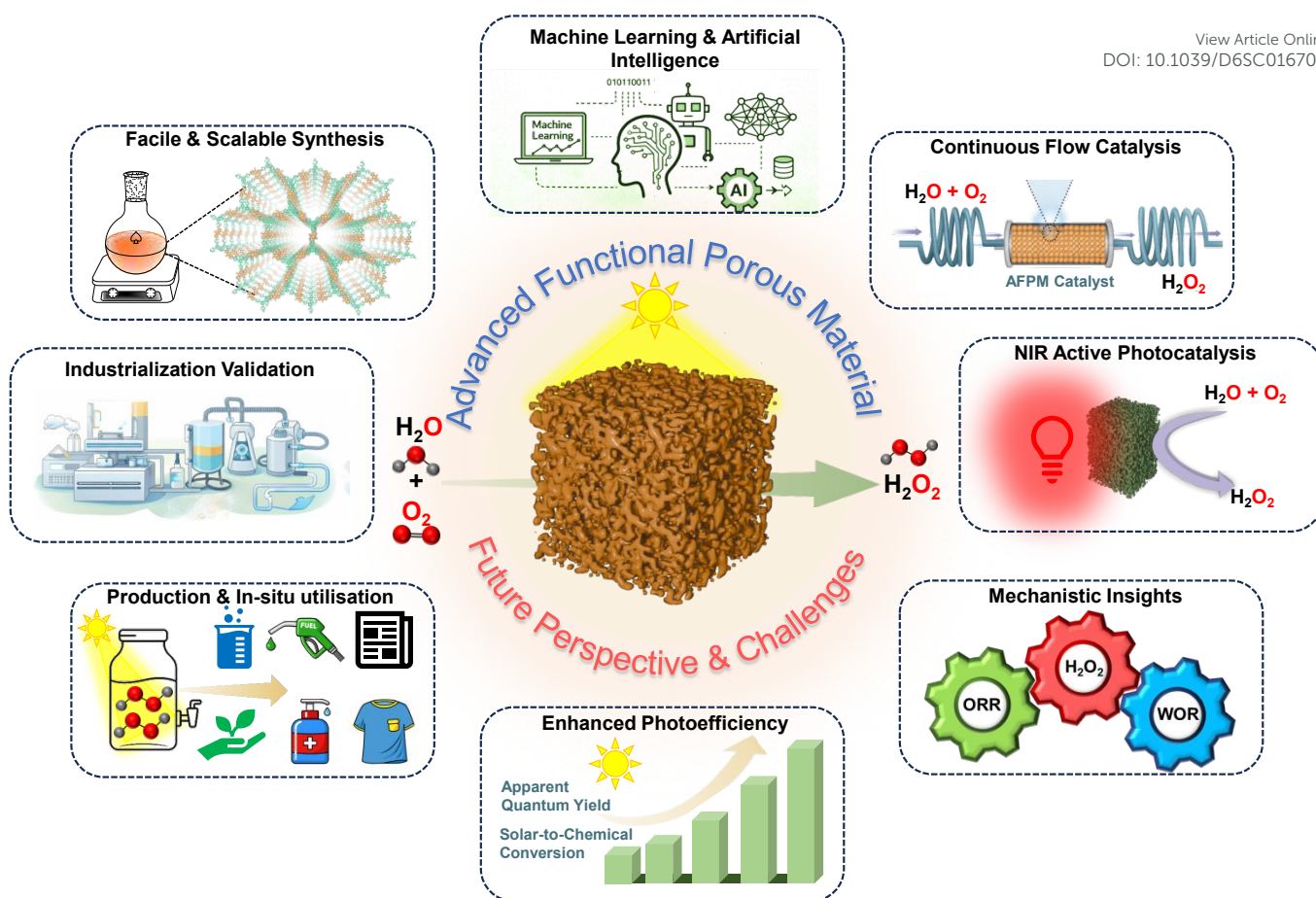


Figure 27: Representative diagram highlighting the future perspectives and challenges in AFPM-based photocatalytic H_2O_2 production.

(ix) strategies, where H_2O_2 is consumed immediately after generation, offer a more efficient and sustainable alternative by minimising accumulation, suppressing decomposition, and reducing safety concerns. oxidation reactions, antimicrobial processes, or pollutant degradation, heavy metal capture and sequestration offer a practical strategy to consume H_2O_2 immediately, suppress degradation pathways, and extend catalyst lifetime. Future advances will depend on reactor designs and porous catalyst architectures that simultaneously facilitate controlled H_2O_2 release, selective mass transport, and seamless integration with end-use reactions, thereby bridging the gap between laboratory-scale synthesis and real-world applications.

(x) **Continuous Flow catalysis:** Flow catalysis presents a compelling strategy for advancing porous materials toward stable and scalable H_2O_2 synthesis. Continuous-flow reactors enable precise control over mass transport, reactant residence time, and photon utilisation, which are critical for regulating the $2e^-$ ORR or WOR pathways while minimising H_2O_2 over-reduction and catalytic decomposition. Importantly, flow operation alleviates local H_2O_2 accumulation and concentration gradients that often accelerate framework degradation in batch systems, thereby enhancing the structural stability and operational durability of porous catalysts. When coupled with robust frameworks and optimised pore environments, flow catalysis offers a practical platform for sustained H_2O_2 production, bridging the gap between laboratory-scale

demonstrations and long-term, industrially relevant operation. By enabling decentralised, on-site generation, flow catalysis eliminates challenges associated with H_2O_2 storage, decomposition, and transport. For real-world implementation, photocatalytic systems should therefore be designed to deliver H_2O_2 on demand at concentrations in the range of 10–100 mM.

(xi) **Suppression of H_2O_2 decomposition:** Direct exposure of the photocatalyst to the generated H_2O_2 frequently promotes its undesired decomposition, thereby restricting achievable yields. To address this challenge, several catalyst-product separation strategies have been explored. Among them, biphasic reaction systems (e.g., water-benzyl alcohol) are widely employed, wherein the hydrophobic character of certain MOFs, combined with density-driven phase separation, enables the preferential transfer of H_2O_2 into the aqueous phase. Although sacrificial agents effectively suppress charge recombination, their use complicates H_2O_2 separation and purification. A more sustainable strategy is to employ sacrificial agents that selectively consume photogenerated holes while simultaneously enabling the synthesis of value-added chemicals.

(xii) **Structure-Activity Relationships and Mechanistic Insights:** Clarifying reaction mechanisms and structure-activity relationships remains a central challenge for AFPM-based photocatalysts in H_2O_2 photosynthesis. Although AFPM offers rich structural diversity through versatile bonding motifs, abundant building blocks, and



tunable functional groups, their structure-performance correlations in H₂O₂ generation are still poorly understood due to complex architectures and reaction environments. Substantial efforts are therefore required to elucidate the roles of electronic structure, pore hydrophilicity/hydrophobicity, and nano-confinement effects in governing photocatalytic activity and selectivity. Beyond rational

material design, the integration of advanced *in situ* characterisation techniques with density functional theory (DFT) calculations is essential to unravel charge-transfer pathways and free-radical mechanisms involved in AFPM-driven H₂O₂ synthesis, which will be critical for accelerating progress in this field.

Conflicts of interest

There are no conflicts to declare

Data availability

No data was used for the research described in the article

Acknowledgements

SMR acknowledges ANRF (formerly SERB) for funding through the National Postdoctoral Fellowship (NPDF) Scheme (Project No. PDF/2023/001234). GKD thanks CSIR for the fellowship. SKG acknowledges DST-SERB (Project No. CRG/2022/001090) and CSIR, India (Project No. 30523670 (01/3124/23/EMR-II) for funding.

References

- J. M. Campos-Martin, G. Blanco-Brieva and J. L. G. Fierro, *Angew. Chem. Int. Ed.* 2006, **45**, 6962–6984
- H. J. H. Fenton, *Journal of Chemical Society, Transaction*, 1894, **65**, 899–909
- M. A. Voinov, J. O. S. Pagán, E. Morrison, T. I. Smirnova and A. I. Smirnov, *J Am Chem Soc*, 2011, **133**, 35–41
- B. W. Richardson, *The Lancet*, 1891, **137**, 707–709
- T. H. Oliver, B. CH. Cantab, D. V Murphy and M. B., *The Lancet*, **195**, 432–433
- J. W. Finney, H. C. Urschel, G. A. Balla, G. J. Race, B. E. Jay, H. P. Pingree, H. L. Dorman and J. T. Mallams, *Ann N Y Acad Sci*, 1967, **141**, 231–241
- M. Armogida, R. Nisticò and N. B. Mercuri, *British Journal of Pharmacology*. 2012, **166**, 1211–1224
- R. Ciriminna, L. Albanese, F. Meneguzzo and M. Pagliaro, *ChemSusChem*, 2016, **9**, 3374–3381
- R. L. Myers, *The 100 Most Important Chemical Compounds: A Reference Guide*, Greenwood Press, 2007.
- A. B. Trench, C. M. Fernandes, J. P. C. Moura, L. E. B. Lucchetti, T. S. Lima, V. S. Antonin, J. M. de Almeida, P. Autreto, I. Robles, A. J. Motheo, M. R. V. Lanza and M. C. Santos, *Chemosphere*, 2024, **352**, 141456
- Y. Tang, W. Wang, J. Ran, C. Peng, Z. Xu and W. Chu, *Energy Environ. Sci.*, 2024, **17**, 6482–6498
- Y. Sun, L. Han and P. Strasser, *Chem. Soc. Rev.*, 2020, **49**, 6605
- Y. Yamada, M. Yoneda and S. Fukuzumi, *Energy Environ Sci*, 2015, **8**, 1698–1701.
- Hydrogen Peroxide Market - By Function (Disinfectant, Bleaching, Oxidant), By Application (Pulp & Paper, Chemical Synthesis, Wastewater Treatment, Mining, Food & Beverages, Personal Care, Healthcare, Textiles), & Forecast, 2024-2032*, 2024
- India Hydrogen Peroxide Market Analysis: Industry Market Size, Plant Capacity, Production, Operating Efficiency, Demand & Supply, End-User Industries, Sales Channel, Regional Demand, Company Share, Foreign Trade, Manufacturing*, 2024
- X. Zhang, X. Zhao, P. Zhu, Z. Adler, Z. Y. Wu, Y. Liu and H. Wang, *Nat Commun*, 2022, **13**, 2880
- S. C. Perry, D. Pangotra, L. Vieira, L. I. Csepei, V. Sieber, L. Wang, C. Ponce de León and F. C. Walsh, *Nature Reviews*, 2019, **3**, 442–458
- X. Liang, Z. Mi, Y. Wang, L. Wang, X. Zhang and T. Liu, *Chem Eng Technol*, 2004, **27**, 176–180
- C. Xia, Y. Xia, P. Zhu, L. Fan and H. Wang, *Science*, 2019, **366**, 226–231
- R. Ernstorfer, M. Harb, C. T. Hebeisen, G. Sciaini, T. Dartigalongue and R. J. D. Miller, *Science*, 2009, **323**, 1033–1037
- J. H. Lunsford, *J Catal*, 2003, **216**, 455–460
- C. E. Baukal Jr, Ed., *Oxygen-enhanced combustion*, CRC Press, Second., 2013
- L. Wang, J. Zhang, Y. Zhang, H. Yu, Y. Qu and J. Yu, *Small*, 2022, **18**, 2104561
- H. Tada, M. Teranishi and S. I. Naya, *Journal of Physical Chemistry C*, 2023, **127**, 5199–5209
- H. Huang, M. Sun, M. Li, L. Tang and S. Zhang, *Green Energy and Resources*, 2023, **1**, 10003125
- W. Wang, Q. Song, Q. Luo, L. Li, X. Huo, S. Chen, J. Li, Y. Li, S. Shi, Y. Yuan, X. Du, K. Zhang and N. Wang, *Nat Commun*, 2023, **14**, 2493
- Z. Li, Z. Yu, C. Guan, K. Xu and Q. Xiang, *Journal of Materiomics*, 2024, **11**, 100982.
- Z. Jiang, C. Li, F. Qi, Z. Wang, Y. Liu, F. Li, H. Wang, Z. Bian, M. Zhu, J. Kumirska and E. M. Siedlecka, *Appl. Mater. Interfaces* 2025, **17**, 42–66
- H. He, S. Liu, Y. Liu, L. Zhou, H. Wen, R. Shen, H. Zhang, X. Guo, J. Jiang and B. Li, *Green Chemistry*, 2023, **25**, 9501–9542
- Y. Yang, C. Wang, Y. Li, K. Liu, H. Ju, J. Wang and R. Tao, *Journal of Materials Science & Technology*, 2024, **200**, 185–214
- Y. Shi, Z. Zhao, D. Yang, J. Tan, X. Xin, Y. Liu and Z. Jiang, *Chem. Soc. Rev.*, 2023, **52**, 6938–6956
- Q. Wang and K. Domen, *Chem. Rev.* 2020, **120**, 919–985
- X. Tao, Y. Zhao, S. Wang, C. Li and R. Li, *Chem Soc Rev*, 2022, **51**, 3561
- R. Marschall, *Eur J Inorg Chem*, 2021, **2021**, 2435–2441
- Y. N. Gong, X. Guan and H. L. Jiang, *Elsevier B.V.*, 2023, preprint, DOI: 10.1016/j.ccr.2022.214889.
- Y. Hao, Y. L. Lu, Z. Jiao and C. Y. Su, *Angew. Chem. Int. Ed.* 2024, **63**, e202317808
- B. Gurung, S. Pradhan, D. Sharma, D. Bhujel, S. Basel, S. Chettri, S. Rasaily, A. Pariyar and S. Tamang, *Catal Sci Technol*, 2022, **12**, 5891–5898
- Ž. Kovačič, B. Likozar and M. Huš, *ACS Catal*, 2020, **10**, 14984–15007
- W. Gao, H. Li, J. Hu, Y. Yang, Y. Xiong, J. Ye, Z. Zou and Y. Zhou, *Chem. Sci.*, 2024, **15**, 14081–14103
- S. Wu and X. Quan, *ACS ES and T Engineering*, 2022, **2**, 1068–1079
- F. Akira and K. Honda, *Nature*, 1972, **238**, 37–38
- G. Zhang, Z. Guan, J. Yang, Q. Li, Y. Zhou and Z. Zou, *Sol. RRL* 2022, **6**, 2200587
- V. Soni, M. Malhotra, P. Singh, A. A. P. Khan, W. A. Bawazir, V. H. Nguyen, T. Ahamad, Q. Van Le, P. Raizada and K. A. Alzahrani, *J Environ Chem Eng*, 2025, **13**, 115151



44. W. Ji, Z. Xu, S. Zhang, Y. Li, Z. Bao, Z. Zhao, L. Xie, X. Zhong, Z. Wei and J. Wang, *Catal Sci Technol*, 2022, **12**, 2865–2871
45. M. Gryszel, R. Rybakiewicz and E. D. Glowacki, *Adv. Sustainable Syst.* 2019, **3**, 1900027
46. Y. Zheng, J. Liu, J. Liang, M. Jaroniec and S. Z. Qiao, *Energy Environ. Sci.*, 2012, **5**, 6717
47. S. Cao, J. Low, J. Yu and M. Jaroniec, *Advanced Materials*, 2015, **27**, 2150–2176
48. J. Fu, J. Yu, C. Jiang and B. Cheng, *Adv. Energy Mater.* 2018, **8**, 1701503
49. J. Zhu, P. Xiao, H. Li and S. A. C. Carabineiro, *American Chemical Society*, 2014, preprint, DOI: 10.1021/am502925j.
50. S. Bordiga, C. Lamberti, G. Ricchiardi, L. Regli, F. Bonino, A. Damin, K. P. Lillerud, M. Bjorgen and A. Zecchina, *Chemical Communications*, 2004, 2300–2301.
51. M. Alvaro, E. Carbonell, B. Ferrer, F. X. Llabrés I Xamena and H. Garcia, *Chemistry - A European Journal*, 2007, **13**, 5106–5112.
52. S. Navalón, A. Dhakshinamoorthy, M. Álvaro, B. Ferrer and H. García, *Chem. Rev.* 2023, **123**, 445–490
53. J. D. Xiao and H. L. Jiang, *Acc Chem Res*, 2019, **52**, 356–366.
54. R. Chen, G. Liu, B. Xia, T. Liu, Y. Xia, S. Liu, A. Talebian-Kiakalaieh and J. Ran, *Chem. Commun.*, 2024, **60**, 10989
55. M. G. Schwab, M. Hamburger, X. Feng, J. Shu, H. W. Spiess, X. Wang, M. Antonietti and K. Müllen, *Chemical Communications*, 2010, **46**, 8932–8934
56. S. Liu, M. Wang, Y. He, Q. Cheng, T. Qian and C. Yan, *Coordination Chemistry Reviews*, 2023, **475**, 214882
57. H. Ran, Q. Xu, Y. Yang, H. Li, J. Fan, G. Liu, L. Zhang, J. Zou, H. Jin and S. Wang, *ACS Catal.* 2024, **14**, 11675–11704
58. M. Debruyne, P. Van Der Voort, V. Van Speybroeck and C. V. Stevens, *Chem. Eur. J.* 2024, **30**, e202400311
59. T. X. Wang, H. P. Liang, D. A. Anito, X. Ding and B. H. Han, *J. Mater. Chem. A*, 2020, **8**, 7003
60. T. Gao, D. Zhao, S. Yuan, M. Zheng, X. Pu, L. Tang, and Z. Lei, *Carbon Energy* 2024, **6**, e596
61. D. Tsukamoto, A. Shiro, Y. Shiraishi, Y. Sugano, S. Ichikawa, S. Tanaka and T. Hirai, *ACS Catal.* 2012, **2**, 599–603.
62. H. L. Tan, C. H. T. Chai, J. Z. X. Heng, Q. V. Thi, X. Wu, Y. H. Ng and E. Ye, *Adv. Sci.* 2025, **12**, 2407801.
63. Y. Shiraishi, S. Kanazawa, Y. Sugano, D. Tsukamoto, H. Sakamoto, S. Ichikawa and T. Hirai, *ACS Catal.* 2014, **4**, 774–780
64. X. Xiao, H. Wang, X. Wang, C. Liu, Y. Han, S. Zhai, H. Du, *Carbon Energy* 2025, **7**, e666
65. D. Tan, R. Zhuang, R. Chen, M. Ban, W. Feng, F. Xu, X. Chen and Q. Wang, *Adv. Funct. Mater.* 2024, **34**, 2311655
66. J. Qiu, D. Dai and J. Yao, *Coord Chem Rev*, 2024, **501**, 215597.
67. W. Wang, X. Wang, M. Gao, Z. Li and W. Zhou, *Coordination Chemistry Reviews*, 2024, **506**, 215694
68. D. Tan and X. Fan, *Polymers*, 2024, **16**, 659
69. K. H. Xie, G. B. Wang, F. Zhao, M. C. Wang, H. Y. Zhang, H. R. Ma, Z. Z. Chen, L. Jiang, Y. Geng and Y. Bin Dong, *Inorg. Chem. Front.*, 2024, **11**, 1322
70. A. P. Cote, A. I. Benin, N. W. Ockwig, M. O’Keeffe, A. J. Matzger and O. M. Yaghi, *Science*, 2005, **310**, 1164–1166.
71. N. L. Campbell, R. Clowes, L. K. Ritchie and A. I. Cooper, *Chemistry of Material*, 2009, **21**, 204–206.
72. X. Zhao, P. Pachfule and A. Thomas, *Chem. Soc. Rev.*, 2021, **50**, 6871–6913
73. Y. N. Gong, X. Guan and H. L. Jiang, *Coordination Chemistry Reviews*, 2023, **475**, 214889
74. L. Stegbauer, K. Schwinghammer and B. V. Lotsch, *Chem. Sci.*, 2014, **5**, 2789–2793.
75. Y. Yusran, H. Li, X. Guan, Q. Fang and S. Qiu, *EnergyChem*, 2020, **2**, 100035
DOI: 10.1039/D6SC01670G
76. Z. Alsudairy, N. Brown, A. Campbell, A. Ambus, B. Brown, K. Smith-Petty and X. Li, *Mater. Chem. Front.*, 2023, **7**, 3298–3331
77. H. Li, A. Dilipkumar, S. Abubakar and D. Zhao, *Chem. Soc. Rev.*, 2023, **52**, 6294–6329.
78. Z. Wang, S. Zhang, Y. Chen, Z. Zhang and S. Ma, *Chem. Soc. Rev.*, 2020, **49**, 708–735
79. X. Zhao, P. Pachfule and A. Thomas, *Chem. Soc. Rev.*, 2021, **50**, 6871–6913.
80. D. G. Wang, T. Qiu, W. Guo, Z. Liang, H. Tabassum, D. Xia and R. Zou, *Energy Environ. Sci.*, 2021, **14**, 688–728.
81. J. Guo, S. Kong, Y. Lian and M. Zhao, DOI: *Chem. Commun.*, 2024, **60**, 918–934.
82. X. Liu, D. Huang, C. Lai, G. Zeng, L. Qin, H. Wang, H. Yi, B. Li, S. Liu, M. Zhang, R. Deng, Y. Fu, L. Li, W. Xue and S. Chen, *Chem. Soc. Rev.*, 2019, **48**, 5266–5302
83. R. Xue, Y. S. Liu, S. L. Huang and G. Y. Yang, *ACS Sens.* 2023, **8**, 2124–2148
84. J. Wang and S. Zhuang, *Coordination Chemistry Reviews*, 2019, **400**, 213046
85. C. I. Yeo, Y. S. Tan, H. T. A. Awan, A. Hanan, W. P. Wong, R. Walvekar, B. H. Goh and M. Khalid, *Coordination Chemistry Reviews*, 2024, **521**, 216167
86. S. Wan, J. Guo, J. Kim, H. Ihee and D. Jiang, *Angew. Chem. Int. Ed.*, 2008, **47**, 8826–8830.
87. I. H. Chowdhury, S. Gupta and V. G. Rao, *ChemCatChem*, 2023, **15**, e202300243
88. H. Wang, H. Wang, Z. Wang, L. Tang, G. Zeng, P. Xu, M. Chen, T. Xiong, C. Zhou, X. Li, D. Huang, Y. Zhu, Z. Wang and J. Tang, *Chem. Soc. Rev.*, 2020, **49**, 4135–4165.
89. C. Krishnaraj, H. Sekhar Jena, L. Bourda, A. Laemont, P. Pachfule, J. Roeser, C. V. Chandran, S. Borgmans, S. M. J. Rogge, K. Leus, C. V. Stevens, J. A. Martens, V. Van Speybroeck, E. Breynaert, A. Thomas and P. Van Der Voort, *J Am Chem Soc*, 2020, **142**, 20107–20116.
90. G. Zhang, M. Zhao, L. Su, H. Yu, C. Wang, D. Sun and Y. Ding, *ACS Appl Mater Interfaces*, 2023, **15**, 20310–20316.
91. H. Liu, S. Zhu, Y. Zhi, H. Yue and X. Liu, *Chem. Sci.*, 2025, **16**, 12768.
92. J. Sun, H. Sekhar Jena, C. Krishnaraj, K. Singh Rawat, S. Abednatanzi, J. Chakraborty, A. Laemont, W. Liu, H. Chen, Y. Y. Liu, K. Leus, H. Vrielinck, V. Van Speybroeck and P. Van Der Voort, *Angew. Chem. Int. Ed.* 2023, **62**, e202216719.
93. R. Liu, Y. Chen, H. Yu, M. Polozij, Y. Guo, T. C. Sum, T. Heine and D. Jiang, *Nat Catal*, 2024, **7**, 195–206.
94. Y. Chen, R. Liu, Y. Guo, G. Wu, T. C. Sum, S. W. Yang and D. Jiang, *Nature Synthesis*, 2024, **3**, 998–1010.
95. D. Li, C. Li, L. Zhang, H. Li, L. Zhu, D. Yang, Q. Fang, S. Qiu and X. Yao, *J. Am. Chem. Soc.*, 2020, **142**, 8104–8108.
96. C. Qin, X. Wu, L. Tang, X. Chen, M. Li, Y. Mou, B. Su, S. Wang, C. Feng, J. Liu, X. Yuan, Y. Zhao and H. Wang, *Nat. Commun.*, 2023, **14**, 5238
97. X. Wang, H. Li, S. Zhou, J. Ning, H. Wei, X. Li, S. Wang, L. Hao and D. Cao, *Adv. Funct. Mater.*, 2025, **35**, 2424035
98. J. Y. Yue, L. P. Song, Y. F. Fan, Z. X. Pan, P. Yang, Y. Ma, Q. Xu and B. Tang, *Angew. Chem. Int. Ed.* 2023, **62**, e202309624
99. C. Shu, X. Yang, L. Liu, X. Hu, R. Sun, X. Yang, A. I. Cooper, B. Tan and X. Wang, *Angew. Chem. Int. Ed.* 2024, **63**, e202403926.
100. J. Yang, Z. Zhao, X. Liu, H. Yang, J. Yang, M. Zhou, S. Li, X. Liu, X. Xu and C. Cheng, *Nat. Commun.*, 2025, **16**, 7654
101. Z. Xue, B. Zhang, Q. Guo, Y. Wang, Q. Li, K. Yang and S. Qiao, *Adv. Mater.* 2025, **37**, e10201.



102. Z. Zhang, Y. Hou, S. Zhu, L. Yang, Y. Wang, H. Yue, H. Xia, G. Wu, S. Wang Yang and X. Liu, *Angew. Chem. Int. Ed.* 2025, **64**, e202505286
103. J. Chen, S. Yan, F. Wang, F. Lin, J. Lin, R. A. Borse and Y. Wang, *Angew. Chem. Int. Ed.* 2025, **64**, e202500924
104. M. Deng, L. Wang, Z. Wen, J. Chakraborty, J. Sun, G. Wang and P. Van Der Voort, *Green Chemistry*, 2024, **26**, 3239–3248.
105. H. Ma, Y. Zhang, Y. Wu, Q. Gu, Z. Li and Q. Zhang, *Chem. Sci.*, 2025, **16**, 16668–16677
106. H. Wang, C. Yang, F. Chen, G. Zheng and Q. Han, *Angew. Chem. Int. Ed.* 2022, **61**, e20220232
107. Y. Yang, J. Kang, Y. Li, J. Liang, J. Liang, L. Jiang, D. Chen, J. He, Y. Chen and J. Wang, *New J. Chem.*, 2022, **46**, 21605–21614.
108. J. N. Chang, Q. Li, J. W. Shi, M. Zhang, L. Zhang, S. Li, Y. Chen, S. L. Li and Y. Q. Lan, *Angew. Chem. Int. Ed.* 2023, **62**, e202218868
109. J.-C. Liu, C. Tuo, W.-Y. Xiao, M.-Y. Qi, Y. Yusran, Z.-T. Wang, H. Li, C.-S. Guo, J.-L. Song, S.-L. Qiu, Y.-J. Xu and Q. Fang, *Angew. Chem. Int. Ed.* 2025, **64**, e202416240
110. R. Wang, Z. Wang, L. Li, L. Zhang, Ji. Zhang, H. Jin, Q. Xu, Y. Wei, Y. Yang, and S. Wang, *Journal of Catalysis*, 2025, **450**, 116289.
111. Y. Xie, F. Mao, Q. Rong, X. Liu, M. Hao, Z. Chen, H. Yang, G. I. N. Waterhouse, S. Ma and X. Wang, *Adv. Funct Mater.*, 2024, **34**, 2411077.
112. H. Xu, Y. Wang, Y. Xu, Q. Wang, M. Zhuang, Q. Liao and K. Xi, *Angew. Chem. Int. Ed.* 2024, **63**, e202408802
113. X. Di, X. Lv, H. Wang, F. Chen, S. Wang, G. Zheng, B. Wang and Q. Han, *Chem. Eng. J.*, 2023, **455**, 140124
114. V. S. Vyas, F. Haase, L. Stegbauer, G. Savasci, F. Podjaski, C. Ochsenfeld and B. V. Lotsch, *Nat Commun*, 2015, **6**, 8508
115. D. Chen, W. Chen, Y. Wu, L. Wang, X. Wu, H. Xu and L. Chen, *Angew. Chem. Int. Ed.* 2023, **62**, e202217479.
116. Z. Zhang, Q. Zhang, Y. Hou, J. Li, S. Zhu, H. Xia, H. Yue and X. Liu, *Angew. Chem. Int. Ed.* 2024, **63**, e202411546
117. X. Yang, Z. X. Pan, J. Y. Yue, X. Li, G. Liu, Q. Xu and G. Zeng, *Small* 2024, **20**, 2405907
118. W. Wu, Z. Li, S. Liu, D. Zhang, B. Cai, Y. Liang, M. Wu, Y. Liao and X. Zhao, *Angew. Chem. Int. Ed.* 2024, **63**, e202404563
119. Z. Li, B. Cai, Y. Zou, D. Zhang, Y. Liang, Y. Zhou, Y. Ma, X. Wang, B. Shi, W. K. Chen, Y. Liu and X. Zhao, *Adv. Energy Mater.*, 2025, **15**, 2500341.
120. Y. Hou, P. Zhou, F. Liu, Y. Lu, H. Tan, Z. Li, M. Tong and J. Ni, *Angew. Chem. Int. Ed.* 2024, **63**, e202318562
121. D. Cao, J. Du, J. Li, Q. Sun, J. Guan and J. Liu, *ACS Catal*, 2025, **15**, 3584–3594.
122. Y. Ju, H. Lin, G. Tan, P. Su, Z. Wang, C. Hu, R. Hou, T. Hao, F. Chen and Y. Tang, *Nat. Commun.*, 2025, **16**, 5658
123. H. Yu, F. Zhang, Q. Chen, P. K. Zhou, W. Xing, S. Wang, G. Zhang, Y. Jiang and X. Chen, *Angew. Chem. Int. Ed.* 2024, **63**, e202402297
124. L. Guo, L. Gong, Y. Yang, Z. Huang, X. Liu and F. Luo, *Angew. Chem. Int. Ed.* 2025, **64**, e202414658.
125. Y. Yao, C. Zhu, R. Liu, Q. Fang, S. Song, B. Chen and Y. Shen, *Small*, 2024, **20**, 2404885.
126. S. Kandambeth, A. Mallick, B. Lukose, M. V. Mane, T. Heine and R. Banerjee, *J Am Chem Soc*, 2012, **134**, 19524–19527
127. H. Wang, C. Qian, J. Liu, Y. Zeng, D. Wang, W. Zhou, L. Gu, H. Wu, G. Liu and Y. Zhao, *J Am Chem Soc*, 2020, **142**, 4862–4871
128. Y. Kong, X. He, H. Wu, Y. Yang, L. Cao, R. Li, B. Shi, G. He, Y. Liu, Q. Peng, C. Fan, Z. Zhang and Z. Jiang, *Angew. Chem. Int. Ed.*, 2021, **60**, 17638–17646
129. H. Hu, Y. Tao, D. Wang, C. Li, Q. Jiang, Y. Shi, J. Wang, J. Qin, S. Zhou and Y. Kong, *J Colloid Interface Sci*, 2023, **629**, 750–762.
130. X. Zhang, J. Zhang, J. Miao, X. Wen, C. Chen, B. Zhou and M. Long, *Chemical Engineering Journal* 2023, **466**, 143085
131. X. Zhang, S. Cheng, C. Chen, X. Wen, J. Miao, B. Zhou, M. Long and L. Zhang, *Nat Commun*, 2024, **15**, 2649 DOI: 10.1039/D6SC01670G
132. H. Li, Y. Li, X. Lv, C. Liu, N. Zhang, J. Zang, P. Yue, Y. Gao, C. Liu and Y. Li, *Adv. Mater.* 2025, **37**, 2415126.
133. K.-H. Xie, G.-B. Wang, F. Huang, F. Zhao, J.-L. Kan, Z.-Z. Chen, L. Cai, S.-L. Han, Y. Geng and Y.-B. Dong, *Nat Commun*, 2025, **16**, 3493
134. T. Yang, D. Zhang, A. Kong, Y. Zou, L. Yuan, C. Liu, S. Luo, G. Wei and C. Yu, *Angew. Chem. Int. Ed.* 2024, **63**, e202404077
135. L. Fang, H. Xu, S. Qiu, T. Ye, T. Wang, J. Shang, C. Gu, S. Kitagawa and L. Li, *Angew. Chem. Int. Ed.* 2025, **64**, e202423220
136. H.-H. Sun, Z.-B. Zhou, Y. Fu, Q.-Y. Qi, Z.-X. Wang, S. Xu and X. Zhao, *Angew. Chem. Int. Ed.* 2024, **63**, e202409250
137. Y. Mou, X. Wu, C. Qin, J. Chen, Y. Zhao, L. Jiang, C. Zhang, X. Yuan, E. Huixiang Ang and H. Wang, *Angew. Chem. Int. Ed.* 2023, **62**, e20230948
138. A. Chakraborty, A. Alam, U. Pal, A. Sinha, S. Das, T. Saha-Dasgupta and P. Pachfule, *Nat Commun*, 2025, **16**, 503
139. T. Xu, Z. Wang, W. Zhang, S. An, L. Wei, S. Guo, Y. Huang, S. Jiang, M. Zhu, Y. B. Zhang and W. H. Zhu, *J Am Chem Soc*, 2024, **146**, 20107–20115.
140. J. Y. Yue, L. P. Song, Y. F. Fan, Z. X. Pan, P. Yang, Y. Ma, Q. Xu and B. Tang, *Angew. Chem. Int. Ed.* 2023, **62**, e202309624
141. W. Wang, R. Zhang, H. Chu, Z. Zhan, Q. Huang, Z. Li, X. Wang, F. Bai and W. Zhou, *Small*, 2025, **21**, 2406527.
142. P. Li, H. Zhao, R. Ji, W. Chi, X. Sun, Y. Dong and Y. Zhu, *Catal Sci Technol*, 2024, **14**, 2470–2478.
143. K. Prakash, R. Deka and S. M. Mobin, *Inorg. Chem. Front.*, 2024, **11**, 6711–6752
144. C. Pan, Y. Han and J. Lu, *Appl. Sci.* 2020, **10**, 6374.
145. R. Freund, S. Canossa, S. M. Cohen, W. Yan, H. Deng, V. Guillermin, M. Eddaoudi, D. G. Madden, D. Fairen-Jimenez, H. Lyu, L. K. Macreadie, Z. Ji, Y. Zhang, B. Wang, F. Haase, C. Wöll, O. Zaremba, J. Andreo, S. Wuttke and C. S. Diercks, *Angew. Chem. Int. Ed.* 2021, **60**, 23946 – 23974
146. J. Y. Yue, J. X. Luo, Z. X. Pan, R. Z. Zhang, P. Yang, Q. Xu and B. Tang, *Angew. Chem. Int. Ed.* 2024, **63**, e202405763
147. J. Cheng, Y. Wu, W. Zhang, L. Wang, X. Wu and H. Xu, *Adv. Mater.* 2025, **37**, 2410247.
148. H. M. El-Kaderi, J. R. Hunt, J. L. Mendoza-Cortés, A. P. Côté, R. E. Taylor, M. O’Keeffe and Yaghi Omar M., *Science*, 2007, **316**, 268–272.
149. R.-M. Zhu, Y. Liu, W.-K. Han, J.-D. Feng, J. Zhang, H. Pang, J. Zhang and Z.-G. Gu, *Angew. Chem. Int. Ed.* 2025, **64**, e202412890.
150. J. P. Liao, M. Zhang, P. Huang, L. Z. Dong, T. T. Ma, G. Z. Huang, Y. F. Liu, M. Lu, S. L. Li and Y. Q. Lan, *ACS Catal*, 2024, **14**, 3778–3787.
151. W. Lan, B. Wei, Y. Jin, S. Xu, H. Zhou, Y. Wu, Q. Liu, P. Chen, J. Wang, X. Zhao, H. Meng, L. Liu, D. Wang, H. Huang, Y. Wei, Q. Zhu and Y. Yu, *Small*, 2025, **21**, 2501327.
152. X. Guan, F. Chen, Q. Fang and S. Qiu, *Chem. Soc. Rev.*, 2020, **49**, 1357–1384.
153. K. Yu, P. He, D. Zhang, H. Wu, K. Shu, H. Long, Y. Sun, X. Pei, B. Jiang, K. Cao, Y. Li and L. Ma, *Angew. Chem. Int. Ed.* 2025, **64**, e202511501
154. Z. Gong, Y. Gao, J. Li, Z. Cai, N. Liu and J. Jiang, *Angew. Chem. Int. Ed.* 2025, **64**, e202423205
155. X. Wang, Y. Jin, N. Li, H. Zhang, X. Liu, X. Yang, H. Pan, T. Wang, K. Wang, D. Qi and J. Jiang, *Angew. Chem. Int. Ed.* 2024, **63**, e202401014.
156. Z. S. Zhu, S. Zhong, C. Cheng, H. Zhou, H. Sun, X. Duan and S. Wang, *Chem. Rev.* 2024, **124**, 11348–11434
157. Y. Liu, L. Li, Z. Sang, H. Tan, N. Ye, C. Sun, Z. Sun, M. Luo and S. Guo, *Nat. Synth* 2025, **4**, 134–141.



158. Z. Ding, J. Yang, Z. Wu, M. Adeli, X. Luo, X. Wang, X. Xie, X. Xu, C. Cheng and C. Zhao, *Chem. Mater.* 2025, **37**, 1972–1982.
159. Y. Zhang, Y. Wu, H. Ma, Y. Gao, X. Fan, Y. Zhao, F. Kang, Z. Li, Y. Liu and Q. Zhang, *Small* 2025, **21**, 2500674.
160. Q. Zhou, Y. Guo and Y. Zhu, *Nat Catal*, 2023, **6**, 574–584.
161. M. Guo, C. He, Z. Wu, Y. Tian, J. Yang, Y. Wang, H. Wu, J. Yang, M. Xu, W. Xue, C. Cheng, S. Li and C. Zhao, *Adv. Sci.* 2025, **12**, e05794
162. X. Ding, T. Wang, B. Yu, Q. Zhi, H. Wang, H. Liu, P. A. Stuzhin and J. Jiang, *Adv Funct Mater*, 2025, 2422291.
163. X. F. Lu, Y. Fang, D. Luan and X. W. D. Lou, *Nano Lett*, 2021, **21**, 1555–1565.
164. W. Xia, A. Mahmood, R. Zou and Q. Xu, *Energy Environ. Sci.*, 2015, **8**, 1837–1866.
165. J. Lee, O. K. Farha, J. Roberts, K. A. Scheidt, S. T. Nguyen and J. T. Hupp, *Chem Soc Rev*, 2009, **38**, 1450–1459.
166. W. Cheng, X. F. Lu, D. Luan and X. W. Lou, *Angew. Chem. Int. Ed.*, 2020, **59**, 18234–18239.
167. S. Zhao, Y. Wang, J. Dong, C. T. He, H. Yin, P. An, K. Zhao, X. Zhang, C. Gao, L. Zhang, J. Lv, J. Wang, J. Zhang, A. M. Khatkhat, N. A. Khan, Z. Wei, J. Zhang, S. Liu, H. Zhao and Z. Tang, *Nat Energy*, 2016, **1**, 16184
168. J. Q. Shen, P. Q. Liao, D. D. Zhou, C. T. He, J. X. Wu, W. X. Zhang, J. P. Zhang and X. M. Chen, *J Am Chem Soc*, 2017, **139**, 1778–1781.
169. N. Diyali, S. Rasaily and B. Biswas, *Coordination Chemistry Reviews* 2022, **469**, 214667.
170. S. Rasaily, D. Sharma, S. Pradhan, N. Diyali, S. Chettri, B. Gurung, S. Tamang and A. Pariyar, *Inorg Chem*, 2022, **61**, 13685–13699.
171. D. Sharma, S. Rasaily, S. Chettri, D. Sureka, S. Tamang and A. Pariyar, *Inorg Chem*, 2023, **62**, 4540–4549
172. (a) L. J. Murray, M. Dinca and J. R. Long, *Chem. Soc. Rev.*, 2009, **38**, 1294–1314 (b) H. Li, L. Li, R. B. Lin, W. Zhou, Z. Zhang, S. Xiang and B. Chen, *EnergyChem*, 2019, **1**, 100006
173. R. B. Lin, S. Xiang, W. Zhou and B. Chen, *Chem*, 2020, **6**, 337–363.
174. S. Dutta, S. Mukherjee, O. T. Qazvini, A. K. Gupta, S. Sharma, D. Mahato, R. Babarao and S. K. Ghosh, *Angew. Chem. Int. Ed.* 2022, **61**, e202114132.
175. S. Mollick, S. Saurabh, Y. D. More, S. Fajal, M. M. Shirolkar, W. Mandal and S. K. Ghosh, *Energy Environ Sci*, 2022, **15**, 3462–3469.
176. S. Fajal, D. Ghosh, W. Mandal and S. K. Ghosh, *Chem. Commun.*, 2024, **60**, 1884–1887.
177. H. Sohrabi, S. Ghasemzadeh, Z. Ghoreishi, M. R. Majidi, Y. Yoon, N. Dizge and A. Khataee, *Mater Chem Phys*, 2023, **299**, 127512.
178. P. Samanta, S. Let, W. Mandal, S. Dutta and S. K. Ghosh, *Inorg. Chem. Front.*, 2020, **7**, 1801–1821.
179. A. Karmakar, N. Kumar, P. Samanta, A. V. Desai and S. K. Ghosh, *Chemistry - A European Journal*, 2016, **22**, 864–868.
180. H. S. Wang, Y. H. Wang and Y. Ding, *Nanoscale Adv.*, 2020, **2**, 3788–3797.
181. J. Y. Choi, B. Check, X. Fang, S. Blum, H. T. B. Pham, K. Tayman and J. Park, *J. Am. Chem. Soc.* 2024, **146**, 11319–11327.
182. X. Wang, J. Li, X. Wei, J. Song, J. Xie, Z. Li, M. Yuan, L. Jiang, Y. Wang, C. Liang and W. Liu, *ACS Omega*, 2024, **9**, 33671–33678.
183. Y. Zhang, Z. Luo, T. Zhou, H. Huang and H. Tang, *Chemical Communications*, 2024, **60**, 1920–1923.
184. Y. Zheng, H. Zhou, B. Zhou, J. Mao and Y. Zhao, *Catal Sci Technol*, 2022, **12**, 969–975.
185. X. Y. Ji, Y. Y. Wang, Y. Li, K. Sun, M. Yu and J. Tao, *Nano Res*, 2022, **15**, 6045–6053.
186. Y. Zhang, C. Pan, G. Bian, J. Xu, Y. Dong, Y. Zhang, Y. Lou, W. Liu and Y. Zhu, *Nat Energy*, 2023, **8**, 361–371.
187. M. Shao, R. Bao, H. Guo, C. Yao, S. Wang, Y. Song and X. Guo, *Inorg. Chem.*, 2025, **64**, 18567–18576.
188. A. Pal, S. Suresh, A. Khan, L. Huai Kuo, L. Tang Chi, A. Ganguly, C.-Y. Kao, M. Kumar Sharma, T.-S. Andrew Wang, D. Y. Kang and Z. H. Lin, *Sci. Adv.* 2025, **11**, 4711.
189. Y-X Li, Y. Hu, H-S Bae, J. Du, S. Zhao, D. Pan, W. Choi, *ACS Nano* 2024, **42**, 29233–29247
190. S. Fajal, S. Dutta and S. K. Ghosh, *Mater. Horiz.*, 2023, **10**, 4083–4138
191. A. Trewin and A. I. Cooper, *Angew. Chem. Int. Ed.* 2023, 2010, **49**, 1533–1535.
192. B. Mishra, A. Alam, B. Kumbhakar, D. Díaz Díaz and P. Pachfule, *Cryst. Growth Des.* 2023, **23**, 4701–4719.
193. C. Liu, M. Chen, H. Li, Q. Shi, Y. Feng and B. Zhang, *Cryst Growth Des*, 2022, **22**, 4745–4756.
194. L. Liao, M. Li, Y. Yin, J. Chen, Q. Zhong, R. Du, S. Liu, Y. He, W. Fu and F. Zeng, *ACS Omega* 2023, **8**, 5, 4527–4542.
195. M. Liu, L. Guo, S. Jin and B. Tan, *J. Mater. Chem. A*, 2019, **7**, 5153–5172.
196. S. R. Zhu, Q. Qi, Y. Fang, W. N. Zhao, M. K. Wu and L. Han, *Cryst Growth Des*, 2018, **18**, 883–891.
197. F. Niu, L. Tao, Y. Deng, H. Gao, J. Liu and W. Song, *New Journal of Chemistry*, 2014, **38**, 5695–5699.
198. C. Yang, W. Huang, L. C. da Silva, K. A. I. Zhang and X. Wang, *Chemistry - A European Journal*, 2018, **24**, 17454–17458.
199. S. Kumar, B. Bayarkhuu, H. Ahn, H. Cho and J. Byun, *Nano Trends*, 2023, **4**, 100023.
200. H. Zhang, W. Wei, K. Chi, Y. Zheng, X. Y. Kong, L. Ye, Y. Zhao and K. A. I. Zhang, *ACS Catal*, 2024, 17654–17663.
201. L. Zhang, C. Wang, Q. Jiang, P. Lyu and Y. Xu, *J Am Chem Soc*, 2024, **146**, 29943–29954.
202. L. Chen, L. Wang, Y. Wan, Y. Zhang, Z. Qi, X. Wu and H. Xu, *Adv. Mater.* 2020, **32**, 1904433.
203. Y. Yang, Q. Guo, Q. Li, L. Guo, H. Chu, L. Liao, X. Wang, Z. Li and W. Zhou, *Adv Funct Mater*, 2024, **34**, 2400612.
204. X. Nie, Y. Zhao, W. Gao, W. Liu, X. Cheng, Y. Gao, N. Shang, S. Gao and C. Wang, *Chem. Eur. J.* 2023, **29**, e202203607
205. X. Xu, D. Jiang, K. Xie, Y. Sui, W. Chen, Y. Li, H. Zhong, and H-R Wen, *ACS Appl. Polym. Mater.* 2025, **7**, 6920–693
206. X. Xu, L. Chai, Y. Li, W. Chen, X. Li, W. Huang, G. Zhou, H. Zhong, and Y. Sui, *Polymer*, 2025, **340**, 129236
207. Y. Wang, W. Chi, R. Zhang, Y. Guo, X. Sun, H. Zhao, J. Zhang, Y. Dong and Y. Zhu, *New Journal of Chemistry*, 2024, **48**, 9043–9051
208. G. Lv, X. Yu, J. Wang, J. Qiu, D. Yang and Y. Zhu, *Adv. Funct. Mater.*, 2026, **36**, e17393
209. R. Sun, X. Yang, X. Hu, Y. Guo, Y. Zhang, C. Shu, X. Yang, H. Gao, X. Wang, I. Hussain and B. Tan, *Angew. Chem. Int. Ed.* 2025, **64**, e202416350.
210. Y. Guo, X. Yang, R. Sun, X. Hu, C. Shu, X. Yang, H. Gao, X. Wang and B. Tan, *Small*, 2024, **20**, 2403743.
211. X. Xu, Y. Sui, W. Chen, S. Xiong, Y. Li, X. Li, W. Huang, H. Zhao, G. Zhou, H. Chen and H. Zhong, *ACS Sustain Chem Eng*, 2024, **12**, 11409–11418
212. S. Lee, H. Jeong, D. Nam, M. S. Lah and W. Choe, *Chem. Soc. Rev.*, 2021, **50**, 528–555
213. A. J. Gosselin, C. A. Rowland and E. D. Bloch, *Chem. Rev.* 2020, **120**, 8987–9014
214. E. S. M. El-Sayed, Y. Di Yuan, D. Zhao and D. Yuan, *Acc Chem Res*, 2022, **55**, 1546–1560
215. Y. P. Wang, Y. Zhang, X. H. Duan, J. J. Mao, M. Pan, J. Shen and C. Y. Su, *Coordination Chemistry Reviews* 2024, **501**, 215570
216. D. Majumder, S. Fajal, M. M. Shirolkar, A. Torris, Y. Banyla, K. Biswas, S. Rasaily and S. K. Ghosh, *Angew. Chem. Int. Ed.* 2025, **64**, e202419830



217. Y. Liu, L. Huang, L. Qin and T. Zhou, *ChemCatChem*, 2025, **17**, e202401487
218. Y. L. Lu, Y. P. Wang, K. Wu, M. Pan and C. Y. Su, *Acc. Chem. Res.* 2024, **57**, 3277–3291.
219. J. N. Lu, J. J. Liu, L. Z. Dong, J. M. Lin, F. Yu, J. Liu and Y. Q. Lan, *Angew. Chem. Int. Ed.* 2023, **62**, e202308505
220. L. Xiao, H. Zhao, F. Fu, Y. Han, J. Wang, Q. Dong, X. Hu, N. Wang, Y. Wei, P. Wang, D. Liu and Y. Li, *Angew. Chem. Int. Ed.* 2025, **64**, e202516678
221. R. B. Lin, Y. He, P. Li, H. Wang, W. Zhou and B. Chen, *Chem. Soc. Rev.*, 2019, **48**, 1362–1389
222. B. Wang, R. B. Lin, Z. Zhang, S. Xiang and B. Chen, *J. Am. Chem. Soc.* 2020, **142**, 14399–14416
223. W. Yang, A. Greenaway, X. Lin, R. Matsuda, A. J. Blake, C. Wilson, W. Lewis, P. Hubberstey, S. Kitagawa, N. R. Champness and M. Schröder, *J Am Chem Soc*, 2010, **132**, 14457–14469
224. Y. He, S. Xiang and B. Chen, *J Am Chem Soc*, 2011, **133**, 14570–14573
225. Y. Li, S. Tang, A. Yusov, J. Rose, A. N. Borrfors, C. T. Hu and M. D. Ward, *Nat Commun*, 2019, **10**, 4477
226. C. J. Lu, W. J. Shi, Y. N. Gong, J. H. Zhang, Y. C. Wang, J. H. Mei, Z. M. Ge, T. B. Lu and D. C. Zhong, *Angew. Chem. Int. Ed.* 2024, **63**, e202405451
227. Q. Yin, E. V. Alexandrov, D. H. Si, Q. Q. Huang, Z. Bin Fang, Y. Zhang, A. A. Zhang, W. K. Qin, Y. L. Li, T. F. Liu and D. M. Proserpio, *Angew. Chem. Int. Ed.* 2022, **61**, e202115854
228. J. H. Zhang, Z. M. Ge, J. Wang, D. C. Zhong and T. B. Lu, *Nat Comm*, 2025, **16**, 2448
229. J. L. Segura, S. Royuela and M. Mar Ramos, *Chem. Soc. Rev.*, 2019, **48**, 3903–3945
230. Q. Shang, Y. Liu, J. Ai, Y. Yan, X. Yang, D. Wang and G. Liao, *J Mater Chem A Mater*, 2023, **11**, 21109–21122
231. Y. Cong, X. Li, S. Zhang, Q. Zheng, Y. Zhang and S. W. Lv, *ACS Appl Mater Interfaces*, 2023, **15**, 43799–43809
232. L. Ma, J. Xu, S. Zhao, L. Li and Y. Liu, *Chemistry - A European Journal*, 2021, **27**, 15795–15805
233. Y. He, J. Zhao, Y. T. Sham, S. Gao, M. Pan, Q. Chen, G. Huang, P. K. Wong and J. Bi, *ACS Sustain Chem Eng*, 2023, **11**, 17552–17563
234. G. Xia, J. Qiu, L. Zhang, D. Dai and J. Yao, *Colloids Surf A Physicochem Eng Asp*, 2023, **664**, 131124
235. Y. Yang, Y. Li, X. Ma, L. Xie, D. Lv, L. Jiang, J. He, D. Chen and J. Wang, *Catal Sci Technol*, 2023, **13**, 5599–5609
236. Q. Zuo, B. Chu, X. Ye, F. Li, L. Li and Q. Xu, *J. Am. Chem. Soc.*, 2025, **147**, 34681–34689.
237. J. Zhu, X. F. Lu, D. Luan and X. W. Lou, *Angew. Chem. Int. Ed.* 2024, **63**, e202408846
238. S. Rasaily, K. Baruah, D. Sharma, P. Lepcha, S. Biswas, A. N. Biswas, S. Tamang and A. Pariyar, *Inorg Chem*, 2023, **62**, 3026–3035
239. S. Rasaily, S. Chettri, D. Sharma, K. Baruah, R. Dewan, S. Tamang and A. Pariyar, *Inorg Chem*, 2024, **63**, 17846–17855
240. Y. T. Zheng, S. Li, N. Y. Huang, X. Li and Q. Xu, *Coordination Chemistry Reviews*, 2024, **510**, 215858
241. M. I. Gonzalez, A. B. Turkiewicz, L. E. Darago, J. Oktawiec, K. Bustillo, F. Grandjean, G. J. Long and J. R. Long, *Nature*, 2020, **577**, 64–68
242. Z. R. Tao, J. X. Wu, Y. J. Zhao, M. Xu, W. Q. Tang, Q. H. Zhang, L. Gu, D. H. Liu and Z. Y. Gu, *Nat Commun*, 2019, **10**, 2911
243. J. Qiu, L. Zhang, G. Xia, D. Dai, Y. Tang and J. Yao, *Catal Sci Technol*, 2023, **13**, 2101–2107
244. Y. Kondo, K. Hino, Y. Kuwahara, K. Mori and H. Yamashita, *J Mater Chem A Mater*, 2023, **11**, 9530–9537
245. Y. Kondo, K. Hino, Y. Kuwahara, K. Mori, H. Kobayashi and H. Yamashita, *ChemComm*, 2022, **58**, 12345–12348
246. Y. C. Hao, L. W. Chen, J. Li, Y. Guo, X. Su, M. Shu, Q. Zhang, W. Y. Gao, S. Li, Z. L. Yu, L. Gu, X. Feng, A. X. Yin, R. Si, Y. W. Zhang, B. Wang and C. H. Yan, *Nat Commun*, 2021, **12**, 2682
247. C. D. Gheewala, B. E. Collins and T. H. Lambert, *Science*, 2016, **351**, 961–965
248. Y. Lin, J. Zou, X. Wu, S. Tong, Q. Niu, S. He, S. Luo and C. Yang, *Nano Lett*, 2024, **24**, 6302–6311
249. Z. Li, X. Shi, H. Cheng, Y. Song, Y. Jiao, S. Shi, J. Gao and J. Hou, *Adv Energy Mater*, 2024, **14**, 2302797



View Article Online
DOI: 10.1039/D6SC01670G

Data availability

No primary research results, software or code have been included and no new data were generated or analysed as part of this review.

